THE INVESTIGATION OF ADVANCED CARBON-BASED NANOCOMPOSITES FOR RENEWABLE ENERGY APPLICATION

XU DAN

PhD

The Hong Kong Polytechnic University

2024

Initial Submission for Examination Purpose

The Hong Kong Polytechnic University

Department of Building Environment and Energy Engineering

The investigation of advanced carbon-based nanocomposites for renewable energy application

XU DAN

A thesis submitted in partial fulfilment of the requirements for the degree of Doctor of Philosophy

July 2024

CERTIFICATE OF ORIGINALITY

I hereby declare that this thesis is my own work and that, to the best of my knowledge and belief, it reproduces no material previously published or written, nor material that has been accepted for the award of any other degree or diploma, except where due acknowledgement has been made in the text.

____________________ (Signed)

____XU DAN______ (Name of student)

Abstract

Nanotechnology has been used in various emerging renewable energy applications, and the focus is to enhance the efficiency of existing technologies. While the challenges of nanomaterials in practical applications include the cost, the stability and sustainability, and environmental impact. The strategies for developing new carbon nanomaterials typically involve structural design and functional enhancement. This thesis explores new strategies for advanced carbon nanocomposites, enhancing the performance in hydrogen generation, photothermal utilization for water production and nano-mechanical harvesting.

First, to develop efficient electrode for hydrogen production through water electrolysis, 3-D composites has been synthesized by using laser-induced forward transfer (LIFT) technology. The study introduced a facile method to fabricate a composite consisting of ultrasmall Cu_xO nanoparticles immobilized on porous graphene dispersed on Ni foam. This composite demonstrated remarkable performance in the hydrogen evolution reaction (HER) when tested in a 1M KOH solution. It exhibited a low overpotential of 149.6 mV to achieve an area current density of 10 mA cm^{-2}, with a Tafel slope of 157 mV dec^{-1}. This study highlights the promising potential of the proposed facile preparation method, offering a highly efficient and cost-effective catalyst for scalable hydrogen production.

Second, utilizing LIFT technology combined with solar driven evaporation technology, a composite of Cu nanoparticles (Cu NPs) and Graphene has been synthesized to achieve solar driven freshwater harvesting. A portable interfacial evaporator was fabricated using a one-step deposition method, employing a 3D-structured plasmonic enhanced photothermal nanocomposite composed of Cu nanoparticles/laser-induced graphene (Cu NPs/LIG). This innovative evaporator demonstrates excellent solar absorption with broadband spectrum coverage. Furthermore, this solar-driven evaporator exhibits a high evaporation rate of 2.29 kg/m^2·h when operating with pure water. Long-term experiments showed a high evaporation efficiency of 1.82 kg/m^2·h when operating with brine containing a high salinity of 20 wt.%.

Third, interfaces have been built through the incorporation of polarizable molecules into single-walled carbon nanotubes to harness energy through the flexoelectric effect. Semiconductor single-walled carbon nanotubes (SWCNTs) with diameters ranging from 1.0 nm to 1.5 nm were carefully chosen for the study. Within these SWCNTs, two distinct types of polar molecules were embedded. The flexoelectric effect in these modified carbon nanotubes, initially non-polarized, was examined using the atomic force microscopy (AFM) probe technique. By combining AFM scans in orca, PFM, SCM, and AM-FM modes, this engineered interface enhancement strategy was validated and visualized from both electrical and nanomechanical imaging perspectives.

In summary, this thesis has newly developed strategies for obtaining advanced carbon nanocomposites. The laser fabricated novel composites have been successfully applied for hydrogen production and solar-driven vapor generation. Meanwhile, the functionalization strategy of surfaced modified SWCNTs by two polar molecules has been first time studied to construct engineered interface, and nano energy harvesting has been successfully achieved via the flexoelectric effect. The strategies employed in this thesis for the facile fabrication of 3D graphene-based nanocomposites and interface engineering have laid the foundation for developing novel functionalized carbon nanomaterials. These strategies have also expanded the utilization of new carbon nanomaterials in renewable energy applications.

Publications arising from the thesis

[1] **Xu Dan.,** Zhong, H., Li, M. G., To, S. S., Lu, L. (2023). Efficient plasmonic enhanced solar evaporation achieved by laser-assisted Cu/Graphene nanocomposite. **Carbon**, 204, 231-237.

[2] **Xu Dan.,** Chan, K. C., Guo, H. J, Zhong, H., Lu, L. (2021). One-step fabrication of a laser-induced forward transfer graphene/Cu_xO nanocomposite-based electrocatalyst to promote hydrogen evolution reaction. **Journal of Materials Chemistry A**, 9(30), 16470-16478.

[3] **Xu Dan.**, Lu, L. (2021). Efficient and anti-salt Cu plasmonic enhanced porous solar evaporator, Energy proceedings. (ICAE 2021 Conference paper)

[4] **Xu Dan.,** Xu, S. P., Lu, L. Flexoelectric energy harvesting achieved by external polarization of nonpolar single-walled carbon nanotubes. To be submitted.

[5] **Xu Dan.,** Lu, L. The advanced strategy of polymeric materials and structure engineering for solar steam generation: challenges and prospective. To be submitted.

Acknowledgements

In this section, I would like to express my sincere gratitude and respect to the individuals who have supported and assisted me during my Ph.D. studies.

I would like to extend my sincerest thanks to my supervisor, Professor Lin Lu, for her professional and patient guidance throughout my Ph.D. research journey. Her meticulous and responsible approach has not only motivated me to overcome challenges and strive for continuous improvement in research but has also provided meaningful advice in various aspects of life. Being part of Professor Lin's research group and under her encouraging guidance, I have been able to communicate seamlessly with group members from diverse disciplines. Professor Lin's open-minded, inclusive, motivating, and rigorous scientific attitude has immensely contributed to my Ph.D. research and personal growth, providing me with invaluable guidance for future research, and life. I would also like to express my gratitude to my colleagues in Professor Lu's research group for their support and assistance throughout these years.

I also would like to convey my deepest appreciation to my co-supervisor, Dr. Hanjie Guo, from Songshan Lake Materials Laboratory, for his selfless help during my one-year work and study in the laboratory. His assistance in setting up experimental setups, conducting tests, and providing guidance in paper writing has been invaluable. Lastly, I would like to thank my family. Without their unwavering support and assistance, I would not have been able to accomplish my Ph.D. work.

Table of Contents

List of Figures

List of Tables

Chapter 1
Introduction

In this chapter, the research background of developing new nanomaterials for the harnessing of emerging renewable energy will be introduced. Additionally, based on the research background, the research objectives of this thesis will be presented. Furthermore, the organizational structure of this thesis will be outlined in this chapter.

1.1 Research background

Fossil fuels are exhaustible, and their combustion is the primary cause of the extensive greenhouse gas emission. It is projected that the global energy supply will double to meet the ever-growing demand by 2050 [1]. Meanwhile, driven by the population growth and rapid industrialization, the energy crisis has emerged as a vital concern to the whole society. The energy crisis has garnered increasing interest due to its implication for global climate change and environmental concerns. In the past few decades, considerate efforts have been made to explore promising solutions to address environmental and energy challenges. Green and renewable energies have emerged as the alternatives to alleviate the energy crisis and adverse environmental effects [2]. While efficient energy utilization through energy conversion process and storage is crucial to the development and application of renewable energy technologies. For instance, finding reliable ways for efficient clean energy production and convenient energy storage is of paramount importance. Firstly, the utilization of renewable energy requires efficient conversion of diverse renewable energy resources into available fuels. There is a need for efficient conversion of energy from renewable or inexhaustible sources into usable forms such as electricity or fuels [3]. Furthermore, there is a growing demand for efficient, affordable, and environmentally friendly energy storage solutions to complement the emerging power generation systems. This is particularly important due to the intermittent and off-grid nature of many renewable energy sources. As a result, there is an increasing need for the development of supercapacitors and rechargeable batteries based on lithium technology to meet these requirements [4].

Since the oil crisis in the 1970s, significant efforts have been made to explore available renewable energy recourses [5]. Earth's abundant renewable energy resources include wind energy, biomass, photovoltaics, and geothermal energy [6-8]. For example, biomass, when converted to energy, can help absorb carbon dioxide during its growth. In recent decades, there have been significant advancements in the application of renewable energy technologies. Photovoltaic technology, which converts solar energy into electricity via semiconductor materials, is one of the commercialized techniques of renewable energy conversion. The focus of photovoltaic technology relies on the development of novel and efficient semiconductor materials and device design [9]. Beyond electricity generation, when concentrating on solar power, it can also be utilized for other needs of direct heating via photothermal process in various emerging energy-related fields, such as solar - thermal power generation, seawater desalination [10, 11]. Recently, solar-driven interfacial evaporation is a direct application of solar-thermal conversion for clean water harvesting [12]. Hydrogen, due to its cleanness and high energy efficiency, is another substitute of fossil fuels. In recent decades, explorations in hydrogen technologies have shown promise in reducing global carbon dioxide emission, particularly in heating, fuel cells and other portable power [13]. For instance, water splitting for hydrogen evolution, taking advantage of the abundance of water on earth, is a cost-saving and highly efficient method to assure the long-term and massive hydrogen production [14].

1.2 The utilization of nanomaterials for enhancing renewable energy harness

Nowadays, low carbon energy is an approach that assures energy security for the whole society. For the exploitation of low carbon energy, from the aspect of materials, the development of nanotechnology contributes a lot in the wide ranges of application, such as in solar cells, hydrogen generation, hydrogen storage, and fuel cells [15]. As one of the most earth available sources, solar energy is the promising renewable energy resource that can meet the ever-growing demand. Up to now, the developed and applied solar energy technologies contain Solar Thermoelectricity (STE), Photovoltaic Solar Panels (PV), Concentrated solar power (CSP), Concentrated Photovoltaic (CPV), Dye Sensitized Solar Cell (DSSC), and so on [16-19]. The description of nanotechnology is board， but generally it indicates the material or phenomena at nano scale. Nanomaterials employed in the field of solar energy conversion can be categorized based on their intended application. For example, nanomaterials have been applied in solar collectors, solar cells, PV, photocatalysis [20, 21]. The solar energy conversion (e.g., solar-to-heat, solar-to-electricity) is the key step of all solar energy techniques. The increasing focus on solar energy conversion and the corresponding research and development of materials has been driven by multiple factors. Moreover, the widespread adoption of solar-powered devices utilizing nanomaterials has demonstrated the potential to bring about a transformative impact on global economic growth.

Over the past few decades, considerable progress has been made in the advancement of nanomaterials for the purpose of renewable energy, including their synthesis, properties, and application. Compared to macroscopic materials, nanomaterials exhibit different chemical, optical, and electrical properties due to their size effects, resulting in larger specific surface areas and enhanced reactivity [22]. Nanomaterials can serve as catalysts, playing a crucial role in renewable energy conversion and storage [23]. For instance, metallic catalysts in the form of nanoscale particles can be used for hydrogen production through water electrolysis, while nanostructured catalysts can facilitate the conversion of biomass into fuels or chemicals [24]. Moreover, nanomaterials have significant applications in energy storage. Nanostructured electrode materials, such as nanoparticles in lithium-ion battery materials, can improve energy density and charge/discharge rates [25]. Additionally, nanomaterials are utilized in energy storage devices such as supercapacitors, and hydrogen storage materials [26]. Nanomaterials also play a vital role in solar thermal utilization, where they can function as heat absorbers to enhance the absorption efficiency of solar thermal collectors and improve overall conversion efficiency for various applications [27]. Furthermore, nanostructured thermal insulation materials can be used to enhance the efficiency of thermoelectric conversion devices. The mechanical properties and mechanical energy conversion characteristics of nanomaterials make them crucial materials in the field of mechanical energy utilization. For instance, nanogenerators convert mechanical energy into electrical energy, harnessing vibrations, pressure, or fluid movement as forms of mechanical energy sources. Take carbon nanomaterials for instance, which contain carbon nanotubes and graphene. And, the Graphene, a typical a single or few layers of 2-D structured sp2-bonded carbon sheets, attaching a great deal of interests in many fields. Specifically, because of its exceptional properties in electrical, thermal, chemical, mechanical, and optical and large specific surface areas, great efforts have to be taken to exploit its application in solar cells, fuel cells, supercapacitor, lithium-ion batteries. In conclusion, nanomaterials have broad applications in enhancing the renewable energy harness.

1.3 Objectives of the thesis

The carbon nanomaterial family, including carbon nanotubes (CNTs), graphene, and carbon nanofibers, has attracted great attention in renewable energy application, due to their unique properties such as large specific surface areas, good electrical conductivity, and good thermal stability. In summary, carbon nanomaterials play important roles in the utilization of renewable energy, promoting advancements in energy storage, solar cells, catalysis, energy conversion, and electrocatalysis. Furthermore, due to their renewable nature, low environmental impact, and recyclability, carbon nanomaterials hold promise as candidate materials to address future energy challenges with high energy efficiency. However, given the complex and expensive synthesis process of carbon nanomaterials, the facile preparation of novel and efficient and stable carbon-based nanocomposites holds crucial significance for enhancing their utilization in renewable energy applications. To efficiently develop and utilize renewable energy, the creation of new materials and associated manufacturing technology is one of the key directions. Therefore, this thesis utilized innovative fabrication strategies to obtain novel carbon-based nanomaterials and investigated their performance in emerging renewable energy applications. This research primarily aims to achieve three specific research objectives as described below:

1．To design and construct 3D-carbon based nanomaterials and explore the application in electrolytic Hydrogen production；

2. To fabricate multidimensional-carbon based composites for solar thermal harvesting and utilization；

3. To investigate the strategy of modifying single-walled carbon nanotubes for mechanical energy harvesting via enhanced flexoelectric effect**.**

1.4 Organization of thesis

This section provides an overview of the thesis and the content of each chapter. In this thesis, the focus is on the preparation of novel carbon nanocomposite materials and their applications in the emerging fields of renewable energy conversion and utilization. Accordingly, the thesis includes fabrication and structural design of materials and explores the performance of three types of novel carbon nanocomposite materials in electrolytic hydrogen production, photothermal utilization, and interface-enhanced flexoelectric effects, thereby expanding the applications of novel carbon nanomaterials.

Chapter 1: This chapter introduces the research background of this thesis. It also highlights the significance of developing reliable nanomaterials in enhancing renewable energy harness to address energy and environmental issues. Based on the current development of nanomaterials for renewable energy utilization, three research tasks are proposed in this study.

Chapter 2: This chapter provides a comprehensive review of the research status both domestically and internationally. The review focuses on the emerging renewable energy harvesting and utilization, and development of advanced carbon nanostructured materials.

Chapter 3: This chapter presents the work titled "One-step fabrication of laser-induced forward transfer graphene/CuxO nanocomposite-based electrode to promote hydrogen evolution reaction activity." The work primarily discusses the performance and reliability of the newly fabricated electrode, which serves as a catalyst support for electrolytic water splitting. It covers various aspects, including equipment, fabrication processes, material preparation, and characterization.

Chapter 4: This chapter introduces the work titled "Efficient solar evaporation with self-desalting based on laser-assisted plasmonic Cu/Graphene nanocomposite." The work primarily focuses on the utilization of the newly developed laser-induced graphene composite and its microstructure characteristics for solar energy capture, photothermal conversion, and direct freshwater generation through interfacial seawater evaporation. It encompasses equipment, fabrication processes, material preparation, and characterization of the evaporator's performance, including photothermal effects, evaporation rate, salt removal efficiency, and structural stability.

Chapter 5: This chapter presents the work titled "Flexoelectric energy harvesting achieved by external polarization of nonpolar single-walled carbon nanotubes." It primarily investigates the construction of engineered interfaces using polarizable molecules within carbon nanotubes. The chapter explores the effect of force-electric coupling mechanisms on generating electricity by studying I-V curves through atomic force microscopy. It also examines the enhancement mechanism of flexoelectric effects using atomic force microscopy for capacitance, piezoelectric, and viscoelastic modes.

Chapter 6: This chapter concludes the thesis and provides prospects. It presents conclusions based on the three works conducted in this study and outlines research ideas to address the current and future challenges.

Chapter 2
Literature review

This chapter primarily encompasses a review of relevant domestic and international literature studies to the research topic of this thesis. It includes an overview of the current research status in three aspects of emerging renewable energy application: solar thermal utilization, water electrolysis for hydrogen production, and nanomechanical energy harvesting. Additionally, a literature review is presented on the carbon nanomaterial family, including their preparation, modification, and applications. Subsequently, the chapter introduces the trends in emerging carbon nanomaterials, including fabrication methods and potential applications. Furthermore, the distinctive features of laser-induced porous materials preparation, as well as their properties and applications, are outlined. Finally, based on the literature review, the chapter identifies the existing challenges in the reliable and functionalized fabrication of carbon nanomaterials and proposes a research flowchart for this study.

2.1 Emerging renewable energy harvesting and utilization

In recent years, there have been several emerging trends and technologies in the field of renewable energy collection and utilization. Natural and artificial energy sources have sparked extensive research on energy harvesting and conversion techniques. For example, solar energy remains a significant focus in renewable energy, with advancements in solar panels such as the use of perovskite materials and multi-crystalline cells, leading to increased efficiency and reduced costs. Furthermore, solar energy is being integrated into various new applications in building environments, including building-integrated photovoltaics (BIPV), solar windows, and solar-driven desalination [28]. Hydrogen is a versatile and clean energy carrier that can be produced using renewable energy through water electrolysis. Research is underway on the utilization of hydrogen fuel cells in transportation, power generation, and industrial processes, offering a clean and efficient alternative to fossil fuels. Meanwhile, mechanical energy, including wind, waves, machine vibration, and even human motion, is being collected and utilized by various mechanical energy harvesters. This section will introduce status and trends of research in three aspects, including solar thermal utilization, water electrolysis for hydrogen production, and nanomechanical energy harvesting.

2.1.1 Solar-thermal energy harvesting and utilization

The abundant solar energy has been regarded as one of the ideal renewable energy sources to address the urgent energy crisis on earth. The sunlight in the form of a naturally electromagnetic wave could be absorbed and transferred to the diverse forms of energy including electricity, chemical energy, and heat [11, 29]. According to the distinction of energy conversion, there are four main mechanisms for solar energy conversion, including the photovoltaic effect, photochemical reactions, photothermal effect, and photobiological processes [30-33]. The photovoltaic effect follows the principle of the photoelectric effect, using semiconductor materials in photovoltaic cells to directly convert solar energy into electricity. It is the most common and widely applied mechanism for solar energy conversion. Specifically, when sunlight shines on the surface of a photovoltaic cell/material, photons (particles of sunlight) excite electrons in the cell, causing them to transition to the conduction band, thereby generating electric current [34]. This current can be collected and utilized, supplying power to buildings, or injecting it into the power grid. Photochemical reactions are another mechanism for solar energy to drive chemical reactions. In photochemical reactions, photons excite electrons in molecules or materials, leading to electron transitions and the breaking or formation of chemical bonds [35]. These photocatalytic reactions can be used for water splitting to produce hydrogen and oxygen. Note that, compared with other 3 types of solar energy conversion modes induced by the photoexcitation, the photothermal effect shows the highest conversion efficiency [23]. The photothermal effect utilizes the energy of sunlight to generate heat and is achieved through photothermal materials [36]. Photobiological processes harness the energy of sunlight to drive metabolic activities in organisms [37]. Photosynthesis is the most typical photobiological process. Additionally, photobiology can be applied in areas such as biofuel production through photosynthesis and bio-photovoltaic reactions.

Different solar energy conversion mechanisms play important roles in various application fields, providing multiple pathways for developing sustainable energy and clean technologies. Currently, due to the advancement of high-efficiency semiconductor photovoltaic materials, design and optimization of system structures, and efficient energy management of photovoltaic systems, the photovoltaic effect is the most widely applied mechanism with the highest efficiency for solar energy conversion. Seeing that the photothermal effect is one of the most energy-efficient mechanisms, the optical utilization of solar thermal energy has been a hot topic. The key foundation for solar thermal utilization lies in the efficient photothermal materials and structures. Typically, photothermal materials include carbon materials, semiconductor materials, conductive polymers, and certain metal nanoparticles, each with different photothermal principles (Figure 2.1, Figure 2.2) [38, 39]. The photothermal principles of materials involve light absorption and photothermal conversion. For carbon materials, such as carbon nanotubes and graphene, they possess high light absorption capacity [40]. When sunlight shines on the surface of carbon materials, the π-electron energy level structure allows them to absorb photons within the visible and near-infrared spectral range. By absorbing the energy of the photons, electrons transition to higher energy levels in the band, thereby converting light energy into electron excitation energy or excited states. Through non-radiative internal relaxation processes, the energy is converted into lattice vibrations, generating heat. Some carbon materials can induce photothermal reactions and produce heat through surface structures. For certain conductive molecular materials (e.g., polyaniline, polythiophene), they also exhibit high light absorption capacity [41]. When absorbed photons interact with polymer molecules or segments, they cause electron excitation to higher energy levels, forming excited states. Through non-radiative internal conversion, light energy is converted into vibrational energy of molecules or polymer chains, resulting in heat generation. As for semiconductor materials (such as silicon, cadmium selenide), they also possess high light absorption capacity [42]. When exposed to sunlight, the energy of photons is absorbed, prompting electrons in the semiconductor material to transition from the valence band to the conduction band, forming electron-hole pairs. It is noteworthy that the band structure of semiconductor materials can be adjusted to absorb photons of specific wavelength ranges. The photothermal conversion of semiconductor materials occurs through two mechanisms. One is non-radiative internal conversion to lattice vibration energy, generating heat. The other mechanism involves carrier recombination, where photogenerated electron-hole pairs recombine in the semiconductor material, releasing energy and generating heat. For metal materials, they exhibit high reflectivity to visible and near-infrared light, while their absorption capacity for ultraviolet and far-infrared light is weak. Metal materials are not ideal for photothermal applications. However, metal nanoparticles can absorb incident light energy at specific wavelengths through surface plasmon resonance, which is due to the absorption by free electrons in the material. Similarly, the excited electrons interact with lattice vibrations inside the material, converting light energy into heat energy. This process is commonly referred to as non-radiative decay.

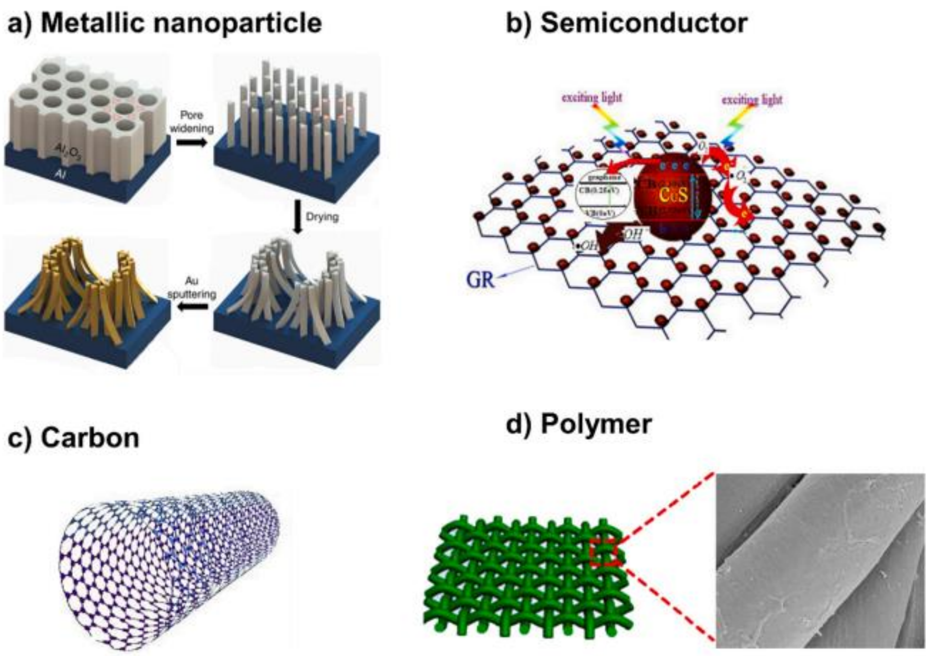

Figure 2.1 Four typical photothermal materials: metallic nanoparticles, (b) semiconductor, (c) carbon materials, (d) conductive polymer [38]

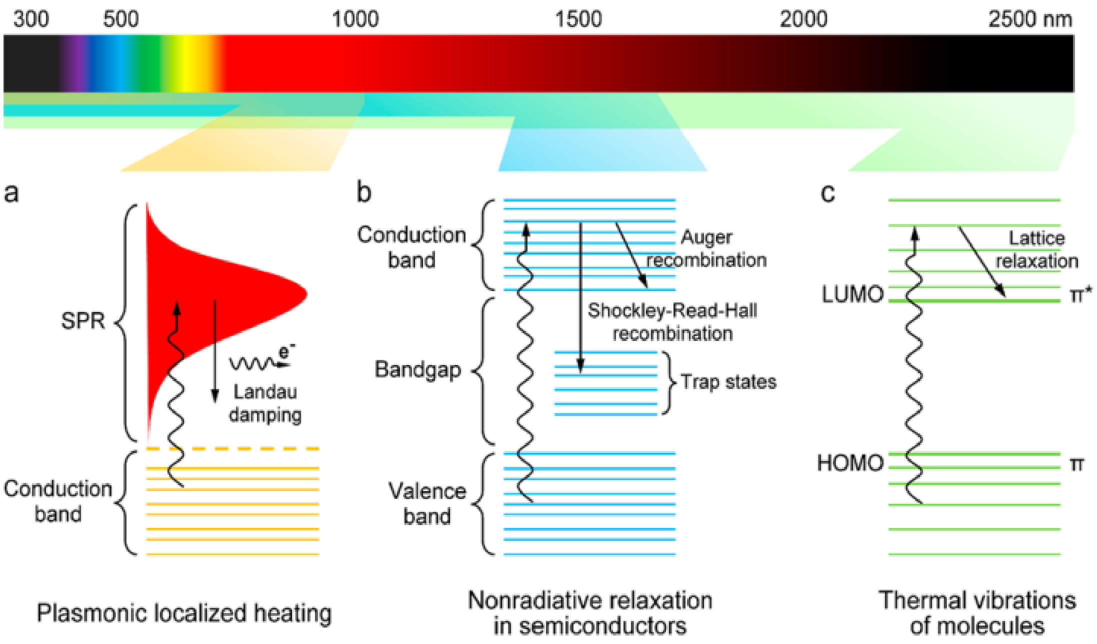

Figure 2.2 Mechanisms of the photothermal effect [39]

Emerging photothermal utilization refers to the growing field of applications that harness photothermal effects for various energy and environmental purposes. One such and significant application is photothermal-driven water nexus, which includes water harvesting, water purification and production, membrane distillation, photocatalysis (Figure 2.3) [43-49]. Nanomaterials have gained a lot of attention for photothermal enhanced water harvesting. For example, the use of nanostructured materials with high surface area can enhance water evaporation rates, thereby improving water harvesting efficiency. Additionally, nanomaterials can be used to design self-cleaning surfaces or anti-fouling coatings to enhance the performance of water collection facilities. Nanotechnology plays a crucial role in photothermal enhanced water purification processes. Nanoparticles can be employed as adsorbents to remove contaminants from water, such as heavy metal ions, organic compounds, and microorganisms. Moreover, nanoscale photocatalysts can utilize photothermal effects for photocatalytic oxidation, facilitating the decomposition of organic pollutants.

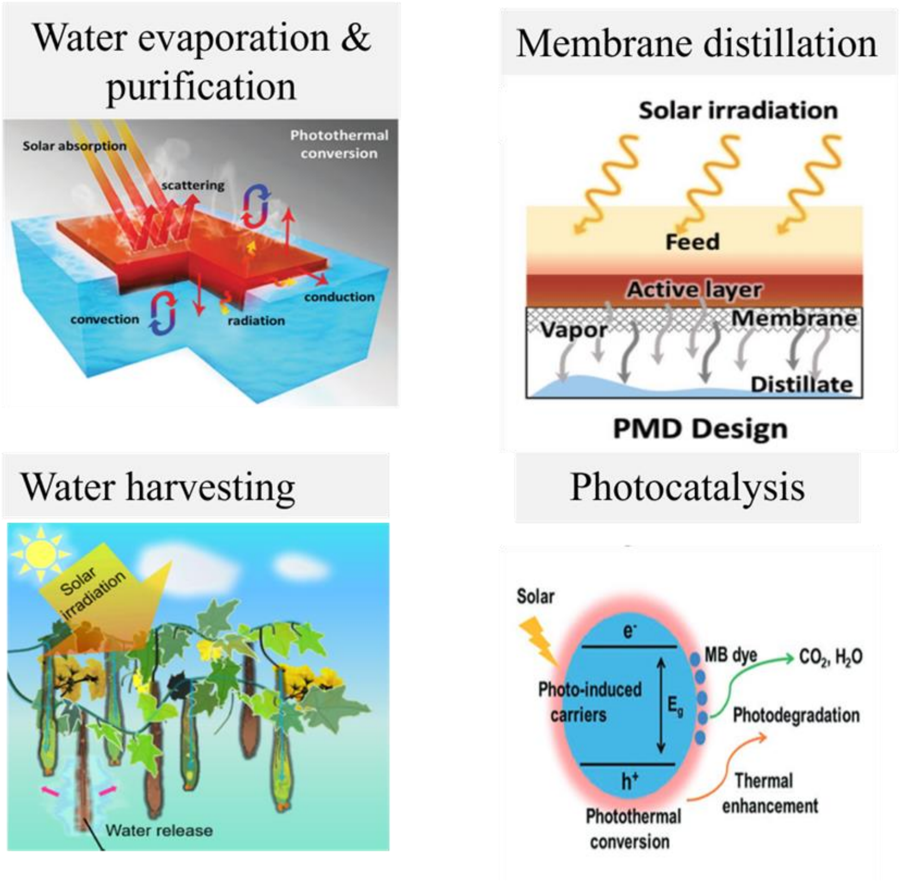

Figure 2.3 Photothermal assisted- water nexus [46-49]

Research on nanomaterials also contributes to innovations in water production. For instance, nanoporous materials can be used in distillation and evaporation systems to enhance water separation and purification efficiency. Additionally, the surface properties of nanomaterials can be utilized in membrane separation processes to achieve efficient water treatment and desalination. In these areas, the development of nanotechnology offers new possibilities for photothermal-driven water-related applications. Through the design and engineering of nanomaterials, more efficient, energy-saving, and environmentally friendly utilization of water resources can be achieved. However, further research and experimentation are still needed to determine the practical performance of nanomaterials in real-world applications and their implications for the environment and human health.

2.1.2 Hydrogen harvesting from water electrolysis

Hydrogen is an efficient and clean energy source that, when burned, only produces water vapor without releasing harmful substances or greenhouse gases. Therefore, hydrogen is considered a clean energy alternative. Hydrogen production is an important energy conversion process that has been widely studied and applied. Steam reforming is the most used industrial method for hydrogen production [50]. It relies on fossil fuels, such as natural gas or liquefied petroleum gas, which react with steam via a catalyst to generate hydrogen and carbon dioxide. However, this process is highly dependent on fossil fuels and results in high carbon dioxide emissions. Water electrolysis is to directly split water to generate hydrogen and oxygen [51]. An electric current passes through an electrolyte in water (such as alkaline solution or polymer electrolyte membrane) to generate hydrogen at the cathode while oxygen at the anode. Combined with the renewable energy sources, it is considered a clean method of hydrogen production (Figure 2.4) [52, 53]. Photolysis of water is a process that uses solar energy to produce hydrogen gas. This typically requires the use of photoelectrochemical catalysts (such as titanium dioxide) to absorb solar energy and catalyze the decomposition reaction of water [54]. Currently, this method is still in the research stage. Biomass fermentation is the conversion of organic materials (such as biomass, waste, or wastewater) into hydrogen gas using microorganisms [55].

However, this method requires dealing with enormous amounts of biomass resources and managing organic waste generated during the hydrogen production process. Low-temperature plasma reforming is a novel method of hydrogen production that utilizes low-temperature plasma to catalytically reform hydrocarbon compounds [56]. The high-energy electrons and ions generated by plasma can activate chemical reactions at low temperatures, breaking hydrocarbon compounds down into hydrogen and other useful products.

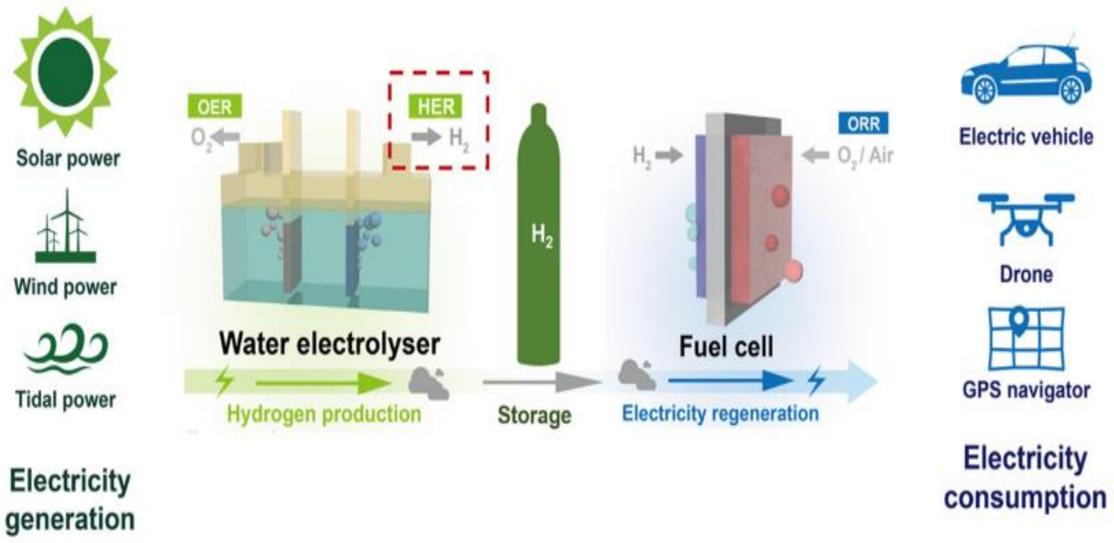

Figure 2.4 Sustainable hydrogen energy supply route [53]

Recent years, water electrolysis has gained widespread attention due to its obvious advantages in the hydrogen production. Firstly, the electricity used in water electrolysis can be generated from renewable energy sources. This means that hydrogen produced through water electrolysis can achieve zero emissions throughout the entire process. The significance lies in the fact that water electrolysis can be a crucial component of clean energy systems, reducing dependence on fossil fuels and addressing environmental issues. Water electrolysis is an efficient energy conversion process. It has been reported that the energy conversion efficiency of water electrolysis can reach around 80-90% in practical applications [57]. Secondly, water electrolysis offers a flexible energy storage solution. Hydrogen can be stored and released as needed. Water electrolysis can also be combined with renewable energy systems to balance the differences in energy supply and demand. For example, when there is excess electricity from renewable energy sources, it can be used for water electrolysis to convert it into stored hydrogen. When in high energy demand periods, the stored hydrogen can be used to generate electricity again through fuel cells. Furthermore, hydrogen produced through water electrolysis typically achieves purity levels of over 99.9% [58]. This high-purity energy is suitable for various applications in fields such as fuel cells, chemical industries, and electronics. With the continuous development of renewable energy sources and improvements in water electrolysis technology, water electrolysis is promising to become a vital component of energy systems, promoting the widespread use and sustainable development of clean energy. Despite many advantages, the widespread adoption of this technology still faces challenges such as energy losses during electrolysis, costs associated with electrolysis equipment and hydrogen storage facilities, and overall system efficiency.

The deployment of portable electrolysis has the potential to drive the installation of market-driven refueling stations, but the cost and stability issues would be increased due to the use of highly acidic proton exchange membranes (PEMs) or systems [59]. The associated issues with electrolytic hydrogen production are also reflected in the excessive cost of precious metal-based materials for hydrogen evolution reactions and that from increased the operational, maintenance, and safety expense of the entire setup due to the highly corrosive conditions. Therefore, developing alternative catalysts and reaction media is an urgent need for the dependable, scalable, and sustainable implementation of electrolytic hydrogen production. However, despite the increased stability of water electrolysis devices under alkaline conditions, alkaline hydrogen evolution reaction (HER) technology faces a significant challenge in the reduction of hydrogen kinetics in this reaction medium. Thus, developing non-precious catalysts with high efficiency for electrolytic hydrogen production is highly imperative [60].

In alkaline water electrolysis, alkaline water electrolysis (AWE) operates at temperatures ranging from 20-80°C and has a theoretical efficiency of 59-70% [61]. In this process, the oxygen evolution reaction (OER) and the hydrogen evolution reaction (HER) occur at the anode and cathode respectively [62]. In a water electrolysis device, the ideal electrodes should possess the following characteristics: (1) large surface areas to provide rich active sites, (2) good electronic conductivity, (3) long-term stability to support continuous operation, (4) high intrinsic activity of the catalyst toward the electrochemical reactions at the electrodes.

Two main strategies of improving their intrinsic activity and increasing active sites are used to enhance the performance of electrocatalysts for water electrolysis [63]. To improve the intrinsic activity, strategies applied on the catalysts like heteroatom doping, strain engineering, or alloying can be employed [64]. While porous structures or constructing nanomorphology would provide more active sites. Modifying the electronic structure of the electrocatalysts aims to improve their electronic conductivity, thereby enhancing the reaction efficiency. In recent years, large non-precious metal-based catalysts have been synthesized for alkaline water electrolysis to achieve efficient hydrogen evolution reaction (HER). These include transition metal phosphides (TMPs), transition metal dichalcogenides (TMDs), transition metal oxides (TMOs), and modified carbon materials [65-67]. TMPs are characterized by a trigonal prismatic crystal structure, with metal/covalent chemical bonding. Depending on the phosphorus content, the same TMPs can exhibit various phases, and they can display either semiconductor or metallic properties [68]. TMPs can be synthesized through methods of solid-state reactions, solvothermal processes, and electrodeposition. Starting from Schaak and colleagues' initial attempts to apply TMPs as HER catalysts in alkaline solutions, the current alkaline HER catalysts based on TMPs include novel nickel, cobalt, iron, molybdenum, tungsten, and copper phosphides. Another class of catalysts commonly used for HER in electrolysis is transition metal dichalcogenides (TMDs), where M refers to the transition metal, such as Mo or W, and X refers to sulfur, selenium, or tellurium as the chalcogen elements [69]. Structurally, TMDs consist of multiple tri-layers stacked by van der Waals interactions, with a transition metal layer in the middle of two layers of chalcogen elements [70]. The anisotropic featured by this unique structure, leading in different HER activities on the basal and edge planes. Among various TMDs, MoS2 is a popular catalytic material for HER because of its near-optimal hydrogen binding. Due to its less ideal conductivity and weaker adsorption capability towards hydroxyl species, its catalytic performance for HER in alkaline electrolytes is weakened [71]. Adjusting the electronic structure o by doping has been proposed to enhance the conductivity and HER catalytic performance of MoS_2. Initially, transition metal oxides (TMOs) were considered inert catalysts for HER due to their weak hydrogen adsorption ability. However, by combining them with highly conductive or high surface area materials, they can exhibit improved HER catalytic activity. Carbon materials are commonly used as conductive supports for electrode fabrication, due to their low cost, large surface areas, high conductivity, and multifunctionality. At the same time， methods including surface functionalization, porous structure fabrication, heteroatom doping, and defect engineering, and edge tailoring are used to improve the structural, electronic and electrochemical properties of carbon materials for HER catalyst [72].

2.1.3 Nano-mechanical energy harvesting

Energy can be directly harvested from renewable sources, including wind energy, ocean waves, solar radiation, raindrops, biomechanical motion, body heat, sound, and railway vibrations [73]. Meanwhile，battery limitations, such as low energy density, limited lifespan, bulky size, risk of overcharging, and high cost，and recycling, have restricted their application in electronic devices [74]. Over the past decades, advanced manufacturing has changed the perception of nanoscale mechanical energy harvesting (NMEH). For instance, innovative electronic applications have seen the widespread adoption of low power NMEH systems. These systems find utility in various fields, like biomedical health monitoring, mobile phones, smartwatches, self-powered wireless sensor, desalination technologies, marine navigation systems [75]. Nanomaterial-based mechanical energy harvesting is an energy conversion and collection process that utilizes nanoscale materials and structures. It relies on fundamental physical principles and mechanisms of energy conversion and acquisition, including the piezoelectric effect, electromagnetic induction, surface effects, and mechanical resonance. Take piezoelectric effect for example, polarization occurs when a material is subjected to forces or pressures, resulting in charge separation. At the nanoscale, piezoelectric materials can induce charge separation through strain or pressure, thereby converting mechanical energy into electrical energy. In the case of nanoscale conductor structures, external vibrations or motion can be used to induce current, enabling the conversion of mechanical energy into electricity for utilization. Surface effects are based on the unique physical properties exhibited by nanoscale structures and materials on their surfaces, such as surface diffusion and surface charge separation. These surface effects can be utilized to convert mechanical energy into electricity for energy harvesting. Another example is mechanical resonance-based energy harvesting using nanomaterials [76]. By designing the geometric shape and material properties of nanoscale structures to resonate at specific frequencies, energy conversion and collection can be achieved when subjected to external mechanical vibrations or oscillations.

2.2 Development of advanced carbon-based nanomaterials

Due to its abundance, accessibility, stability, as well as its excellent thermal conductivity, electrical conductivity, and chemical stability, carbon materials show immense potential in application for addressing energy and environmental challenges. Based on different bonding of carbon atoms, carbon materials can be broadly classified into four groups [77]. The first category includes materials with fully sp2 hybridized bonds, such as graphite, carbon nanotubes, and graphene [78]. The second group includes materials with a combination of sp2 and sp3 hybridized bonds, such as amorphous carbon [79]. The third category includes materials with purely sp3 hybridized bonds. And the fourth category includes carbon chains with sp hybridized bonds. To date, the development of carbon nanomaterials and structures primarily includes graphene, carbon nanotubes, fullerenes, carbon quantum dots, carbon nanofibers, and carbon-based aerogels [80]. The development of new carbon-based nanomaterials involves various approaches. Firstly, there have been improvements in synthesis methods, including chemical vapor deposition, electrochemical deposition, electrospinning, and wet chemical methods [81]. Secondly, surface functionalization is another approach to develop new carbon-based materials, achieved through chemical modification, polymer coating, or the introduction of functional metals or materials onto the surface of carbon nanomaterials. Thirdly, structural control and manipulation of carbon nanomaterials, such as controlling the aspect ratio of carbon nanotubes or the morphology of graphene, to achieve unique properties. Additionally, the development of carbon nanomaterial allotropes, such as carbon quantum dots, carbon nanoribbons, and carbon nanospheres, is pursued. Furthermore, expanding their applications in electronics, energy, biomedicine, and environmental science is an important focus [82]. In summary, the current development of carbon nanomaterials and structures encompasses graphene, carbon nanotubes, fullerenes, carbon quantum dots, carbon nanofibers, and carbon-based aerogels. The development involves improvements in synthesis methods, surface functionalization, structural control, the discovery of new carbon nanomaterial allotropes, and the exploration of diverse applications in various fields.

2.2.1 Carbon based materials/nanostructure

Since its emergence, few-layered graphene, a prominent member of the carbon group, has garnered significant attention, due to its exceptional electrical, thermal, and mechanical features, making it highly desirable in various fields [83]. There are natural and synthetic graphite. The single-layer graphene possesses exceptional crystal quality, as well as remarkable mechanical, thermal, electrical, and optical properties [84]. The extraction of graphene involves techniques such as exfoliation and cleavage, as well as chemical vapor deposition. Exfoliation and cleavage methods aim to obtain graphene from graphite flakes and can be categorized into chemical exfoliation, cleavage, and mechanical exfoliation. Mechanical exfoliation, for instance, involves the process of peeling individual layers of graphene from the bulk graphite [85]. Ideally, this method achieves layer-by-layer extraction of graphene. In summary, few-layered graphene, with its outstanding properties, has attracted significant interest.

The mechanical exfoliation method, where graphene is peeled layer by layer, is one approach employed in the synthesis of graphene, by overcoming the resistance of the van der Waals attraction from adjacent graphene flakes [86]. The extraction of graphene from graphite can also be achieved by chemical vapor deposition (CVD) method. Since its first report in 2006 [87], large-area and high-quality graphene has been obtained. Comparing the properties of graphene produced via chemical vapor deposition (CVD) to those of exfoliated graphene, it is evident that exfoliated graphene maintains superior quality. The process of chemical vapor deposition (CVD) entails activating gaseous reactants, initiating a chemical reaction, and leading to the deposition of a stable solid film onto a compatible substrate [88]. The thermal method is commonly utilized for the growth of CVD graphene on copper and nickel surfaces, making it the predominant approach [89]. Plasma-enhanced chemical vapor depositions have been documented, which typically yield films of inferior quality compared to thermal methods. However, the conventional synthesize of graphene is quite complex, harish, not eco-friendly and not cost-effective.

The first observation of carbon nanotubes took place in 1991 [90]. They have a cylindrical shape and are formed by carbon atoms arranged in a hexagonal pattern. They can exist as single-walled or multi-walled structures with varying diameters and layers [91]. Carbon nanotubes show extremely high mechanical strength and elastic modulus, excellent electrical conductivity and thermal conductivity. They also demonstrate unique optical properties, with tunable absorption and emission wavelengths ranging from ultraviolet to near-infrared. Carbon nanotubes have unique structural and characteristic properties, including their high mechanical strength, elastic modulus, excellent electrical conductivity, thermal conductivity, and tunable optical properties. These properties make them highly versatile and applicable in various fields. Some of the key applications of carbon nanotubes include electronic devices, energy storage, catalysts and biomedical applications. Currently, there are several methods for the synthesis of carbon nanotubes including Chemical Vapor Deposition (CVD)， Arc Discharge, Wet Chemical Methods [92]. In the CVD process, at elevated temperatures, the reaction between a carbon source gas (such as methane) and a catalytic metal (such as iron, nickel, or chromium) leads to the synthesis of carbon nanotubes [93]. This method allows for controlling the diameter, length, and shape of the carbon nanotubes and eases large-scale production. Arc Discharge is another commonly used method for carbon nanotube synthesis [94]. It applied high voltage between two electrodes having a carbon source (such as graphite), leading to a powerful arc discharge and the formation of carbon nanotubes. This method can produce multi-walled carbon nanotubes. Wet chemical methods involve the use of chemical solvents and oxidants to process the carbon source, resulting in the formation of carbon nanotubes. Wet chemical methods offer lower synthesis temperatures and costs, and they also can control over the diameter of the carbon nanotubes [95]. Researchers continue to explore new synthesis methods, functionalization techniques, and applications to further expand the utility of carbon nanotubes in various fields.

2.2.2 The construction of 3-D carbon nanomaterials

3D structured carbon nanomaterials refer to carbon-based materials with three-dimensional shapes and structures. At the nanoscale, they have features like large surface areas, interconnected pores, and well-defined geometric shapes, which improve material transport properties and mechanical strength [96]. As a result, these materials have attracted extensive research in areas such as energy storage, environmental remediation, electronics, and biomedicine [83, 97, 98]. Common examples of 3D structured carbon nanomaterials include carbon nanotube sponges, graphene aerogels, carbon nanofiber sponges, and porous carbon-based materials. Taking graphene aerogel as an example, compared to 2D films, the 3D aerogel morphology is a framework having interconnected micro-/nanosheets, with layered porous structures at micro, meso, and macro scales, contributing to high specific surface area, while the macro pores provide active surface accessibility [99]. 3D graphene aerogels show ultra-low density, excellent mechanical stability, and high flexural strength, while their electronic and chemical properties are also crucial in various applications [100]. The preparation of graphene aerogels can be divided into template methods and non-template methods. For instance, non-template methods include gel casting, freeze-drying, and redox reactions [101, 102]. In recent times, the use of 3D printing technology in a layer-by-layer approach has seen a growing application in the fabrication of graphene aerogels (Figture2.5) [103-106]. This advancement allows for precise design and control over the structure of the aerogels [107]. The critical aspect of 3D printing graphene aerogels lies in developing printable inks that prove shear thinning behavior, enabling them to flow under pressure. Additionally, these inks should show a rapid transition from pseudoplastic to dilatant behavior after deposition to keep the desired shape of the printed structures. Common methods involve using polymers and SiO2 fillers to prepare homogeneous, high-viscosity printing solutions [100]. Template methods used for the fabrication of graphene structures include Chemical Vapor Deposition (CVD) and the ice template method. In CVD, carbon is deposited onto metal foam, such as nickel or copper, enabling the direct production of interconnected 3D graphene structures. By employing various templates, the network and pore structure can be adjusted accordingly. On the other hand, the ice template method controls the porous structure within the aerogel by manipulating the freezing casting direction.

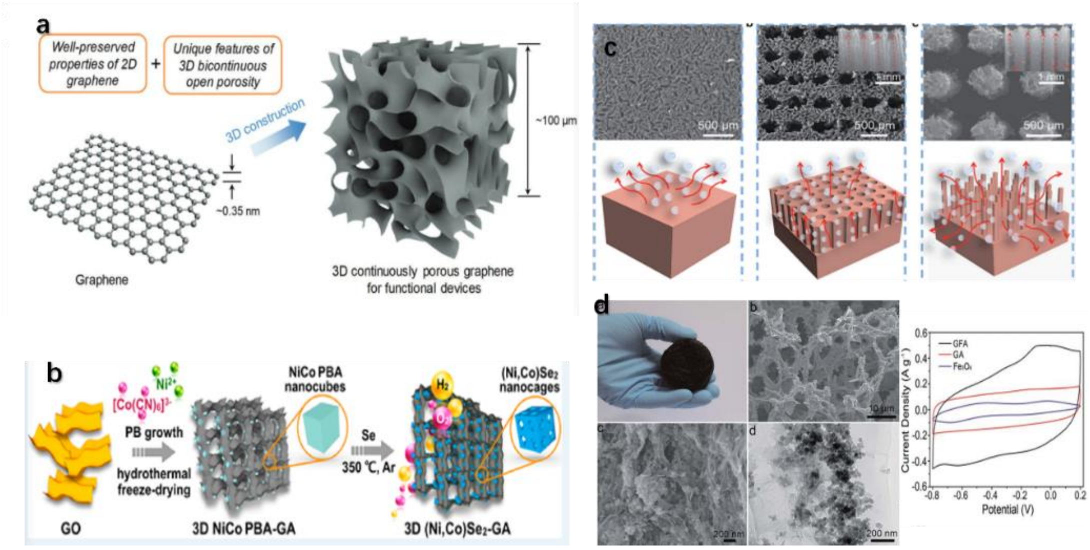

Figure 2.5 3-D carbon nanostructure for energy conversion and utilization [103-106]

2.2.3 Functionalization of carbon nanomaterials

To expand the potential applications of carbon nanomaterials and introduce specific properties or functionalities, functionalization is commonly performed by modifying their surface or structure using various chemical, physical, or biological methods [108]. The methods of functionalizing carbon nanomaterials can be broadly categorized into physical functionalization and chemical functionalization [109]. Chemical functionalization involves introducing covalent functional groups onto the surface of carbon nanomaterials, doping foreign atoms or molecules into the carbon lattice, or modifying the surface through techniques such as plasma treatment, laser irradiation, or thermal treatment [110]. Functionalizing the pristine graphene sheet is extremely challenging, as the edge sites of graphene have higher reactivity compared to the basal plane (Figure 2.6) [111]. Therefore, the dangling bonds at the graphene edges can be used for covalently attaching various chemical groups. Edge-functionalized graphene serves as a basis for further chemical functionalization. On the other hand, covalent functionalization of the graphene sheet causes significant distortion of the π conjugation, leading to pronounced changes of the properties. Non-covalent functionalization, however, induces relatively minor changes to its structure. Additionally, carbon nanomaterials can be incorporated into composites with polymers, metals, or ceramics to enhance mechanical strength, electrical and thermal conductivity of the composite materials [101, 102].

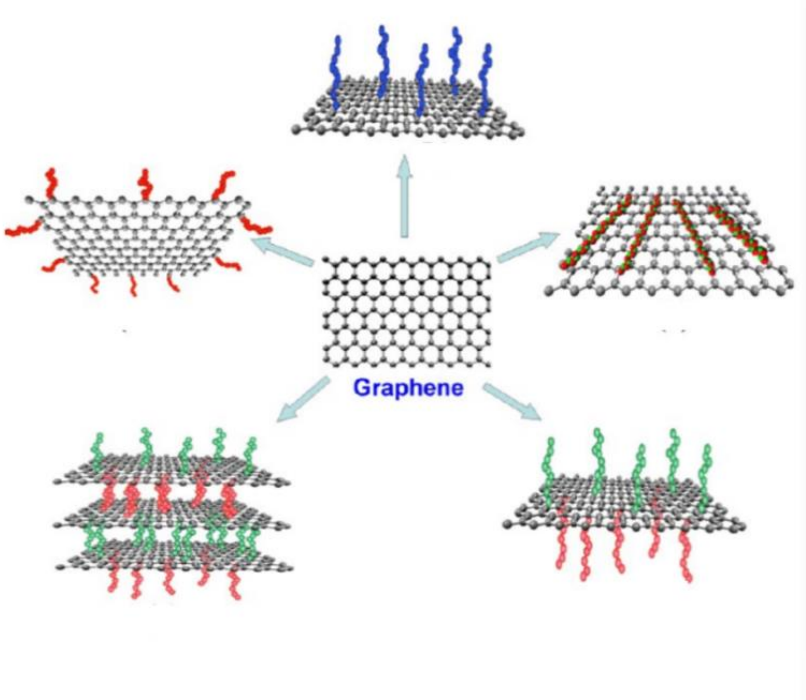

Figure 2.6 Functionalization of graphene [111]

2.3 The development of laser-induced graphene

2.3.1 Laser induced graphene (LIG): fabrication, structure, properties

Originally, the tip-based localized-thermal process was studied for nano range patterning and reducing Graphene Oxide to improve its electrical conductivity [112, 113]. This type of direct method to fabricate reduced GO offered a novel approach for micro-supercapacitor's design and application. Later in 2013, Richard B. Kaner and Maher F. El-Kady successfully made a micro-supercapacitor with high power density of 200 Wcm^{-3} based on few-layered graphene from laser writing the GO/ PET film on DVD device [114]. Earlier research demonstrated that direct laser writing was a promising and scalable, fast, and low-cost method to provide rapid localized photothermal energy for the fabrication and patterning of few layered-reduced Graphene. However, the correlation of the properties and structure formation was not clear. Then in 2014, the porous structured Graphene was obtained by James M. Tour’s group from Polyimide sheet (PI) in ambient condition via CO2 Laser process [115]. A one-step photo-thermal process was successfully employed for the first time to transform a commercial polymer film into a three-dimensional structured graphene. In contrast to using graphene oxide (GO) as the precursor, this direct patterning of polymeric sheets displayed several advantages over conventional lithography methods in terms of cost-effectiveness, mask-free operation, and flexibility in device design and configuration. Moreover, this work also presented the detailed formation process of graphene under different laser influences. Compared with the glassy carbon formation from PI being heated and carbonized at high temperature or exposure in ultraviolet irradiation, this rapid photothermal effect resulted laser induced graphene has porous structure, with a large surface area of 340$m^2.g^{-1}$. According to the study, after being ablated, it can be known the carbon percentage would be increased if the laser influences higher than 2.4 W, and the nitrogen and oxygen contents would be decreased due to the break of C-N and C-O bonds (Figure 2.7). At the same time, the LIG would be insulative and the electric conductivity would be increased with the increase of laser power. What’s more, if the laser power is higher than 4.2 W, oxidation will replace thermal effect to destroy the formation and quality of Graphene, disordered-grain boundaries in the unusual ultra-polycrystalline structure would be formed. Therefore, the curvatures caused by the largely existed pentagon-heptagons in the LIG plane were the main reason of porous structures. Overall, the rapid high temperature(>2,500 ℃) would easily cause the break and release of the organic bonds in the polymer sheets hence lead to porous graphene formation. In another work, James M. Tour’s group systematically studied the parameters to affect the formation and morphologies of LIG [116]. In detail, the parameters of laser pulse, output power, wavelength, spot size can be adjusted to control the morphology growth. In this study, two wavelengths of 9.3㎛ and 10.5 ㎛ CO2 laser had been used to treat PI to synthesize porous structured graphene. In this work, it was observed that ~5 J/cm^2 will be needed to start the carbonization, upon the carbonization temperature of 700 ℃ required for PI. At the same time, the laser could provide enough energy to start the graphitization of PI, with a rapid localized temperature of up to 3000 ℃. The outgassing of the polymeric bonds will further improve the formation of pores inside the LIG. According to earlier study, by modulating the laser influence, the researcher could successfully grow LIG forest and LIG-fiber on the PI sheets (Figure 2.8(a)) [117]. The LIG-fiber was formed by the break of the Graphene sheet according to the HRTEM images. Meanwhile, combining with other fillers or treatment, LIG surfaces with functionalization can be obtained for different applications (Figure 2.8(b)) [118].

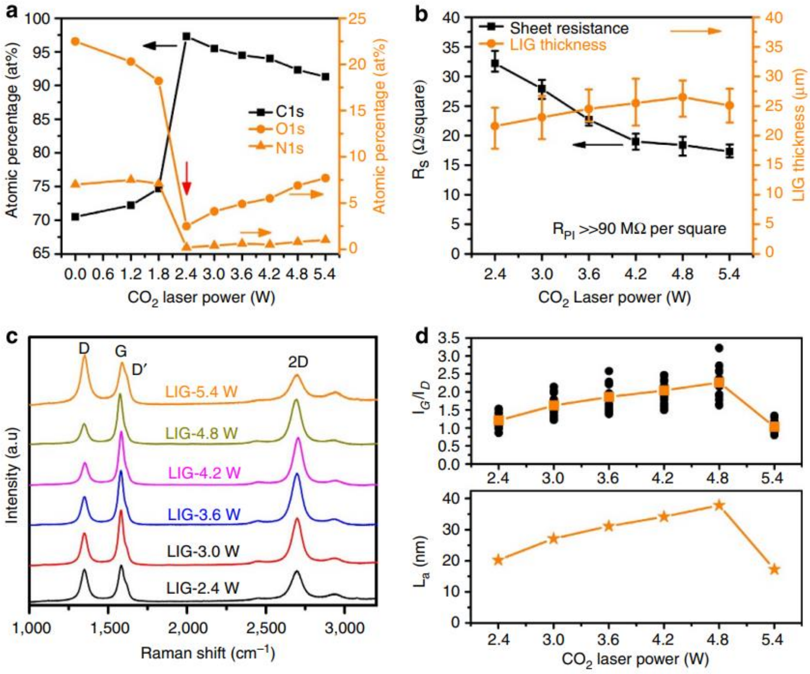

Figure 2.7 Characterizations of LIG prepared with different laser powers

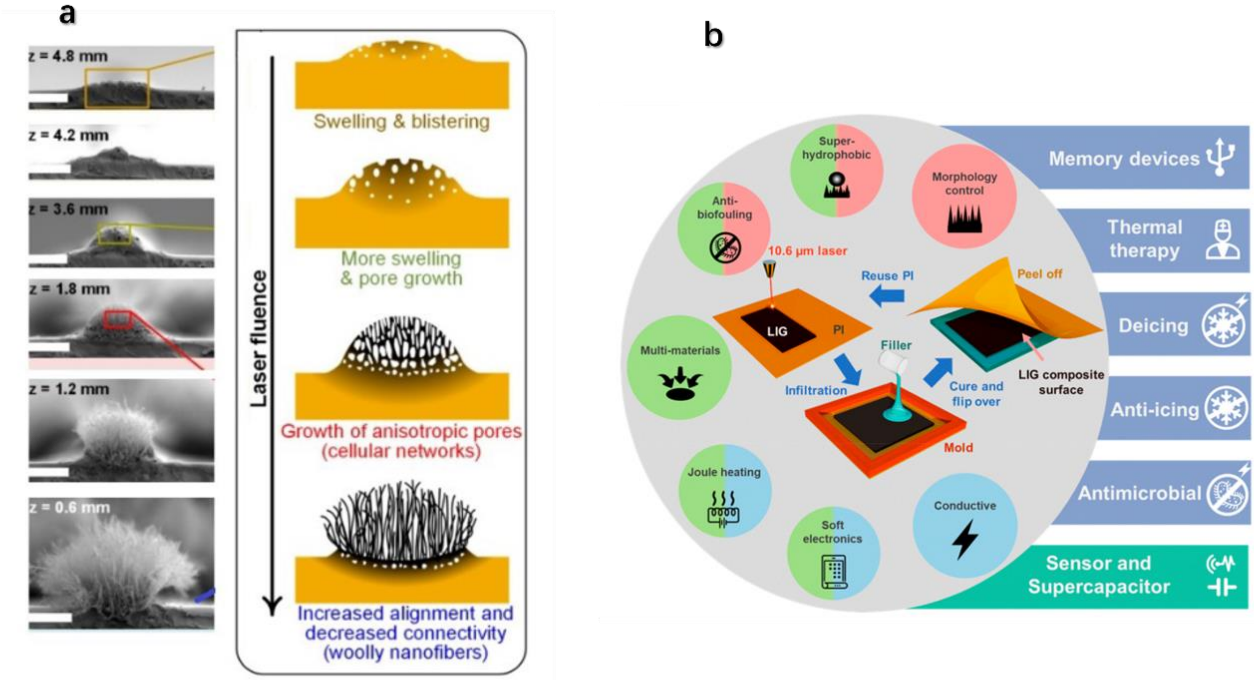

Figure 2.8 The morphological formation of the LIG nanofiber with creasing average fluence

(a) and fabrication of LIGCs with functional surfaces (b) [117-118]

Laser induced graphene is a simple and facile fabrication of graphene-based structures, as the sp3 C has been converted to sp3 C under the rapid photothermal influence. And in the plane of Graphene, it has rich heptagon and hexagon lattices structures. However, varied on the laser machine and parameter controls, the quality of LIG is different. The composition and structure of the LIG can be controlled by adjusting the parameters of the machine. Compared with Graphene made by conventional methods like mechanical exfoliation or thermal chemical methods, some research found that LIG owns poorer electrical properties due to the existence of carbohydrate groups. Jae Yeong Park’s group proved that there are rich Carboxyl groups, Hydroxyl groups, and carbon oxides that existed in LIG [86]. Moreover, they believed that these carbohydrates would decrease the electricity conductivity and increase the charge transfer resistance. Up to now, many types of polymers have been studied to fabricate LIG for specific applications，which include synthetic plastics (thermosetting and thermoplastic), natural polymers form bio-polymer, or bio-surface from plants.

2.3.2 The formation of laser induced graphene by different laser sources

Laser scribing is a facile and fast synthesis method to synthesize clustered and porous structured and layered Graphene. Up to now, there are several experimental studies that have been tried to make LIG from different substrates, but the formation mechanism and the key parameters to obtain high-quality LIG is still unrevealed. For example, how the wavelength affected the formation of LIG is still unknown. It has come to the common conclusion that the LIG synthesis under infrared Laser irradiation is a photothermal process. Hence, the conversion process and morphology of formed LIG from long wavelength laser irradiation is different from which under short wavelength laser irradiation. Take the 1064 nm IR laser for example, the photon energy is about 112.3 kJ/mol which is lower than that of the main chemical bonds in Polyimide (e.g., 332 kJ/mol of C-C ,326 kJ/mol of C-O and 305 kJ/mol of C-N). In this case, single-photon absorption can’t provide enough energy to bread the chemical bonds. At the same time, molecular vibration from multiple photon absorption will result in rapid localized temperature rise. In 2016, Jian Lin’s group tried to simulate the porous Graphene formation under extreme high pressure and high temperature from Polyimide [119]. At the same time, they used molecular dynamics to study the mechanisms of LIG formation. According to earlier studies, the temperature rise can be up to more than 2700K under laser Infrared irradiation within an extreme short time. Therefore, they proposed a hypothesis, comparing with the temperature rise by oven or hotplate heating, the materials cannot respond to expand with short time, herein there will be extreme reaction conditions inside the materials. This work has provided a good understanding of the laser-polymer interaction under extreme working conditions to synthesize porous Graphene. The researchers use the molecular dynamics simulation to study graphitization process of PI under high temperatures with high pressure or without high pressure. According to their study, there would create a high pressure of >3 GPa, if the volume cannot be changed with the rapid temperature rise under the canonical ensemble. And the crystallinity would be improved with the temperature rise. By contrast, for the isothermal -isobaric ensemble, there would not result in high pressure with the rapid localized temperature rise. In this case, the carbon element would exist like CO, HCN rather than carbon rings. Therefore, they concluded that the rapid extreme high temperature would suppress the decomposition of the polyimide and promote the carbon cluster bonding to form layered Graphene. This conclusion from molecular dynamics simulation is highly consistent with the Graphene formation under IR laser irradiation of previous studies. The study has given evidence of how the LIG formed under the photothermal effect by IR laser irradiation. Due to the cost-effectiveness of the equipment, the near-infrared laser such as 1064 nm is the most widely used laser source for laser scribing. However, because of the weak absorption for polymeric materials, the laser patterning on these kinds of substrates is difficult.

Up to now, several polymeric substrates have been studied as the carbon precursor to synthesize the LIG. The most used is Kapton, which is a Polyimide sheet with a relative high transmittance in the 10.6 μm and shows a high thermal stability of 350 ℃. Because there is varied thickness of Kapton sheets, it is useful for different devices design based on different applications. According to Ching-Ping Wong's study, the UV pulse laser of 355nm has been adopted to fabricate a smart pressure probe on the Kapton surface in different thickness [120]. Due to the good UV absorption of Kapton, strong focused spots would be obtained. They used the out-of-plane focus mode to achieve good carbonization of Polyimide and good adhesion of LIG on PI. By adjusting the parameters of power densities, pulse duration, and scanning speed, the minimum of line width of 50 μm has been obtained. In this study, the LIG formation under UV laser was discussed clearly. In 2019, Ching-Ping Wong's systemically studied the formation of LIG from Kapton under UV laser affect [121]. The LIG synthesis under UV laser is not a photothermal process, while the atomic bonds will be broken up directly due to the same level energy of the UV photons. That means the conversion process under UV laser irradiation is probably dominated by the photochemical effect. The high photon energy (~337 kJ/mol for 355 nm UV laser) would induce the direct photochemical deposition of the Polyimide rather than thermal expansion. At the same time, due to the optical limitations of UV laser, there will be easy peeling of the patterned structures, because of the large stresses between the formed LIG and polymeric substrate. Hence, there should always be careful about the adhesion issues of the patterned structures, especially for its application in electric devices. To address this problem, Florinda M. Costa's group made paper-LIG via 355 nm UV laser scribing for humidity and temperature detection [122]. By fixing the distance out of 5mm to the focus plane, the suspected carbonized material was obtained. Compared with the LIG foam made by infrared laser processing, the LIG structure is shallower to avoid adhesion failure. They also figured out there was an energy barrier to be overcome to be affected by the UV laser of the cellulose fiber of the paper. And once one or some spots has been overcome the energy barrier, the nearby area will be more easily transformed to conductive material, which was used to explain the triangular formation. At the same time, the energy barrier would result in triangular propagation, which would hinder the humongous geometry formation of the pattern. It has also been revealed that the fire-retardant treatment was necessary for LIG formation under UV laser processing. Moreover, some spectacular properties have been shown different from PI-LIG. Under UV laser, the Q-switching frequency is also an important parameter to figure out the crystal structure of the material. The obtained structure will be brittle when the Q-switching frequency is low. There will be no carbonized structure formed when the Q-switching frequency is high. The irradiation energy applied on the surface will be changed by adjusting the Q-switching frequency and scanning speed. Therefore, there should be a balance between the starting of carbonization transformation and the strength of structure. According to the SEM results, it can be found that the formation of UV laser induced fibrous Graphene from cellulose fiber follows the paths from pores form to pores grow, and then pores open.

Although it has been inferred that the ablation of polyimide under UV laser is dominated by photochemical effect, there are studies indicating that the photothermal effect may also exist in the LIG formation under different UV wavelength laser irradiation. In 1999, T.M. Yue's group investigated the ablation process of polyimide under UV laser irradiation by using the 355 nm NG: YAG laser machine [123]. According to their study, the obvious melting phenomenon has been observed, which means the photothermal effect may also contribute to the ablation of polyimide. H. Sohn's group investigated the ablation of polyimide under 355 nm UV laser irradiation from experimental and theoretical studies [124]. In this work, they concluded that there is no thermal deformation that occurred at low laser influence, while the photochemical effect is the dominate factor to contribute the ablation of Polyimide. To better interpret the mechanism of polyimide ablation under UV laser irradiation, Xiaoyan Zeng’s group adapted the single-mode pulse to avoid the extra interference [125]. It has been studied that the surface chemistry of PI with the air and the morphology would be different upon the different laser influence. When applied the 355 nm wavelength UV laser in picosecond mode, the concave structure was observed with no residual or recast layer due to the short pulse duration compared with the nanosecond mode, where it occurred both photochemical and photothermal effect. Herein, they revealed reason of different surface structures would be formed under the same wavelength UV laser irradiation. Overall, due to the localization of the photothermal effect, shorter wavelength of laser source would favor thinner sized substrate with higher resolution, more uniformity scribing and patterning.

2.3.3 Functionalization of laser induced graphene

Laser direct writing, which uses portable carbon precursors to induce the formation of porous structured graphene (LIG), has exhibited immense potential across various domains, including supercapacitors, electrocatalysis, photothermal sterilization, and wearable devices [126-130]. While porous structured graphene (LIG) shows remarkable surface structure, thermal properties, and electrical characteristics, its main drawback lies in its limited robustness on the substrate and challenges associated with transferring LIG films. These limitations have significantly hindered the broader applications of LIG in various fields. To address these challenges, efforts have been made to increase the thickness of LIG layers by changing the carbon precursor. Furthermore, in the realm of chemical and biosensing applications, enhancing the sensitivity and selectivity of LIG through functionalization is crucial. Similarly, in energy conversion and storage applications, functionalization becomes essential as LIG inherently shows low catalytic performance. Therefore, the functionalization of LIG plays a vital role in addressing these limitations. The functionalization of LIG can be categorized into two approaches: pre-treatment and post-treatment. Electrochemical deposition has been reported as a post-treatment method for modifying LIG. The distinctive three-dimensional porous microarchitecture of LIG offers a greater surface area compared to conventional current collectors. This leads to enhanced deposition and dispersion of functional materials on the surface. James' group successfully fabricated LIG hybrids of LIG–MnO2, LIG–FeOOH, and LIG–PANI, and used them as the Micro-supercapacitors [131]. Through the combination of direct laser writing and next electrodeposition in a two-step process (as shown in Figure 2.9), three conductive materials were successfully incorporated onto the LIG. This integration resulted in a significant enhancement of the electrochemical performance of the LIG composites, showing exceptional capabilities as a micro-supercapacitor.

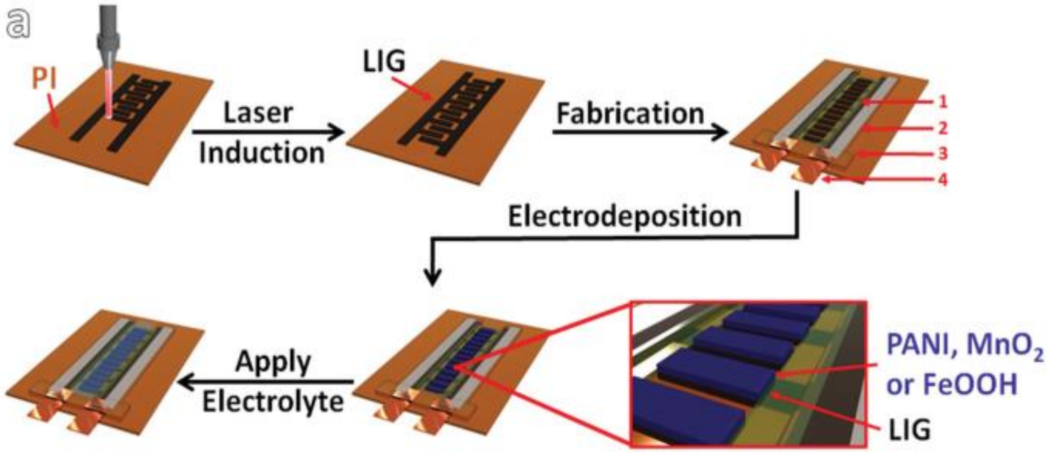

Figure 2.9 Scheme of the fabrication of MSCs with LIG–MnO2[131]

Zhao's group has developed a simple and efficient approach using a similar method to fabricate a flexible composite electrode composed of Cu nanoparticles (Cu NPs) and LIG. This electrode has been successfully worked as a non-enzymatic sensor for accurate determination of glucose levels [132]. The fabrication process is shown in Figure 2.10, where the incorporation of Cu NPs significantly enhances the electron transfer between the flexible porous graphene matrix and Cu. Consequently, this leads to the creation of an innovative non-enzymatic glucose biosensor. The biosensor shows remarkable features including exceptional sensitivity, high stability, good reproducibility, excellent selectivity, a remarkable detection limit, and rapid response to aerometric measurements. Moreover, through the electrodeposition technique, various functional materials such as individual metallic nanoparticles, metallic alloys, and metallic oxides can be immobilized onto the LIG.

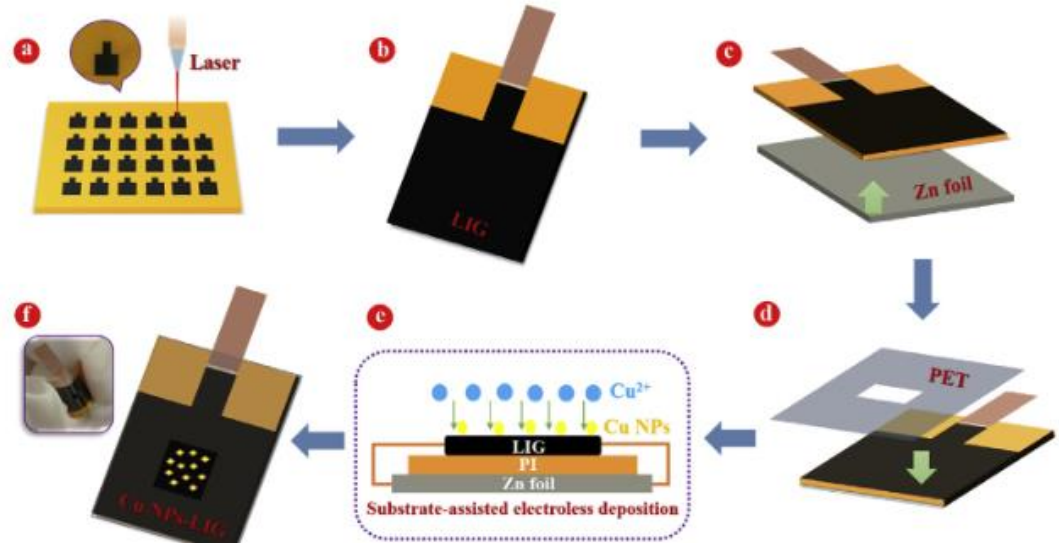

Figure 2.10 Fabrication process of the flexible Cu NPs-LIG sensor [132]

In situ synthesis has been reported as an alternative approach to functionalize laser-induced graphene. In this approach, the first step involves applying or coating a thin layer of a doped material onto a PI substrate. After drying and undergoing laser scanning, a layer of the doped material is formed on the surface of the laser-induced graphene, resulting in the creation of a hybrid material. However, it is important to consider that doped materials susceptible to volatilization or decomposition under light and heat are not suitable for this method. Furthermore, this technique has the drawback of potentially increased aggregation of the doping material on the surface of laser-induced graphene (LIG), which can hinder dispersion and limit the performance of LIG. Zhang used a one-step laser writing process to create efficient water-splitting electrodes based on hybrids of laser-induced graphene (LIG) and Pt nanoparticles (Pt NPs) [133]. The process of fabricating catalytic laser-induced graphene (LIG) electrodes on cost-effective PI films is illustrated in Figure 2.11. In this study, the electrodes were loaded with catalysts through electrochemical deposition. The resulting LIG electrodes, specifically LIG-Pt, LIG-NiFe, and LIG-Co-P, showed exceptional activity surpassing state-of-the-art catalysts for both the hydrogen evolution reaction (HER) and the oxygen evolution reaction (OER) under alkaline conditions.

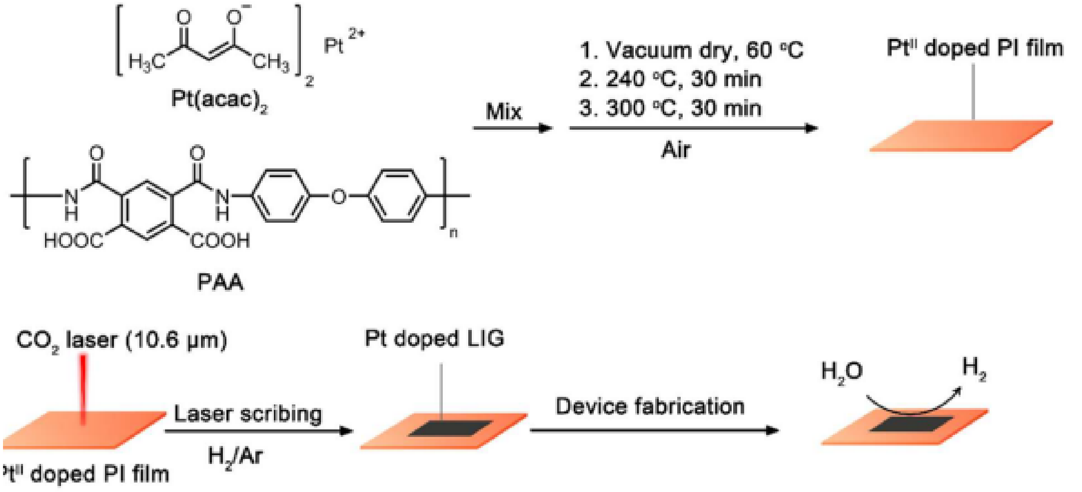

Figure 2.11 Fabrication process of the LIG-Pt [133]

Laser-induced graphene (LIG) has shown its scalability as a fabrication method for producing 3D porous graphene in manufacturing, surpassing conventional methods. A wide range of organic materials, including polyimide, polyester, Bakelite, and certain natural organic materials, can serve as carbon sources for LIG production [127]. An additional significant aspect of LIG is its ability to achieve varied surface wettability levels by adjusting the conditions of the laser process [126, 129]. Several research studies have reported the development of hybrid laser-induced graphene (LIG) materials incorporating metals or metal oxides [134-136]. However, earlier investigations have involved complex processing methods and the use of expensive equipment to mix metal or metal precursors with a carbon source prior to laser ablation or reaction. For example, the metal or metal precursors were either dispersed on the surface of a carbon source film or mixed with a carbon source solution, which was then cast as a film for laser treatment. Subsequently, the graphene metal/metal oxides nanocomposites were grown on the precursor film or synthesized in the solution through laser ablation. Recently, two reported methods for functionalizing LIG include in situ synthesis pretreatment and electrochemical deposition aftertreatment. However, most of the research on LIG has primarily focused on its application as an electrode, as the LIG remains confined to the substrate surface. Therefore, further optimization of laser treatment parameters or combination with other deposition methods is still necessary to fully realize the functionalization of LIG. Moreover, there have been limited investigations into the performance and application of nanomaterials based on LIG for renewable energy conversions.

2.4 Research problems and methodology

Based on literature studies, carbon nanomaterials have shown tremendous potential in the application for addressing environmental and energy issues. However, there are still numerous challenges and issues associated with their practical application. One of the challenges to scale up the application of carbon-based nanocomposites is its excessive cost and complex process methods. Meanwhile, the construction of 3D carbon nanomaterials holds significant potential for enhancing renewable energy harness, but further development is still needed. What is more, the research on functionalization strategies serves as a crucial means to broaden the applications of carbon nanomaterials. Herein, the pursuit of simple and effective fabrication and functionalization strategies for novel and reliable carbon nanomaterials is necessary in expanding their applications in energy and environmental fields. To explore novel carbon nanocomposites for emerging renewable energy applications, the research flowchart is represented in Figure 2.12.

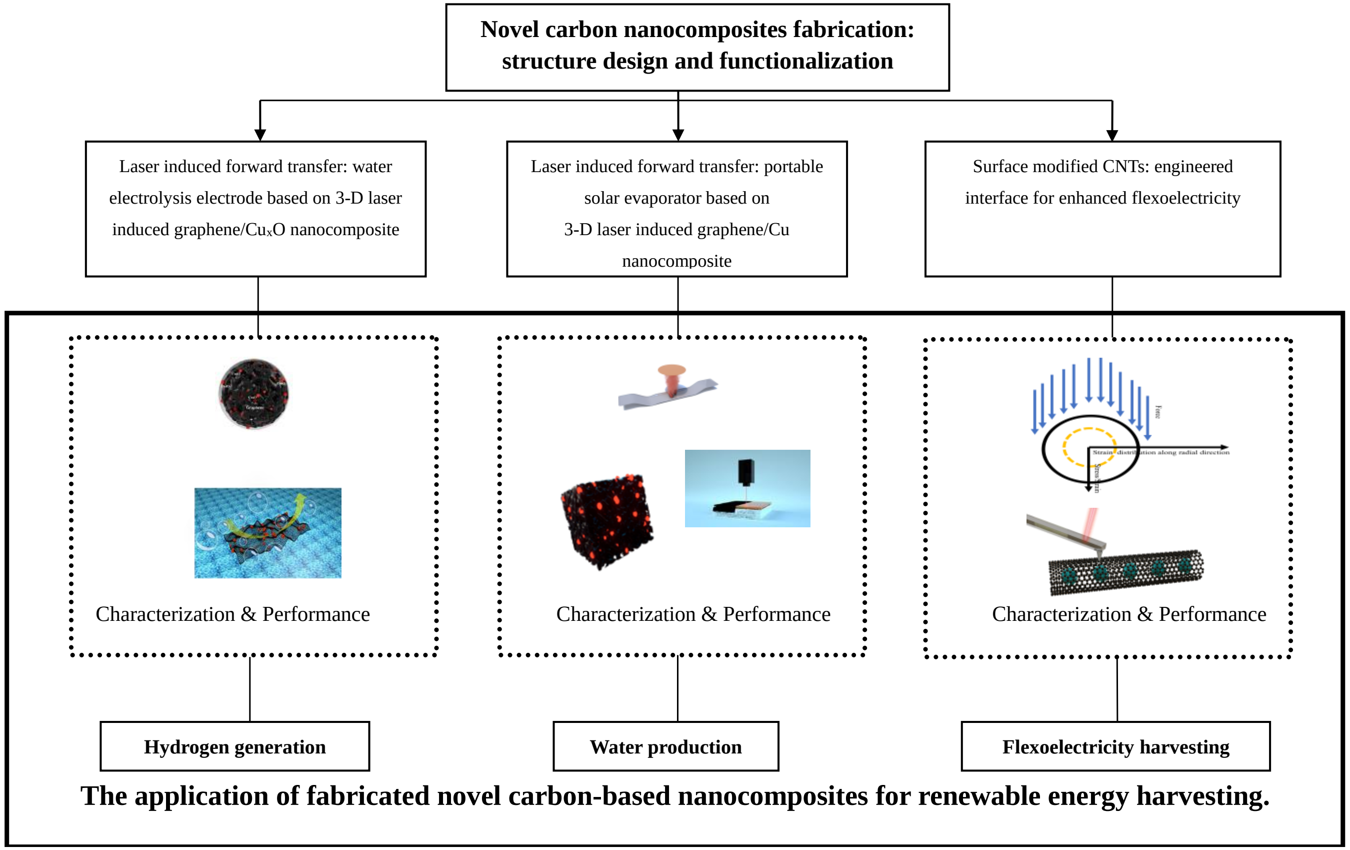

Figure 2.12 Research flowchart of the thesis

Chapter 3

One-step fabrication of laser induced forward transfer graphene/Cu_xO nanocomposite-based electrode to promote hydrogen evolution reaction activity

Based on the previous literature study, the adoption of advanced preparation strategy holds significant importance in broadening the utilization of renewable energy. Therefore, this chapter employs a laser-induced forward transfer method to fabricate laser-induced graphene composites in a single step, aiming to explore the feasibility of their application in hydrogen production through water electrolysis.

3.1 Introduction

In recent years, there has been a growing concern about the worsening energy shortage and environmental pressures. As a result, the focus has shifted towards exploring and applying effective clean energy solutions as the primary strategy to gradually replace fossil fuels in academic and industrial sectors. Molecular hydrogen, as a renewable fuel, holds significant promise in addressing air pollution issues by substituting a part of the depleting fossil fuel consumption. Furthermore, its high energy density and eco-friendliness make it a highly workable option for maintaining adequate energy consumption in industrial sectors and the energy grid [137-140].

Industrial hydrogen production primarily involves coal conversion, natural gas steam reforming, methanol or ammonia decomposition, and water electrolysis. Among these processes, water electrolysis has witnessed significant advancements in recent decades, primarily attributed to its advantages of abundant water availability and the production of high-purity energy. In general, the electrochemical process of water splitting consists of two half-reactions: the hydrogen evolution reaction (HER) and the oxygen evolution reaction (OER) [141]. Water electrolysis can take place in different electrolyte environments, including acidic, neutral, and alkaline media. Among these, alkaline water electrolysis has garnered significant interest and widespread application in industries due to its high stability and lower environmental requirements. Nevertheless, alkaline water splitting requires higher energy input compared to acid and neutral water electrolysis due to sluggish kinetics. Therefore, the development of efficient electrocatalysts with low energy barriers in alkaline water splitting is crucial for achieving large-scale hydrogen production and enabling its widespread application. In earlier research, precious metals such as platinum (Pt) and Pt-based materials have shown excellent performance in alkaline hydrogen evolution reaction (HER) due to their low energy barrier during the Volmer step, which facilitates the adsorption of hydrogen in the intermediate reaction process. These materials have been extensively studied for their potential in alkaline water splitting [142, 143]. Nevertheless, the high cost, limited durability, and scarcity of precious metals have hindered their further development as electrocatalysts. Consequently, significant efforts have been directed towards the development of nonprecious electrocatalysts with high catalytic activity for alkaline hydrogen evolution reaction (HER). In this regard, multicomponent alloys have appeared as promising candidates for water splitting due to their abundance in Earth's crust, low-cost fabrication, excellent cooperativity, durability, and catalytic activity. Transition metal compounds (TMX, where X represents elements such as O, S, C, or N, among others) have garnered significant attention from researchers due to their remarkable electrocatalytic activity and durability. The exploration of these compounds has become a focal point in the pursuit of efficient and sustainable electrocatalysts. Extensive research has been conducted on electrochemical water splitting using affordable transition metal compounds supported by nanostructures. This approach has been recognized as a practical solution to enhance catalytic efficiency by providing a substantial number of exposed surface-active sites and facilitating high electron transfer rates. Such investigations aim to improve the overall performance and cost-effectiveness of water splitting processes for sustainable hydrogen production [144-146]. Copper, known for its cost-effectiveness and abundant availability, has garnered significant attention in the field of electrocatalysis due to its excellent electrical performance. Notably, copper oxide (CuO) and copper(I) oxide (Cu_2O) exhibit p-type semiconductor properties and have been used as photocatalysts for water splitting. In a study by Krishnamurthy et al., Cu_2O/CuO heterojunction catalysts for water splitting were successfully developed using the atmospheric pressure plasma method [147]. Ismail et al. have made significant advancements in solar water splitting by developing a highly efficient thin film of Cu_xO through the reduction of a CuI film. The innovative approach has shown promising results in enhancing the efficiency of solar-driven water splitting processes [148]. Moreover, the nanostructured morphology of Cu-based electrodes has been extensively studied for water splitting applications. Kong et al. have successfully fabricated Cu-based nanosheets through an electrochemical process, and their research focused on investigating the hydrogen evolution reaction (HER) and oxygen evolution reaction (OER) activities of this material. The study offers valuable insights into the electrocatalytic performance of Cu-based nanosheets in water splitting processes [149]. Earlier studies have highlighted the remarkable performance of Cu-based catalysts for water splitting, but their conventional synthesis typically involves high-temperature processing or high-pressure conditions, often requiring additional gas supplementation over extended periods of time.

Two-dimensional structured nanomaterials, such as graphene, black phosphorus [13, 150] and C_3N_4[151-153] and other hybrid structures have received markable HER capabilities [154-156]. Laser-induced graphene (LIG) has appeared as a scalable manufacturing technique for producing three-dimensional porous graphene structures. Various organic materials, including polyimide, polyester, Bakelite, and certain natural organic materials, can be used as carbon sources to generate LIG. This versatility in carbon sources expands the possibilities to produce LIG and its applications in diverse fields [127]. An additional notable aspect of laser-induced graphene (LIG) is its ability to achieve different surface wettability levels by adjusting the laser processing conditions. This capability allows for the control and manipulation of surface properties, opening possibilities for applications where specific surface wettability characteristics are desired [126, 129]. Metal or metal oxides hybrid LIG has been reported by some research [134-136]. Nevertheless, earlier investigations have often involved complex process methods and the use of expensive equipment to mix metal or metal precursors with graphene sources prior to laser ablation or reaction. Typically, the metal or metal precursors would be dispersed onto the surface of a carbon source film or mixed with a carbon source solution, followed by casting the mixture as a film for later laser treatment. Finally, the graphene@ metal/metal oxides nanocomposites would be grown on the precursor film or synthesized in the solution by laser ablation. Herein, we prove a composite with ultrasmall sized Cu_xO nanoparticles combined porous laser induced forward transfer (LIFT) graphene directly deposition on Ni foam by a single one-step laser transfer process based on the earlier research [157, 158]. In this study, the precursor of CuxO nanoparticles, $CuCl_2$, was initially dissolved in ethyl alcohol and subsequently spin-coated onto the surface of a commercially available polyimide (PI) film. Following the optimization of laser conditions, Cu_xO nanoparticles encapsulated with graphene were successfully immobilized uniformly onto the surface of nickel foam. Remarkably, this composite showed impressive electrocatalytic activity for the hydrogen evolution reaction (HER) in a 1M KOH solution. The overpotential is only 149.6 mV at the current density of 10mA cm^{-2}, and the Tafel slope is 157 mV dec^{-1}. It also displays a desired durability in a 10 hours chronoamperometry test. The experimental results indicate that this synthesized composite exhibits promising potential for applications in alkaline water splitting. Drawing inspiration from this rapid and straightforward method, porous graphene supported with various metal oxides or hybrid materials can be tailored as a cost-effective catalyst substrate for efficient and scalable electrochemical hydrogen production. This approach holds great promise for advancing the field of sustainable hydrogen generation.

3.2 Experimental section

3.2.1 Fabrication of the functional composites based on Ni foam.

$CuCl_2$, obtained from Aladdin Chemistry Company, was dissolved in ethyl alcohol (AR grade, Aurora Chemical) using magnetic stirring and ultrasonic dispersion. The resulting solution was spin-coated onto the surface of a polyimide (PI) film (50 μm, Dupont). After drying in an oven, a uniform film consisting of $CuCl_2$ decorated with PI was formed. This PI-coated film was then affixed to the surface of a nickel foam. The assembly was positioned on the working stage of an M-SOLV MSV-200W laser machining system (Figure 3.1), operating in pulse mode scribing. The laser system had a wavelength of 1070 nm, an output power of 25 W, a scan rate of 48 mm/s, a pulse width of 2.5 ms, and a spot size of 500 μm. The laser beam was focused slightly below the film surface, keeping a downward distance of 5 mm. Upon laser treatment, layers of graphene integrated with CuxO nanoparticles were formed on the reverse side of the PI film and subsequently transferred onto the surface of the nickel foam in a single step.

3.2.2 Instruments and characterization

Figure 3.1 M-SOLV MSV-200W laser machining system

Figure 3.2 JEOL model JEM-2100F STEM

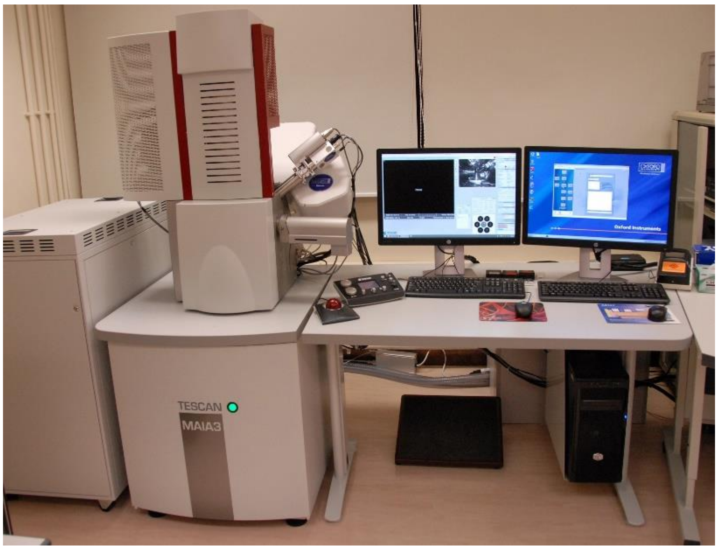

Figure 3.3 TESCAN MAIA 3 field-emission scanning electron microscopies (FESEM)

Figure 3.4 TESCAN VEGA 3 scanning electron microscopies (SEM)

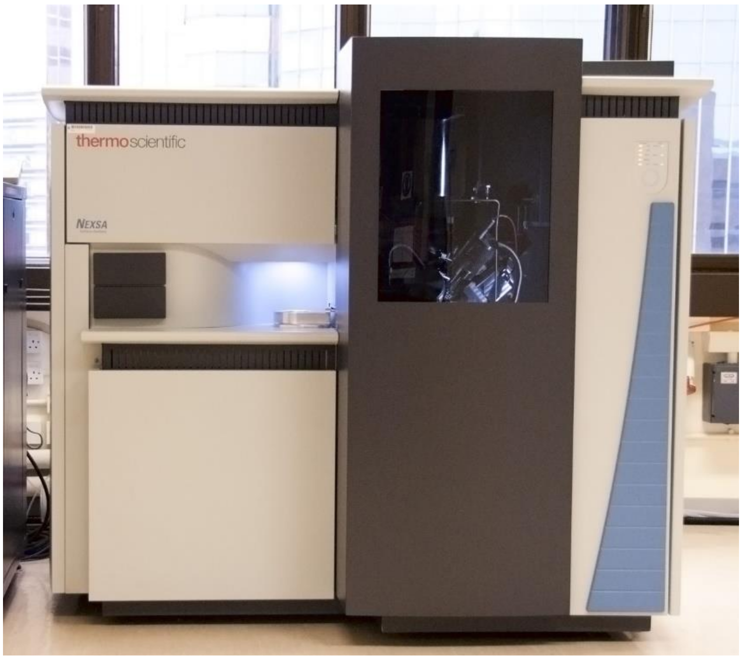

Figure 3.5 Thermo Scientific Neasa surface analysis system

Figure 3.6 Rigaku SmartLab system

Figure 3.7 CHI660E Electrochemical Analyzer

The morphology of the nanocomposites was analyzed using JEOL model JEM-2100F scanning transmission electron microscopy (STEM) (Figure 3.2) and TESCAN MAIA 3 field-emission scanning electron microscopy (FESEM) (Figure 3.3) equipped with an energy-dispersive X-ray spectroscopy (EDX) detector. The surface appearance of the electrodes was seen using TESCAN VEGA 3 scanning electron microscopy (SEM) (Figure 3.4). Raman spectra were acquired using a Renishaw Micro-Raman Spectroscopy System with a 532 nm laser source. XPS data was obtained using a Thermo Scientific Nexsa surface analysis system (Figure 3.5). XRD pattern of the as-fabricated composites was collected by Rigaku SmartLab system (Figure 3.6) using a rotating anode X-ray source (λ~1.54 Å). Electrochemical tests, including CV, LSV, EIS, ECSA and Tafel analysis, were conducted on a CHI660E Electrochemical Analyzer (Figure 3.7) by a standard three-electrode system [159]. The hydrogen evolution reaction (HER) activity was evaluated in a 1M KOH (AR grade, Aurora Chemical) electrolyte solution. A graphite rod and a mercuric oxide electrode (as depicted in Figure 3.15) were employed as the counter and reference electrodes, respectively, both obtained from Tianjin Aida Technology Company.

3.3 Results and discussion

In this study, a LIFT (Laser-Induced Forward Transfer) graphene/Cu_xO-based electrode was fabricated using a simple and rapid one-step method known as direct laser deposition. The detailed preparation process of the nano-composite electrode is illustrated in Figure 3.8. Initially, the copper (Cu) precursor was spin-coated onto the surface of a polyimide (PI) film. Subsequently, the PI film, coated with $CuCl_2$, was positioned above the surface of a nickel (Ni) foam. The powerful laser beam applied during the process resulted in simultaneous heating of the PI film and $CuCl_2$. This led to the formation of Cu_xO nanoparticles, which were subsequently enveloped by graphene during the laser treatment. After optimizing the laser conditions, the composite was transferred onto the surface of the Ni foam. Finally, the LIFT graphene/Cu_xO @Ni foam electrode was obtained. Scanning electron microscope (SEM) images of the LIFT graphene/Cu_xO @Ni foam electrode are presented in Figure 3.9, demonstrating the overall morphology of the porous structured materials integrated within the Ni foam substrate.

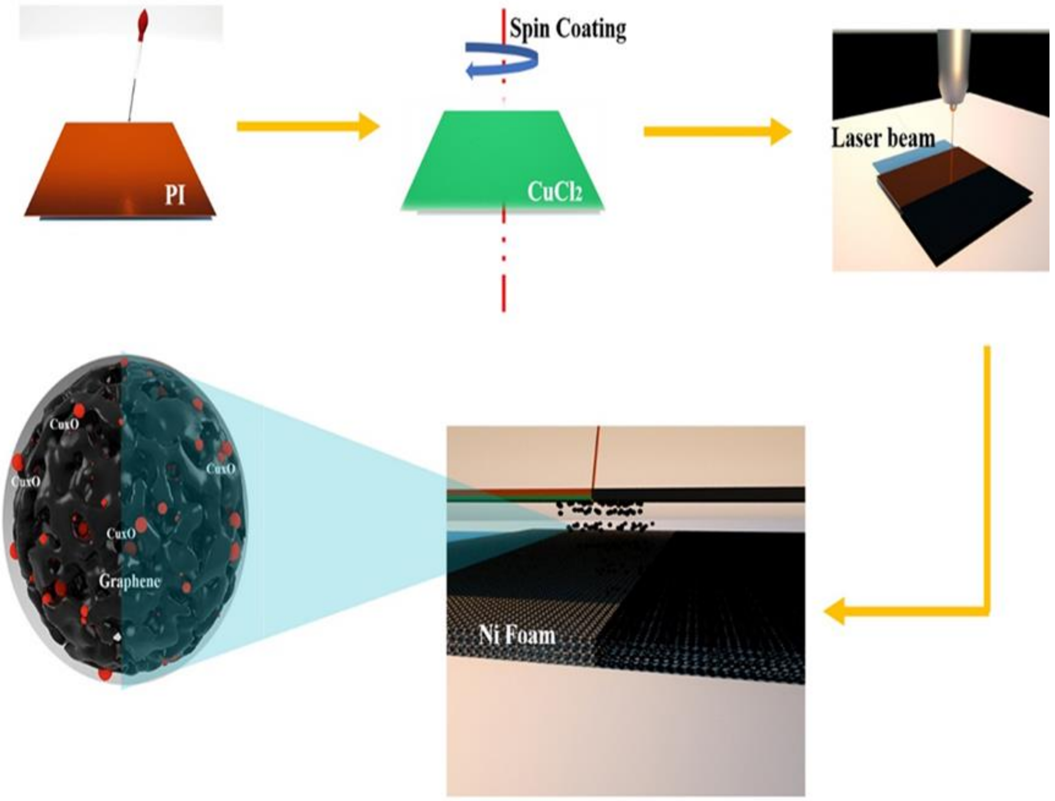

Figure 3.8 The flow chart of the LIFT graphene/Cu$_x$O based electrode fabrication.

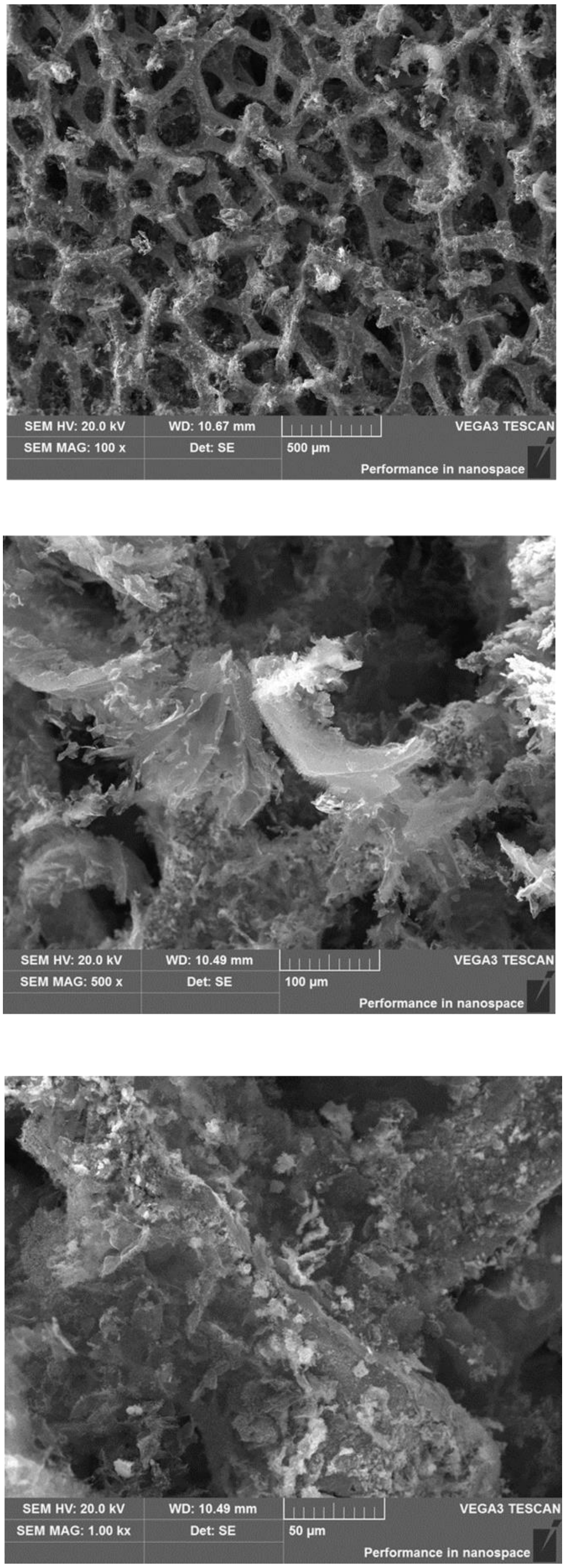

Figure 3.9 SEM images of the LIFT graphene/Cu_xO @Ni foam

Figure 3.10 displays transmission electron microscopy (TEM) images that clearly reveal the presence of nanoscale Cu_xO particles encapsulated by graphene, with the nanoparticles showing a minimum size below 5 nm. Correspondingly, Figure3.11 presents field emission scanning electron microscopy (FESEM) images, demonstrating similar observations of porous graphene tightly enveloping the nanoparticles. Furthermore, Figure 3.12 illustrates the Energy Dispersive X-ray (EDX) mapping, which provides further evidence of the uniform dispersion of copper (Cu) elements within the porous graphene structure.

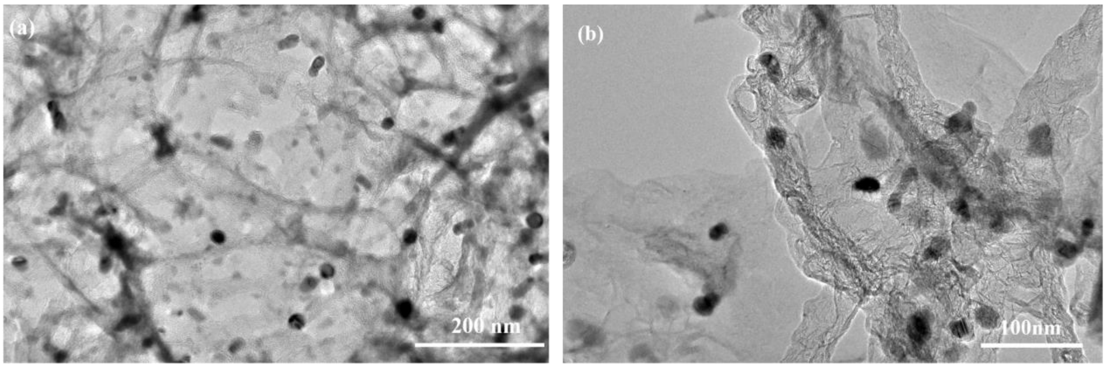

Figure 3.10 (a) TEM image of the LIFT graphene/Cu_xO, (b) The magnified image of the LIFT graphene/Cu_xO.

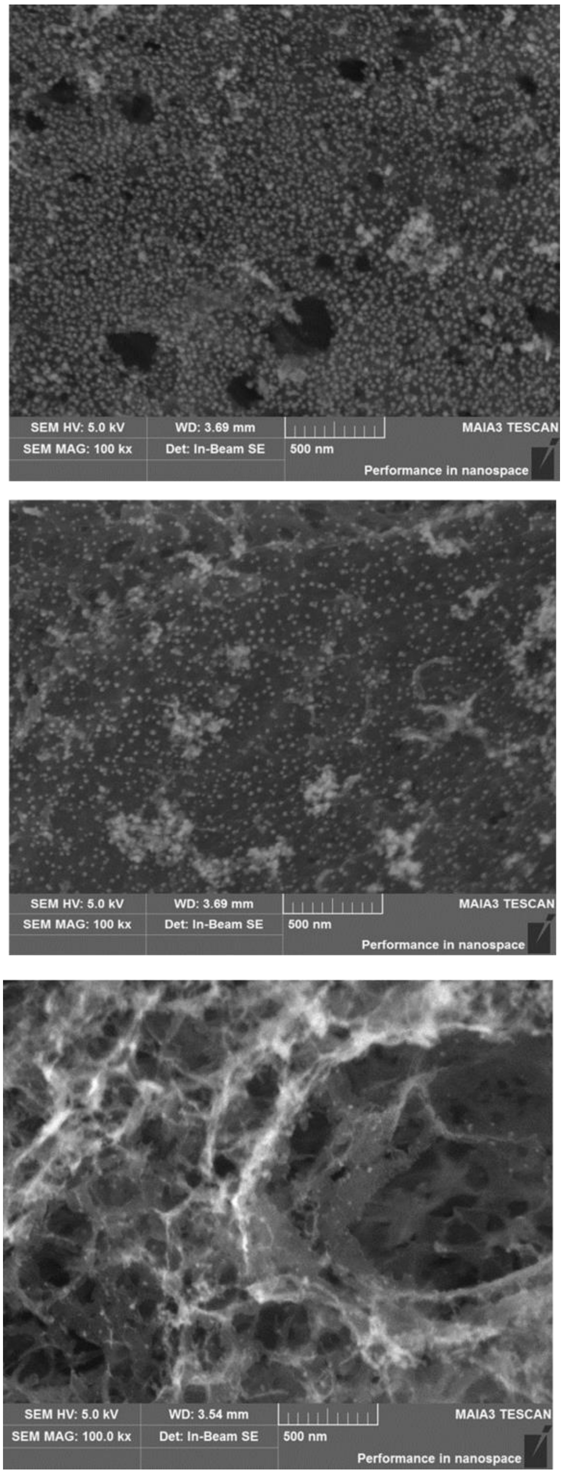

Figure 3.11 FESEM images of porous graphene tightly enveloping the nanoparticles

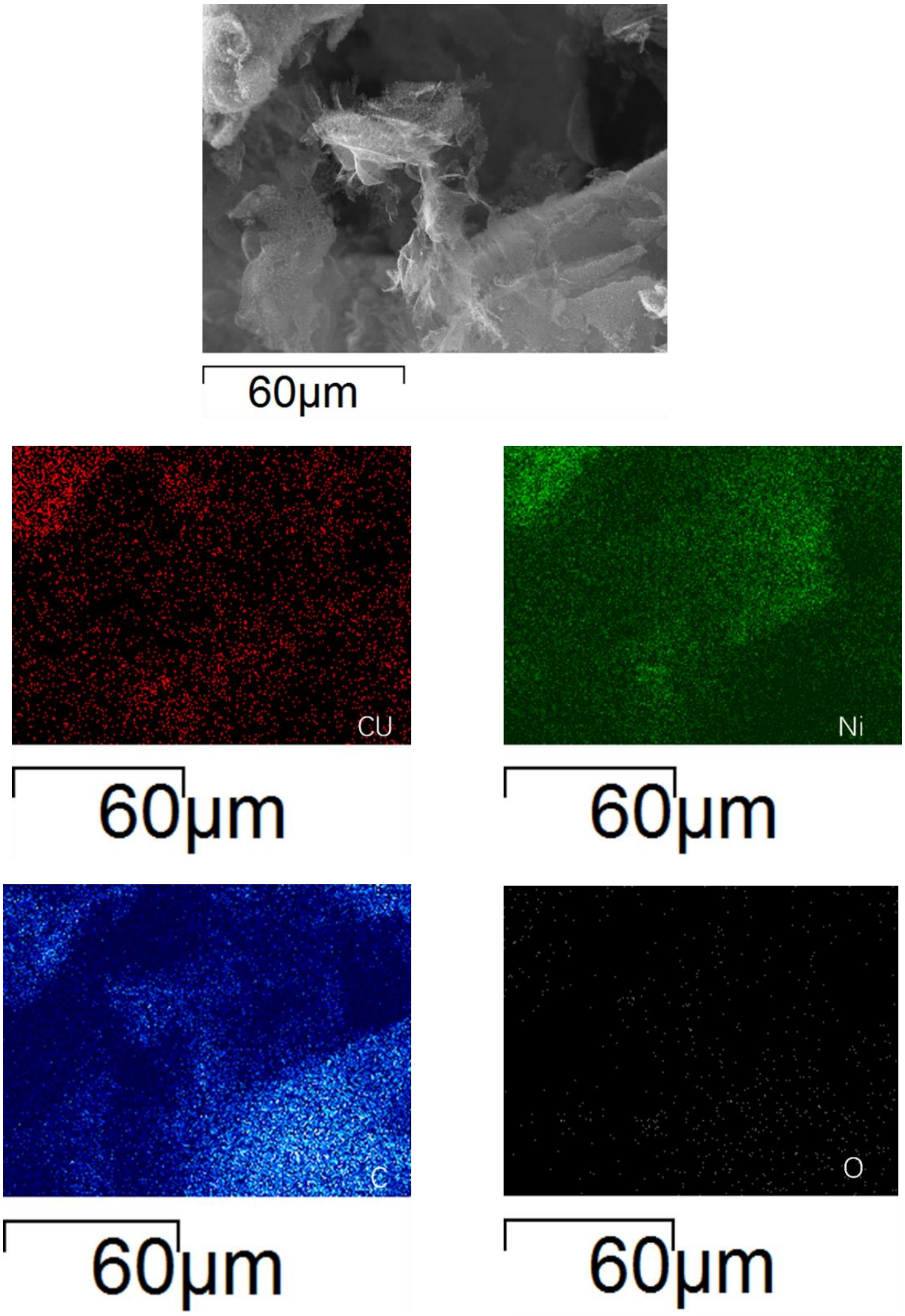

Figure 3.12 Energy Dispersive X-ray (EDX) mapping of LIFT graphene/Cu$_x$O @Ni foam

To identify the materials in the nanocomposite, Raman spectra analysis was conducted in this work, as shown in Figure 3.13 (a). The corresponding Raman peaks are located at 1330 cm^{-1}, 1570 cm^{-1}, 2665 cm^{-1} and 2898 cm^{-1}, which can be clearly assigned to the graphene D, G, 2D and D+G phonon modes, respectively, which is consistent with the results of LIFT graphene in previous study [115, 160-162]. The intensity ratio of the D peak to the G peak in LIFT graphene is measured to be 0.87, which is nearly identical to the ID/IG ratio observed in LIFT graphene/CuxO. This suggests that the incorporation of CuxO nanoparticles does not significantly affect the formation of LIFT graphene. To examine the graphene-based nanocomposite in more detail, X-ray diffraction (XRD) analysis was conducted, as presented in Figure 3.13 (b). The XRD pattern clearly shows the presence of various cupric forms within the nanoparticles of this composite. The dominant diffraction peaks observed at 43.3º, 50.4º, and 74.2º correspond to the (111), (200), and (220) crystal planes of metallic copper (Cu) (PDF#04-0836), indicating that the majority of the $CuCl_2$ precursors were reduced to metallic Cu particles under the high temperature generated by the laser beam. The weaker peaks detected at 37º, 42.6º, 62.4º, and 74.4º are attributed to the (110), (200), (220), and (311) planes of cuprous oxide (Cu2O) (PDF#34-1354). These peaks suggest the presence of some Cu^{2+} ions from the CuCl2 precursor that were reduced to Cu^{+} ions. Furthermore, additional weaker peaks observed at 45º, 47.6º, 50º, 56.4º, 61.3º, and 62.3º can be assigned to the crystal planes of Cu_2Cl (OH)3, indicating the presence of unreacted Cu^{2+} ions from the $CuCl_2$ precursor. From the results of XRD, it can be seen that CuCl2 is laser-reduced to copper compounds.

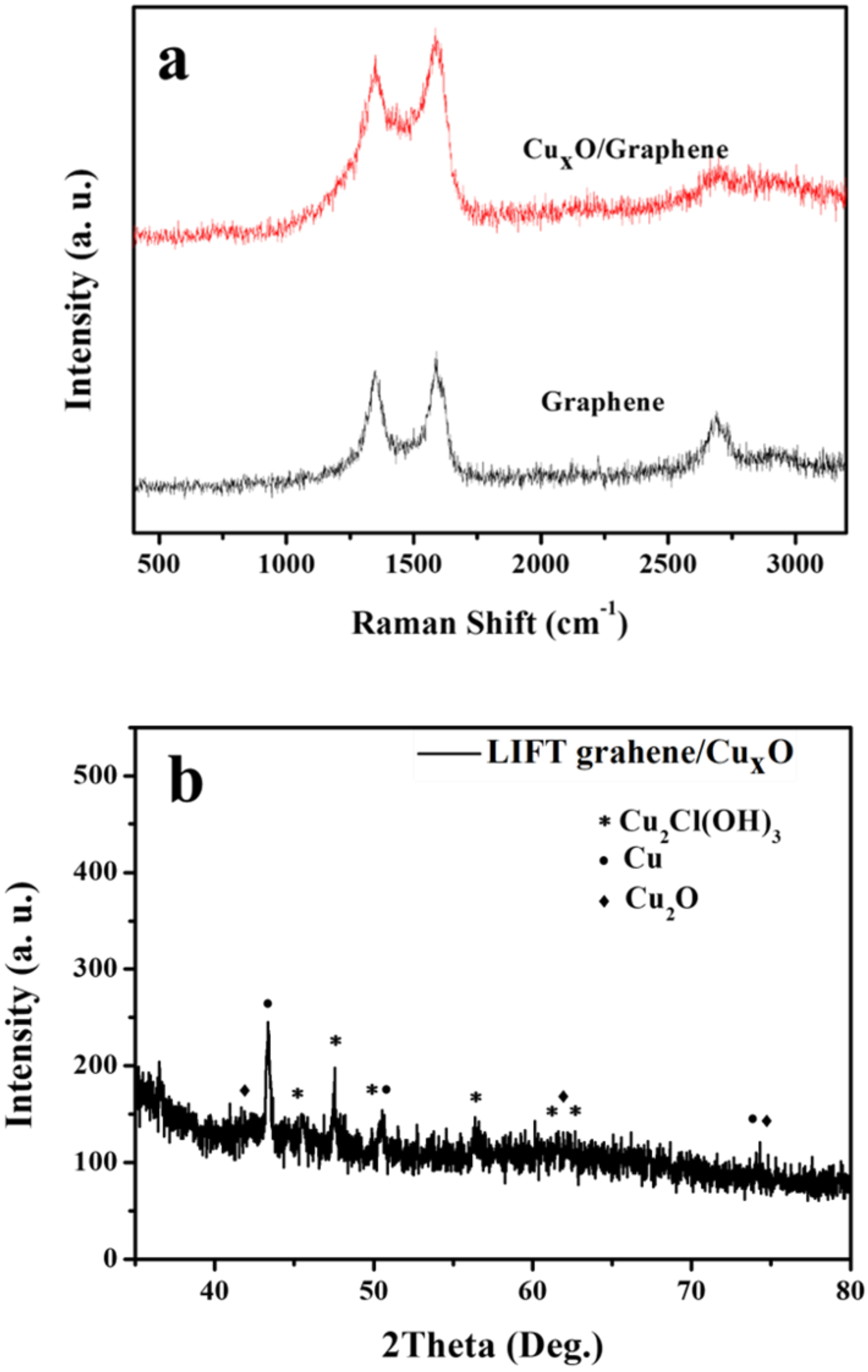

Figure 3.13 (a) Raman spectra of LIFT graphene/Cu$_x$O and Pure LITF graphene, (b) XRD result of LIFT graphene/Cu$_x$O

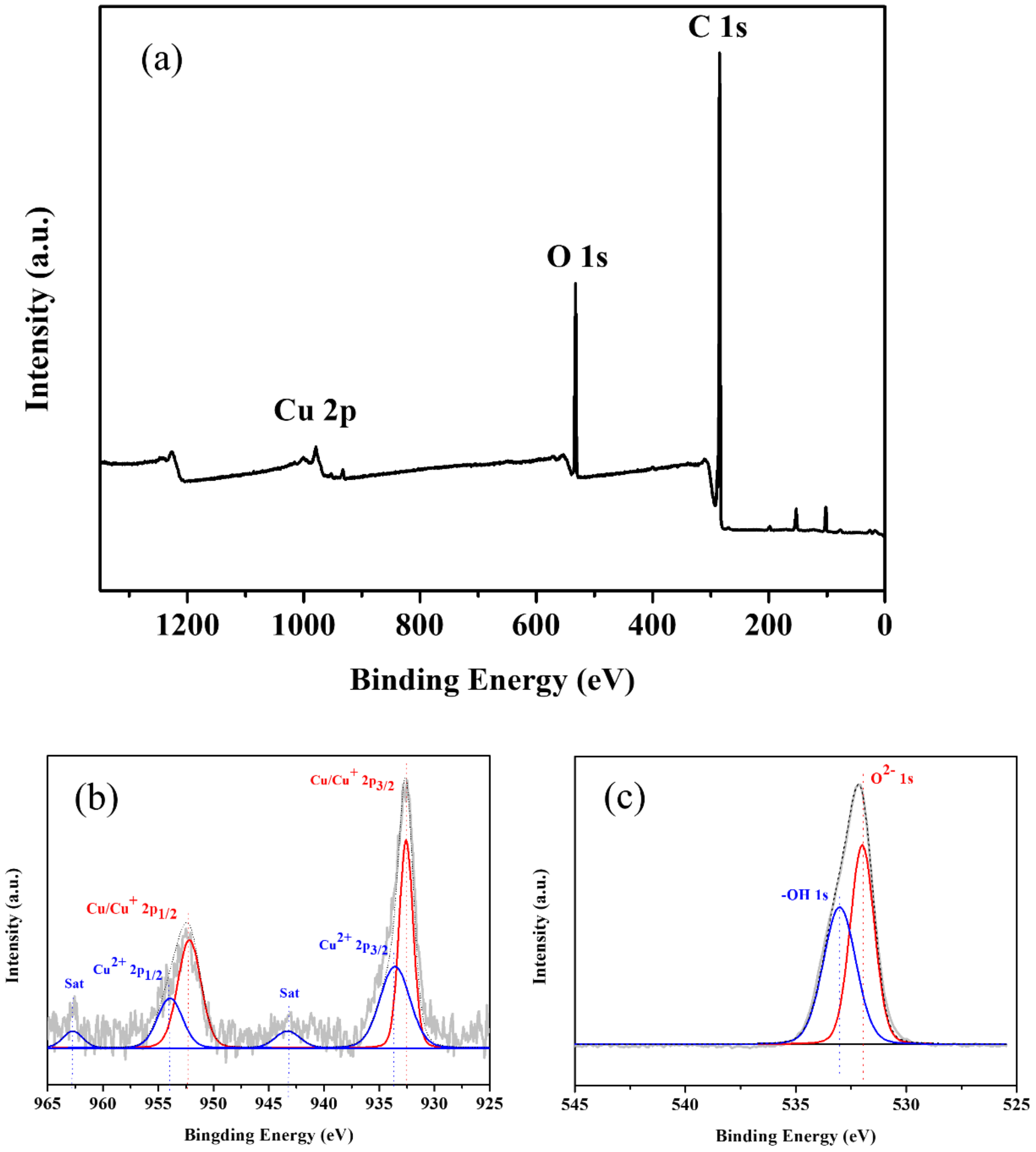

Figure 3.14 (a) XPS survey spectra of LIFT graphene/Cu$_x$O, (b) High resolution Cu$_2$p spectra of LIFT graphene/Cu$_x$O, (c) High resolution O1s spectra of LIFT graphene/Cu$_x$O

X-ray photoelectron spectroscopy (XPS) was employed to analyze the chemical composition of the LIFT graphene/Cu$_x$O composites, as depicted in Figure 3.14. The survey spectra confirm the presence of carbon (C), oxygen (O), and copper (Cu) on the surface of the nanocomposites. Notably, the C1s peak dominates the spectrum, indicating that graphene is the primary component of nanocomposites. High-resolution spectral analysis of the Cu 2p region, as shown in Figure 3.14 (b), reveals the presence of at least two distinct chemical states of copper within the nanocomposites. The main peaks observed at 932.5 eV and 952.2 eV correspond to both Cu and Cu+ states, consistent with previous literature [55, 56]. Additionally, two peaks at 933.9 eV and 953.94 eV can be assigned to Cu2+ 2p3/2 and Cu2+ 2p1/2, respectively, accompanied by two satellite peaks at 943.1 eV and 962.7 eV, indicating the presence of unreduced precursor species. In the high-resolution O 1s spectrum (Figure 4(c)), two prominent peaks at binding energies of 530.5 eV and 533.1 eV are observed, corresponding to O2- 1s and -OH 1s, respectively. Thus, the XPS analysis is consistent with the XRD results, suggesting that the nanocomposites consist of graphene, Cu, Cu2O, and a small number of unreduced precursors.

The as-fabricated LIFT graphene/CuxO @Ni foam serves as the work electrode (Figure 3.15) for evaluating the electrocatalytic performance of the hydrogen evolution reaction (HER). Three different samples were investigated: LIFT graphene/CuxO @Ni foam, LIFT graphene @Ni foam, and bare Ni foam. The electrochemical measurements were conducted in an alkaline medium (1 M KOH) at room temperature. Figure 3.16(a) shows the linear sweep voltammetry (LSV) curves of the three catalysts at a scan rate of 5 mV/s, covering a potential range from 0 to -0.4 V vs RHE. Figure 3.16 (b) summarizes the overpotential of the three catalysts at a current density of 10 mA/ cm^2. The bare Ni foam exhibits an overpotential higher than 300 mV, which is reduced to 273 mV when combined with LIFT graphene.

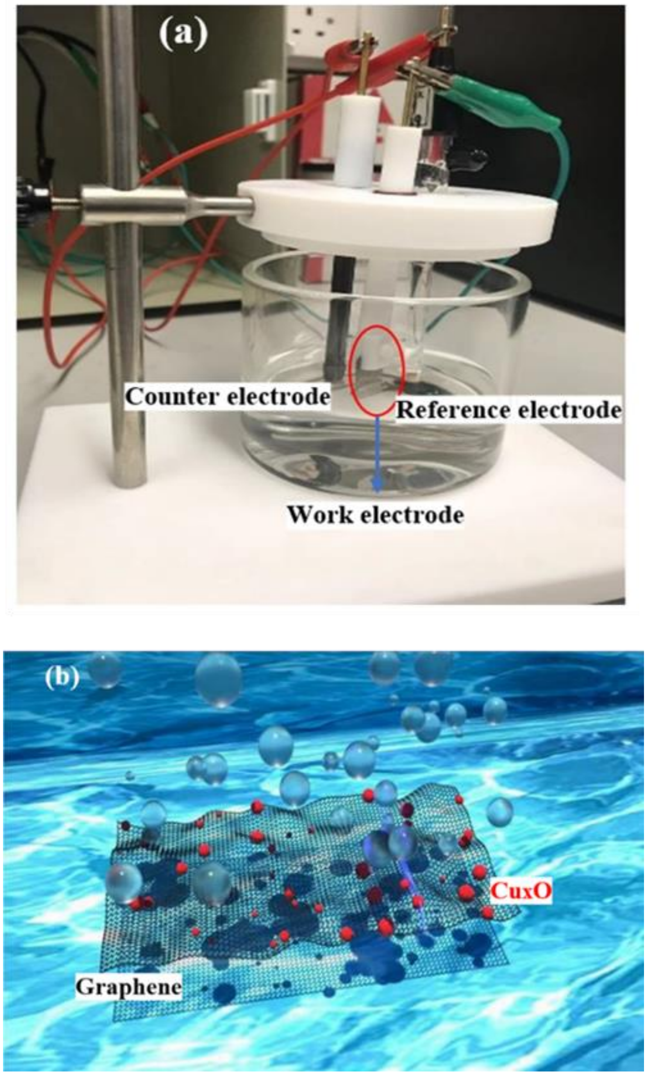

Figure 3.15 Experiment set-up of the three-electrode: (a) A graphite rod and a mercuric oxide electrode as the counter and reference electrode respectively, and (b) HER process in 1M KOH.

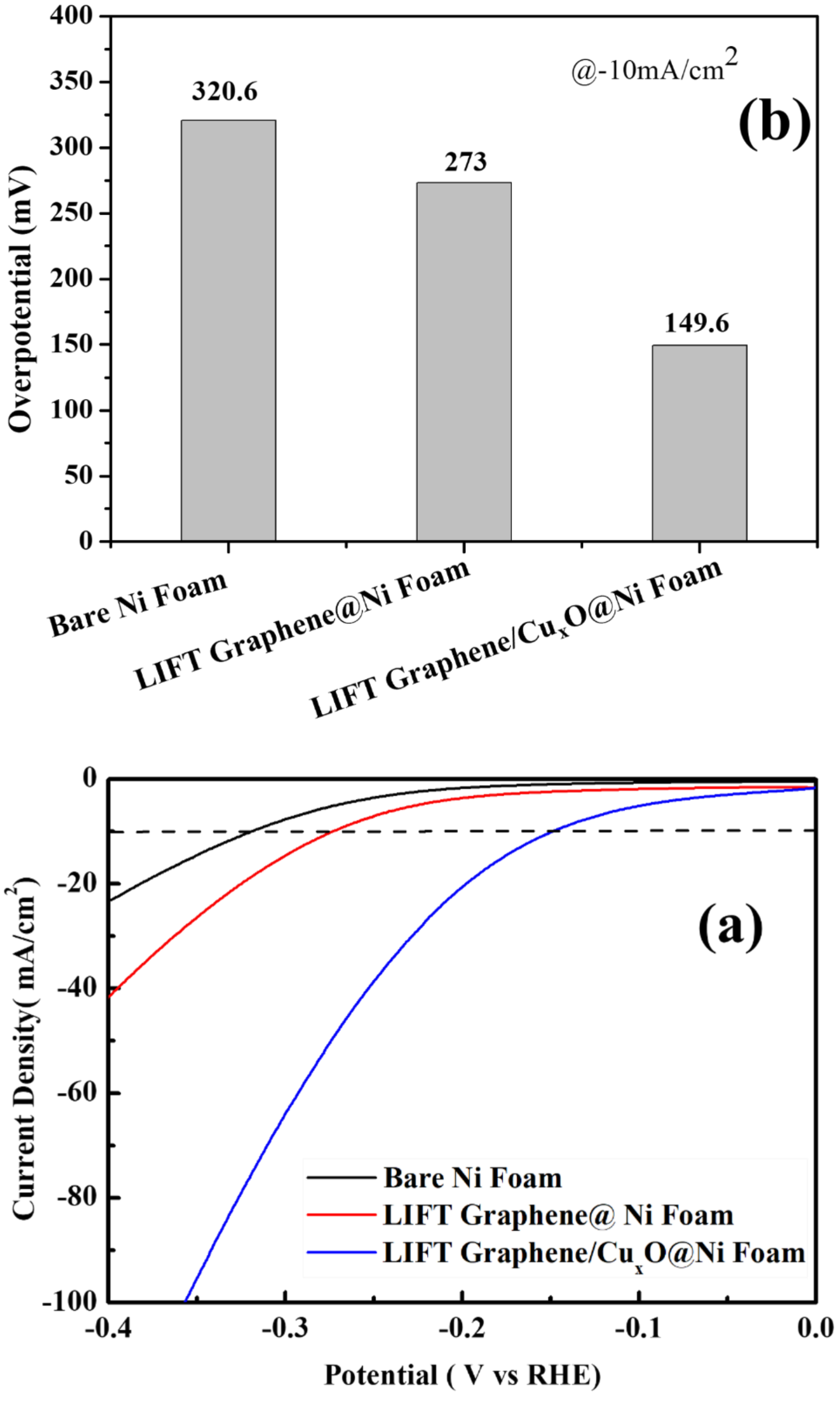

Figure 3.16 (a) LSV curves, (b) Overpotential values at a current density of 10 mA cm^{-2}

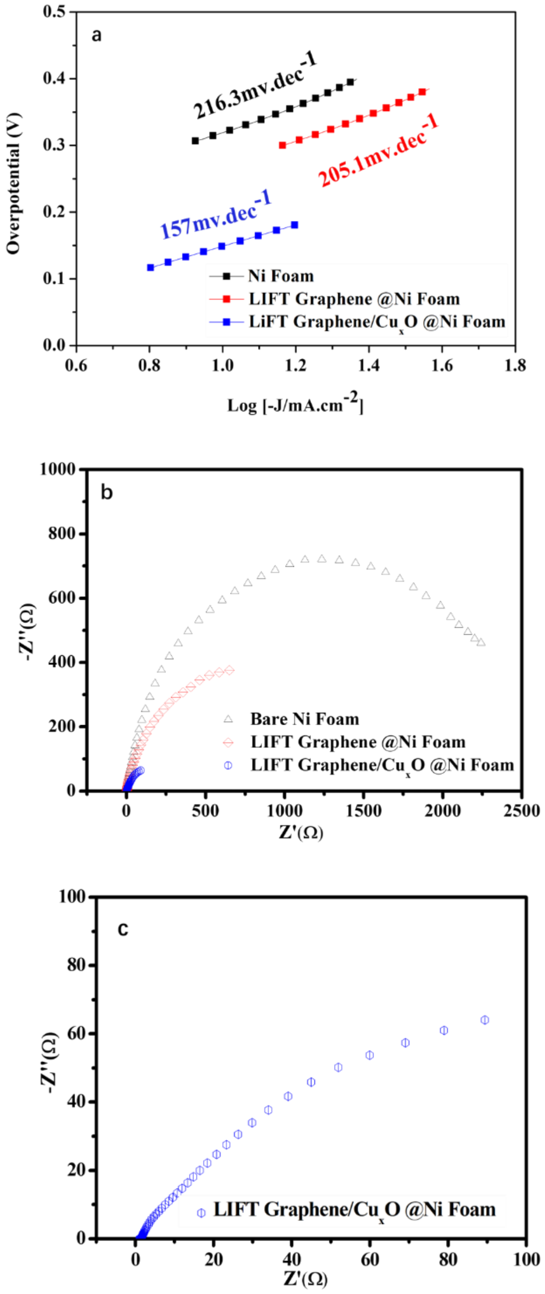

Figure 3.17 Tafel slopes(a) and EIS spectra of the three samples including Bare Ni Foam, LIFT Graphene @Ni Foam (b)and LIFT Graphene/Cu$_x$O @Ni Foam A magnified view of the EIS spectra of LIFT Graphene/Cu$_x$O @Ni Foam(c).

Table 3.1. Comparison of the HER performance of different Cu-based catalysts/electrodes obtained by different approaches

Catalyst/electrode	**Electrolyte**	**η(mV)@j mA cm^{-2}**	**Tafel slope (mV dec^{-1})**	**Preparation method**	**Reference**
LIFT Graphene/CuxO/NiF	1M KOH	149.6@10	157	Laser deposition	This work
Cu3P/CF	1M KOH	210@20	127	Anodization/calcination /Phosphorylation	J. Phys. Chem. C 2017, 121, 25875-25881
CuNPs/CNFs	0.5M H2SO4	200@10	152	CVD/carbonization/ electrospinning / thermal reduction	International journal of hydrogen energy 41(2016) 18044-18049
CoP@Cu2P-Cu3P/GC	1M KOH	118@10	72	Two-step nanocasting-solid phase phosphorization	Sustainable Energy Fuels DOI: 10.1039/d0se01745k
CuCo2Se4	1M KOH	125@10	--	hydrothermal method	ACS Appl. Energy Mater. 2020, 3, 3092-3103
CuO@Ni/NiFe hydroxides	1M KOH	125@10	86	Chemical oxidation-calcination /room-temperature interfacial Galvanic reaction	Electrochimica Acta 318 (2019) 695-702
Cu3P@NF	1M KOH	105@10	--	Hydrothermal method /phosphorization	ACS Appl. Mater. Interfaces 2017, 9, 2240-2248
Cu@NiFe LDH /CF	1M KOH	116@10	58.9	Chemical oxidation/air annealing /electroreduction/electrodeposition	Energy Environ. Sci., 2017, 10, 1820--1827
Cu2S@Cu	1M KOH	316@10	76	Sulfurization reaction	International journal of hydrogen energy 44(2019) 1620-1626
CMS/Ni	1M KOH	213@50	80	Hydrothermal method	Mater. Adv., 2021, 2, 455-463
Co–P/CuO CF	1M KOH	95@20	--	Chemical oxidation/ Air annealing/ electrodeposition	Dalton Trans., 2019, 48, 891–897
NiCoP@Cu3P/CF	1M KOH	54@10	72	Chemical oxidation /hydrothermal method	J. Mater. Chem. A, 2018, 6, 2100–2106
Cu@CoFe LDH	1M KOH	171@10	36.4	Chemical oxidation /electrodeposition	Nano Energy 41 (2017) 327–336
Copper-nickel-sulfide NWS	1 M alkaline	70@10	44	Multi-step wet chemistry strategy	Chem. Commun., 2019, 55, 8154--8157
CuCo2S4 TSAs	1M KOH	69@10	55.4	Hydrothermal method	J. Mater. Chem. A, 2020, 8, 1799–1807

Despite the presence of incompletely reacted precursors, the prepared electrode exhibited significant improvements in HER performance compared to pure nickel foam. In this study, from the perspective of HER performance, the presence of chlorine in the incompletely reacted precursor did not have a significant negative impact on the catalyst's performance and stability. To gain further insights into the catalytic kinetics of bare Ni foam, LIFT graphene @Ni foam, and LIFT graphene/CuxO @Ni foam, the Tafel slopes were calculated by linearly fitting the Tafel plots, as illustrated in Figure 3.17(a). The LIFT graphene/CuxO @Ni foam exhibited the lowest Tafel slope of 157 mV dec^{-1}, indicating superior electrocatalytic performance in the HER. Furthermore, electrochemical impedance spectroscopy (EIS) was conducted at the open circuit voltage across a frequency range of 10 mHz to 100 KHz to evaluate the electrocatalytic performance of these electrodes in the HER. By measuring the charge transfer resistance (Rct) in a 1 M KOH electrolyte solution, the Nyquist plots are shown in Figure 3.17(b). provided valuable information. The estimated values of Rct for bare Ni foam, LIFT graphene @Ni foam, and LIFT graphene/CuxO @Ni foam were 1481 **Ω**, 555 **Ω**, and 144.5 **Ω**, respectively. The significantly lower Rct value observed for LIFT graphene/CuxO @Ni foam indicates that the introduction of CuxO nanoparticles greatly enhances the electron transfer rate during the HER process. Remarkably, the catalyst consisting of bare Ni foam deposited with LIFT graphene/CuxO demonstrates a minimum overpotential of 149.6 mV, indicating a comparable HER performance to previously reported Cu-based catalysts obtained through different approaches (refer to Table 3.1).The electrochemical active surface areas (ECSA) of the three electrodes, indicated by the electrical double-layer capacitance (Cdl), were determined using cyclic voltammetry (CV) curves at various scan rates ranging from 5 mV/s to 200 mV/s, as depicted in Figure 3.18. The calculated values of electrochemical double-layer capacitance are shown in Figure 3.19. It is evident that the Cdl of bare Ni foam is 2.8 mF cm^2. In contrast, the value for LIFT graphene/Cu_xO @Ni foam is more than four times higher, suggesting that the presence of Cu_xO nanoparticles and porous graphene provides additional active sites. Consequently, the introduction of LIFT graphene/Cu_xO not only enhances the electronic transmission speed but also contributes to an increased availability of active areas, leading to improved electrochemical performance.

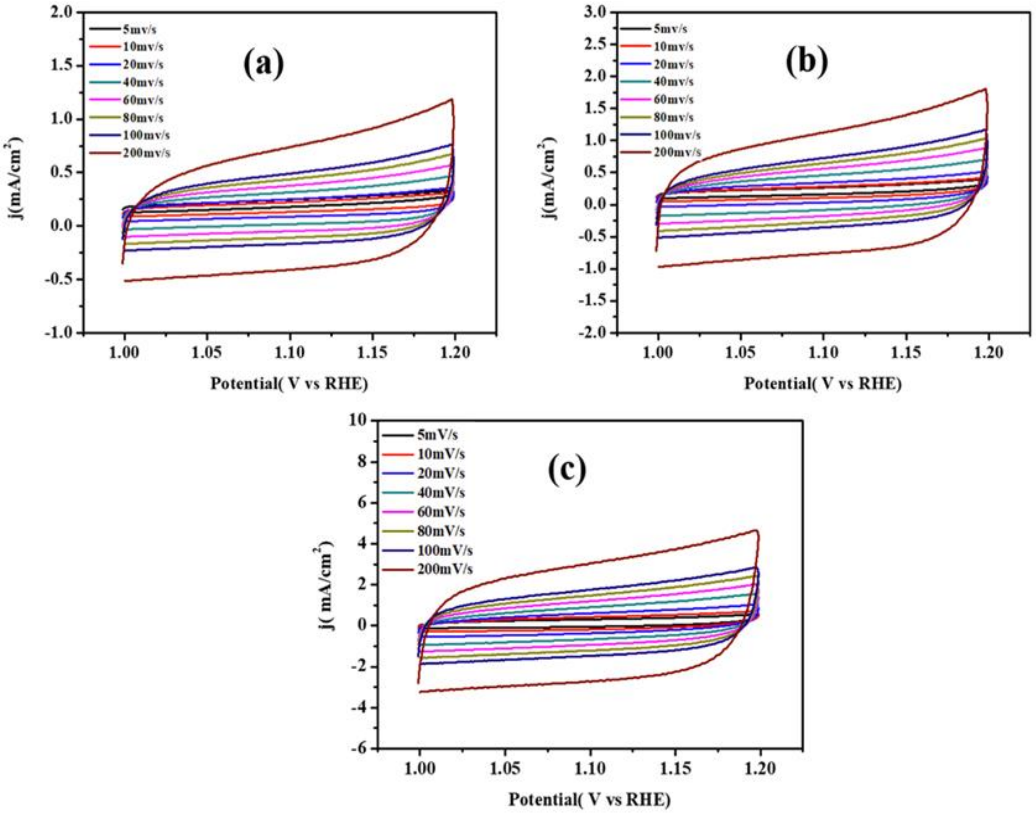

Figure 3.18 CV cures of bare Ni foam (a), LIFT graphene @Ni foam (b), and LIFT (c).

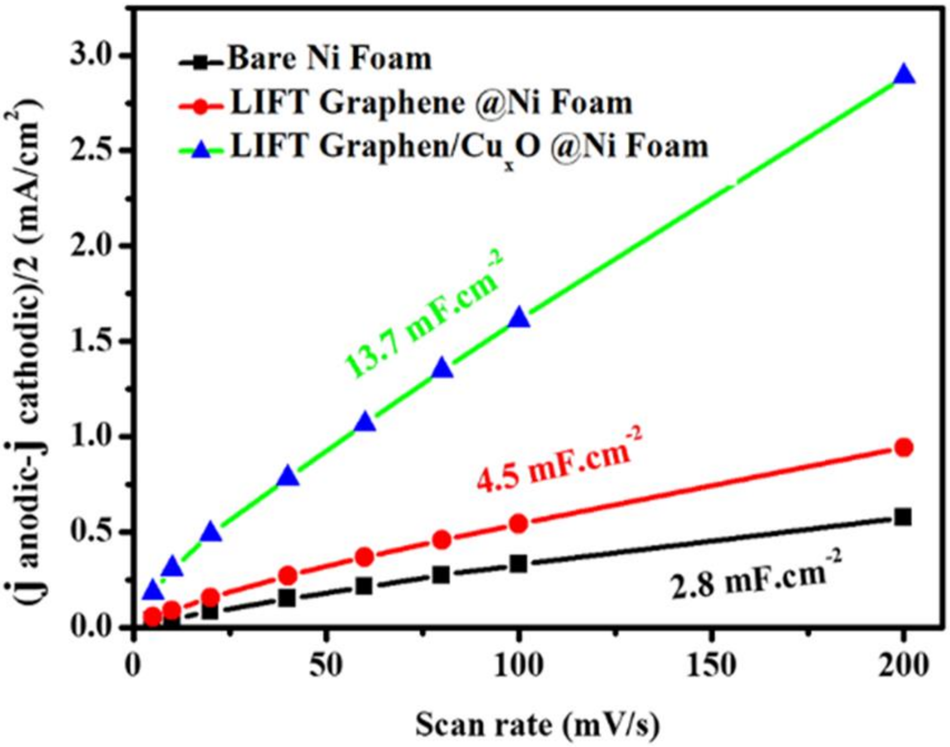

Figure 3.19 The Cdl of Bare Ni foam, LIFT graphene @Ni foam and LIFT graphene/Cu$_x$O @Ni foam extracted from CV curves at varied scan rates.

To assess the stability of the electrocatalytic activity of the LIFT graphene/CuxO @Ni foam electrode, it was subjected to 1000 cycles of cyclic voltammetry (CV) at a scan rate of 5 mV/s in a 1 M KOH electrolyte solution. Figure 3.20 (a) compares the initial catalyst's linear sweep voltammetry (LSV) plot with the LSV plot after 1000 CV cycles, showing no significant change in the electrocatalytic performance. This indicates that the catalyst maintains its activity even after prolonged cycling. Furthermore, the durability of the as-fabricated electrocatalyst was evaluated using chronoamperometry over a period of 10 hours in a 1 M KOH solution at a fixed overpotential of 186 mV, as shown in Figure 3.20 (b). The current density of the electrocatalyst remained nearly constant throughout the 10-hour electrolysis period, indicating excellent stability. Therefore, it can be inferred that the electrocatalyst exhibits long-term sustainability in the hydrogen evolution reaction (HER) under alkaline electrolyte conditions. The morphology of the graphene/Cu_xO catalysts after the CV cycling test was also checked (Figure 3.21(a) and Figure 3.21(b)), and there was no obvious difference. The graphene retains the porous structure highly dispersed on the Ni foam and the Cu_xO particles are also uniformly anchored in porous graphene. In addition, the EDX results (Figure 3.23) show a similar phenomenon of the element distribution. The TEM results of the graphene/Cu_xO before and after 1000 cycles CV tests are compared in Figure 3.22. The average size of nanoparticles is primarily in the range of 14-16 nm before and after CV cycling test, which further confirms the high stability of the catalyst.

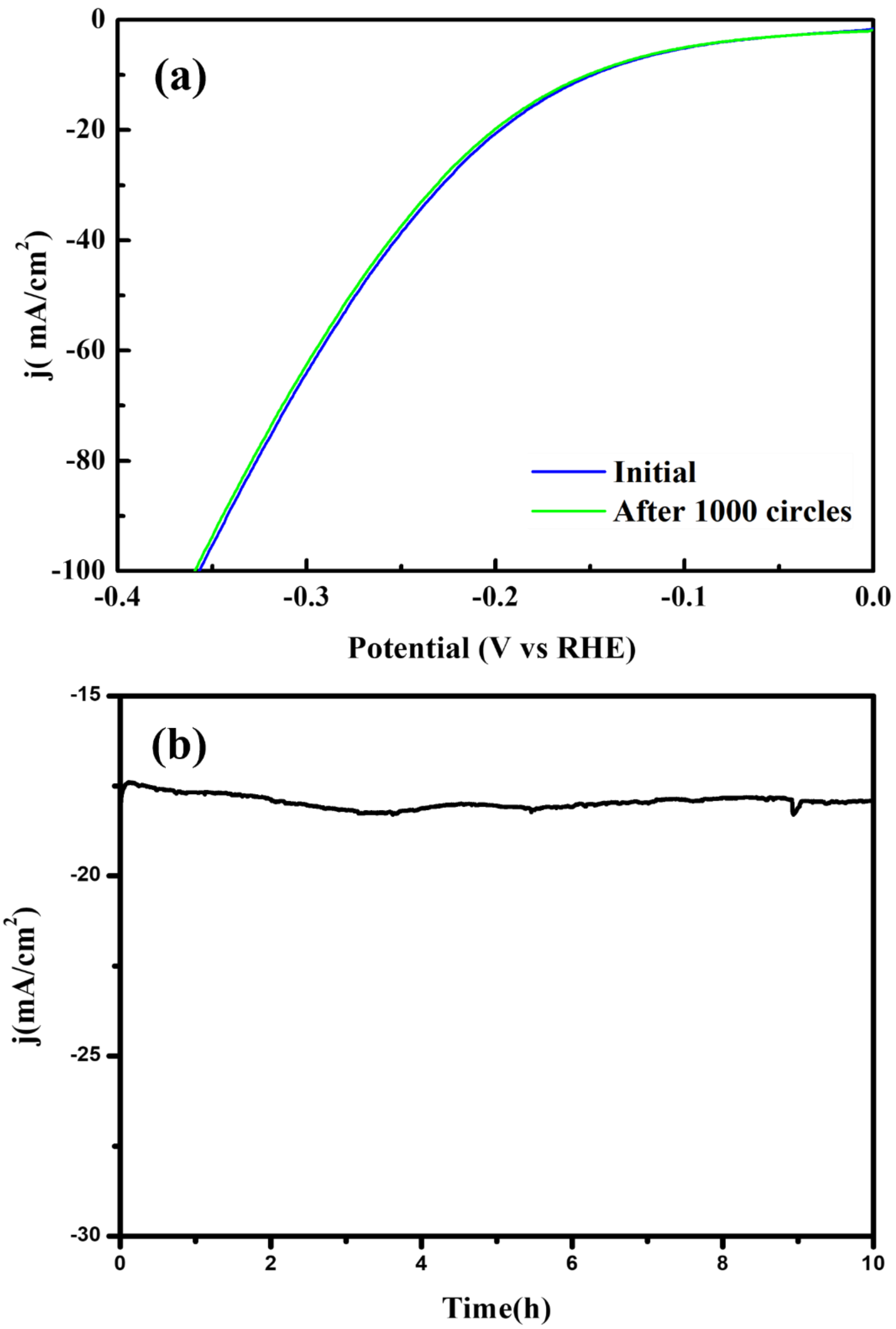

Figure 3.20 (a) Polarization cure of LIFT graphene/CuxO @ Ni foam electrode initially and after 1000 cycles, (b) Chronoamperometry curve of LIFT graphene/CuxO @Ni foam electrode during electrolysis over 10 h.

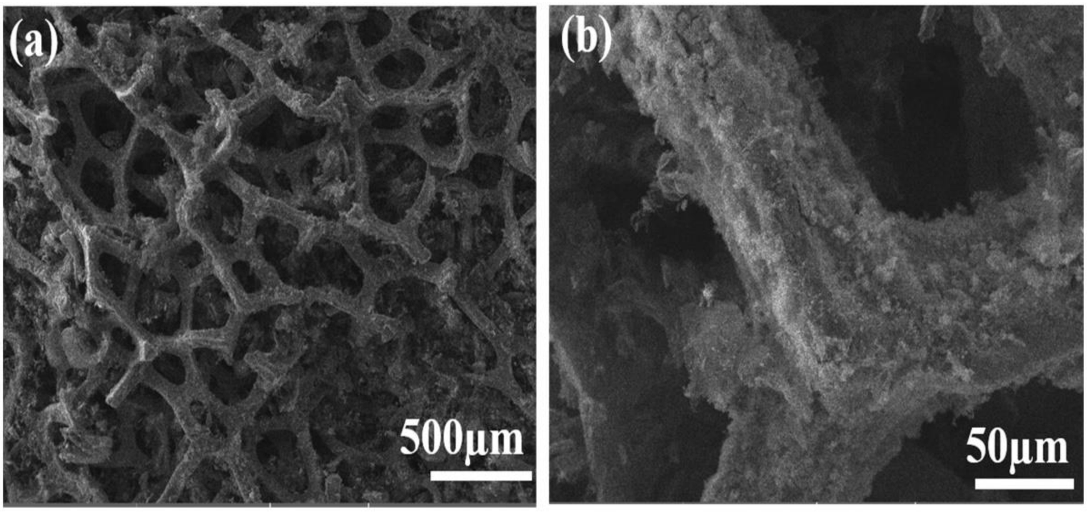

Figure 3.21 SEM images of the LIFT graphene/Cu_xO @Ni foam after 1000 cycles CV test.

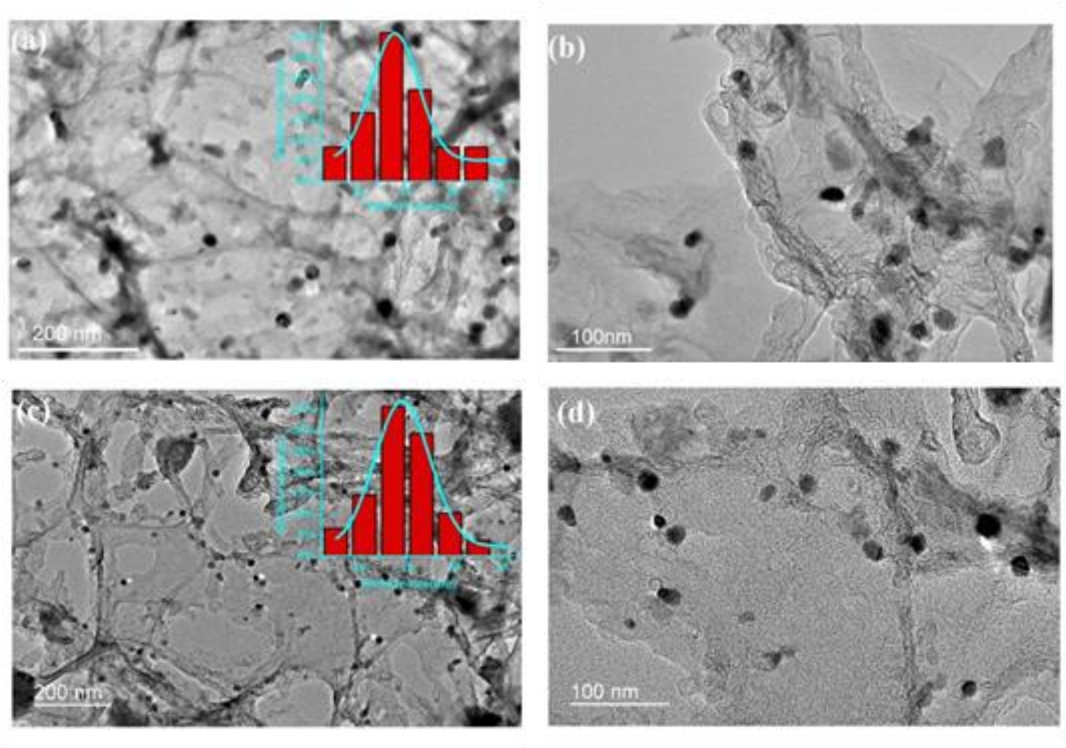

Figure 3.22 TEM images of (a), (b) initial LIFT graphene/Cu_xO,

(c), (d) LIFT graphene/Cu_xO after 1000 cycles CV test.

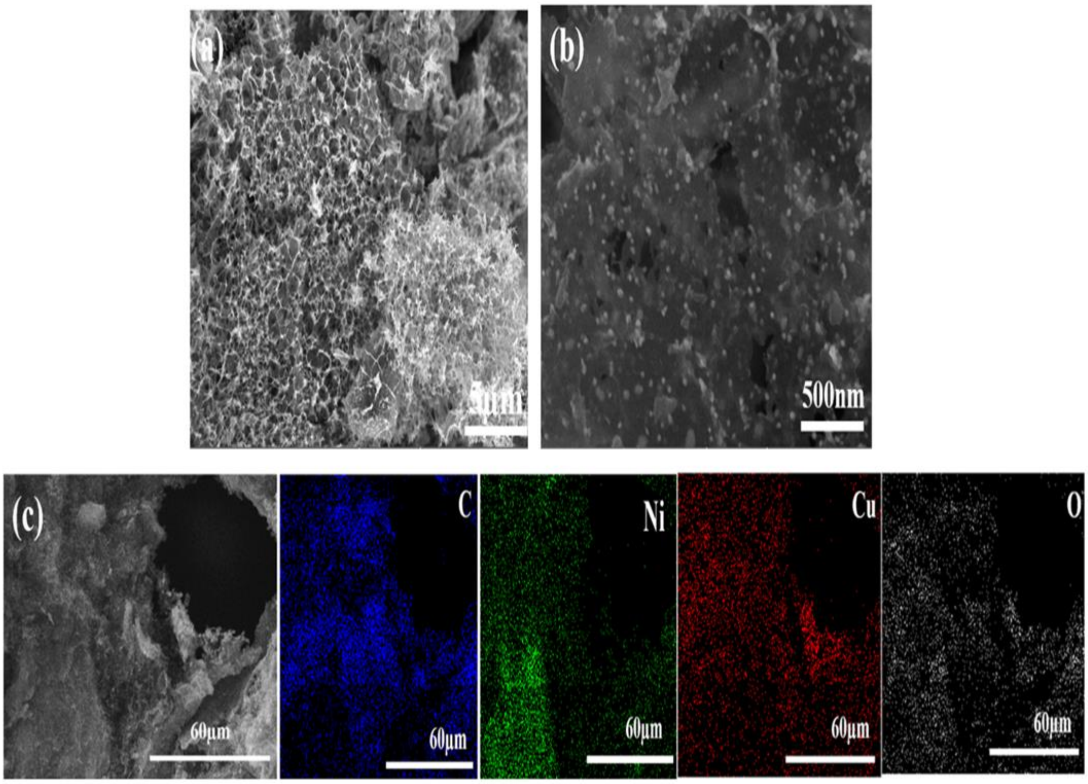

Figure 3.23 (a) (b) FESEM images of the porous LIFT graphene wrapped Cu$_x$O after1000 cycles CV test, (c) EDX mapping of the LIFT graphene wrapped Cu$_x$O after1000 cycles CV test.

3.4 Conclusion

In conclusion, a high electrocatalysis performance of LIFT graphene/Cu_xO @Ni foam electrode has been fabricated through a one-step laser deposition method. In this method, the $CuCl_2$, as the Cu precursor, can be easily reduced to Cu and Cu_2O through the laser beam. Thus, a novel nanocomposite can be obtained after introducing the laser induced porous graphene. The nanocomposite can be transferred to the Ni foam surface and closely combined with the Ni foam surface. The R_{ct} is measured as 144.5 Ω, and the electrical double-layer capacitor is obtained as 13.7 mF cm^{-2}. The nanocomposites can reduce the electronic transmission resistance and provide more active areas during HER. Hence, this electrocatalyst shows the enhanced HER activity, providing an overpotential of 149.6 mV and a Tafel slope of 157 mV dec^{-1} of HER. Meanwhile, the as-fabricated electrode has shown good stability in alkaline electrolyte solution. There is ignorable change of the electrocatalysis performance after 1000 cycle CV test and 10 h chronoamperometry test. This impressive result shows that the novel catalyst has a potential in terms of electrocatalytic HER activity. And, it can be extended cosmically, due to its simplicity and fast fabrication. It is foreseen that more electrocatalysts with outstanding HER performance will be accomplished by inspiring this work in the future.

Chapter 4

Efficient plasmonic enhanced solar evaporation achieved by laser-assisted Cu /Graphene nanocomposite

The previous chapter primarily focused on the fabrication of graphene composite materials using the one-step method of laser-induced forward transfer. In this section, a novel approach is introduced that combines thermal evaporation of metal nanoparticles with laser-induced forward transfer to produce a laser-induced graphene composite with copper nanoparticles. Its application in solar-driven interfacial evaporation for pure water harvesting is investigated.

4.1 Introduction

The energy crisis and freshwater scarcity are two pressing global challenges that pose significant threats to sustainable development. Efforts to address these issues have intensified in recent decades. One critical aspect is the exploration of solutions to mitigate the impact of these challenges. It is important to note that despite the abundance of seawater on Earth, its high salinity renders it unsuitable for direct use. Additionally, the rapid pace of industrial development has led to the depletion and contamination of limited freshwater sources. Disturbingly, estimates indicate that by 2025, approximately three billion people will face the daunting challenge of inadequate access to clean drinking water [163]. Addressing the aforementioned concerns, the purification of clean water from seawater or sewage emerges as a promising solution to alleviate the ongoing freshwater shortage. However, conventional technologies for seawater purification often require substantial energy consumption and incur excessive costs for infrastructure maintenance [164]. As an example, the widely used membrane-based reverse osmosis (RO) process, which stands for a massive portion of global desalination capacity, typically requires 2.5~4 kWh of electricity per cubic meter of purified water produced [165]. Furthermore, it is important to consider the significant environmental impact associated with conventional water purification methods. Therefore, there is a pressing need to develop environmentally friendly and sustainable approaches to obtain clean water, in order to address the critical water scarcity and energy challenges we currently face.

In nature, evaporation under natural sunlight is an ancient way and a typical application of photothermal conversion to generate clean steam, which happens at the surface water on earth every day. However, this sun-to-earth interaction is largely restricted by its unsatisfied evaporation efficiency. In the past decades, interfacial solar-driven steam generation has regained tremendous interest owing to the advanced strategies of material engineering for efficient photothermal utilization. Assuring efficient solar absorption and solar-to-heat conversion is the critical step for solar evaporation, which is largely determined by the solar absorber located at solar capture surface. Metals nanoparticles, semiconductor nanoparticles, conductive polymers, and carbon material are the four typical photothermal materials [47]. Carbon-based materials, known for their low cost, good stability, and broadband absorption, have found extensive applications in the field of solar thermal energy. Among these materials, two-dimensional graphene has gained significant attention due to its unique properties, including low density, large specific surface area, high photothermal conversion efficiency, tunable wettability, and excellent photostability. As a result, graphene has emerged as a popular material for solar evaporation applications [166-168]. Nevertheless, a significant challenge lies in effectively harnessing solar energy by tailoring graphene into three-dimensional (3D) structures. In recent years, graphene-based aerogels have garnered considerable attention for solar steam generation due to their distinct characteristics. These aerogels exhibit several unique features, including large surface areas, high porosity, low thermal conductivity, and low mass density. These properties make graphene-based aerogels highly desirable for efficient utilization of solar energy in steam generation applications [169, 170]. The inherent microstructures provide sufficient channels for solar capture and water transport [171]. Another approach to designing the structure of graphene-based materials is through 3D printing. Li et al. demonstrated the fabrication of a jellyfish-like evaporator using a vertical 3D printing method [172]. The vertical 3D printing method employed in this study facilitated the vertical alignment of reduced graphene oxide (rGO) pillars on a carbon/rGO composite substrate. This unique structure created numerous microchannels that enabled efficient vertical water transport and maximized heat transfer from the large contact surface to the feed water. As a result, a high energy conversion efficiency of 87.5% was achieved. Despite the widespread use of abundant carbon-based materials as cost-effective solar absorbers, their limited light absorption across the entire solar spectrum (typically ranging from 50% to 70%)

remains a hindrance to their broader application in solar evaporation [173, 174]. In terms of material design, the incorporation of novel composites or hybrids offers the potential to broaden and enhance solar absorption capabilities [175, 176]. An example of enhancing solar harvesting is achieved by incorporating nanostructured metal-based materials with localized plasmonic heating into carbon-based materials. This approach has been recognized as a possible strategy to further enhance solar absorption capabilities [177]. Metal nanoparticles (NPs) such as Au, Ag, Al, and Cu possess localized surface plasmon resonance (LSPR) absorption, which imparts them with unique optical responses across the solar spectrum [178]. Plasmonic graphene nanocomposites or nanostructures, which combine reduced graphene oxide (rGO) with gold nanoparticles (Au NPs) or silver nanoparticles (Ag NPs), demonstrate high optical absorption properties. These materials can be effectively utilized as solar absorbers in efficient solar water desalination systems [179]. Simultaneously, the development of cost-effective and efficient solar absorbers by combining carbon-based materials with non-noble metallic plasmonic components holds great significance for practical solar desalination applications. One proposed approach to enhance evaporation efficiency is through interfacial evaporation, which focuses the heat localization at the vapor generation interface rather than within the bulk water. This concept has the potential to greatly improve the overall efficiency of the evaporation process [180, 181]. The practice of floating the evaporator, either through a self-supporting method or by utilizing a buoyant substrate, is a well-known and effective approach to concentrate the solar-to-heat conversion specifically at the evaporation interface. This technique ensures that the solar absorber or layer stays at the air/liquid interface, improving the efficiency of heat transfer and evaporation. In a study by Chen et al[12], an interfacial solar-driven steam generator was fabricated using polypyrrole (PPy) in combination with hydrophilic open-cell melamine foam (MF). This design achieved an impressive evaporation rate of 2 kg/m2 h. However, solar-driven evaporation devices still face challenges regarding their salt resistance and long-term stability. Pioneering research has shown that incorporating a porous surface and establishing continuous water pathways can effectively reduce salt aggregation during the evaporation process [182-184].

In various applications, it is crucial to customize graphene for the construction of three-dimensional (3D) porous structures that offer both a high surface area and maintain its exceptional mobility and mechanical stability. Recently, laser direct writing has emerged as a green approach to fabricate porous-structured graphene by utilizing photothermal-induced transformation of portable carbon precursors. This method enables the expansion of 3D graphene's application scope in various fields, including supercapacitors, electrocatalysts, photothermal sterilization, and wearable devices [127, 128, 133, 185]. An efficient solar evaporator was developed by Chen et al., utilizing a membrane composed of laser-induced graphene (LIG) and polyimide (PI) [186]. The combination of the high porosity resulting from the porous structure of laser-induced graphene (LIG) and the fibrous structures of the polyimide (PI) substrate contributes to the excellent performance of the fabricated membrane in terms of solar absorption, water wicking, and vapor escape. To date, most reported

LIG generated through direct laser writing remains confined to polymeric substrates, limiting its modification and application possibilities. However, in our previous work, we successfully utilized the laser forward transfer method to deposit the porous-structured graphene composite onto specific target substrates. This advancement opens up new avenues for the modification and diverse applications of LIG beyond polymeric substrates [126, 129, 187]. Copper nanoparticles (Cu NPs), a widely recognized non-noble metal plasmonic material, demonstrate the localized surface plasmon resonance (LSPR) effect within the visible and near-infrared (NIR) regions [188]. In this study, we introduce a highly efficient and salt-resistant solar evaporator utilizing a composite material consisting of laser-induced graphene (LIG) combined with plasmonic copper nanoparticles (Cu NPs) as the solar absorber. The portable nature of this device enables its versatility in various applications. Impressively, it achieves an outstanding evaporation rate of 2.29 kg/m2.h under 1 solar irradiation. Moreover, the device demonstrates remarkable stability even in high salinity conditions (20 wt.% NaCl) due to the presence of micro-pathways within its structure.

4.2 Experimental section

4.2.1 Preparation of Cu NPs/LIG@ non-woven fabric evaporator

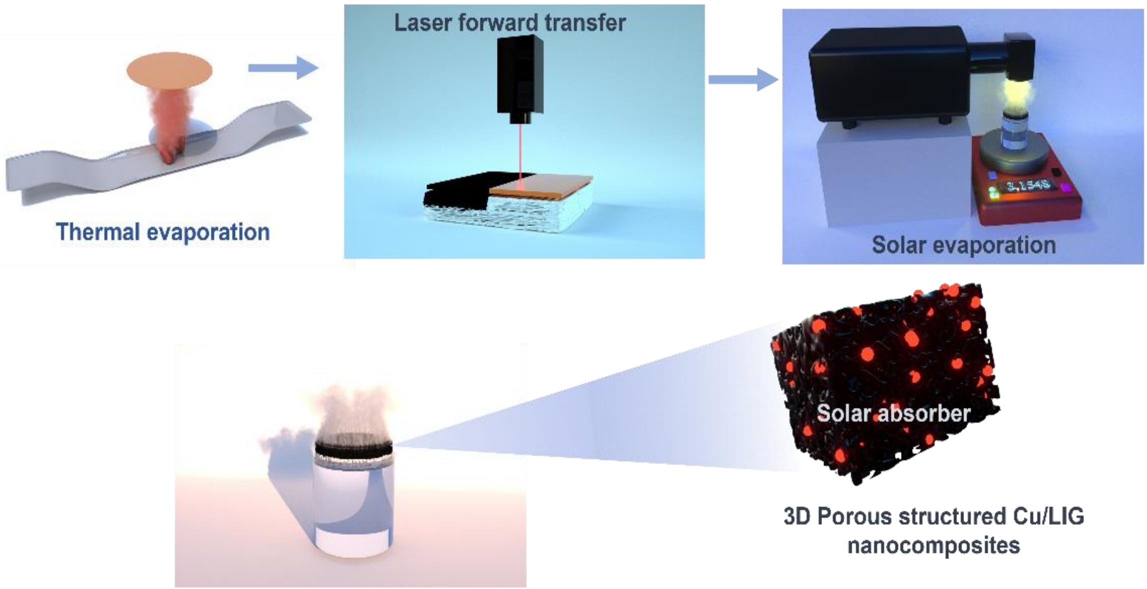

Figure 4.1 Schematic illustration of fabrication process of Cu/LIG@ non-woven fabric evaporator

The Polyimide (PI) sheets with a thickness of 50 μm were procured from Suzhou Kunleng Film Industries Co. Ltd in Mainland China for mass production. The water apportioning substrates for the evaporator were non-woven fabrics obtained from San Heng Yi Shu Non-Woven Products Limited Company in China. The construction process of the Cu/LIG@ non-woven fabric evaporator is illustrated in Figure 4.1. To synthesize and deposit the Cu NPs/LIG nanocomposite onto the hydrophilic non-woven fabric, a straightforward one-step laser-induced forward transfer method was employed. Initially, a Cu layer with varying thicknesses (10 nm/50 nm/100 nm) was coated onto the surface of the PI sheet using an Evaporation Apparatus (Beijing

Technol Company, ZHD-150A). The Cu-coated PI sheet was then positioned with the Cu layer facing the non-woven fabric on the laser machine workstation. Subsequently, the PI/Cu sheet was subjected to scribing using the DMG Lasertec40 (Figure 4.2) in the continuous wave (CW) mode. During the pretreatment, the laser energy was set at 5.5 W with a writing speed of 400 mm/s. In the post-processing step, the laser energy was adjusted to 0.3 W with a scribing speed of 800 mm/s. Through laser treatment, the graphene cladding integrated with Cu nanoparticles was transferred onto the surface of the non-woven fabric. This method allows for efficient deposition of the Cu/LIG nanocomposite onto the non-woven fabric, enabling the fabrication of the Cu/LIG@ non-woven fabric evaporator.

4.2.2 Instruments and characterization

To investigate the structure and characteristics of the novel plasmonic-enhanced evaporator membrane, several analytical techniques were employed. The surface morphology and structure were observed using a Tscan VEGA3 scanning electron microscope (SEM) (Figure 4.3). Particle size distribution analysis was conducted using a scanning transmission electron microscope (STEM), specifically the JEOL Model JEM-2100F (Figure 4.4). The crystal structure of the sample was determined using X-ray diffraction (XRD) with a Rigaku Smart Lab instrument (Figure 4.5). Raman spectra were measured using the WITEC Confocal Raman System (Figure 4.6). The optical absorption spectra of the prepared samples were obtained using a Hitachi UH4150 UV-VIS-NIR spectrophotometer (Figure 4.7). To investigate the surface temperature variation of the novel porous evaporator membrane, an infrared thermal imaging camera purchased from Fluke (Figure 4.8) and a solar radiation simulator from Honle were utilized. Additionally, the surface wettability of the membrane was observed and calculated using a Sindatek 100SB optical contact angle meter (Figure 4.9) through the sessile drop method. Through these analytical techniques, a comprehensive understanding of the structure, optical properties, thermal behavior, and surface characteristics of the plasmonic-enhanced evaporator membrane was obtained.

Figure 4.2 DMG Lasertec40

Figure 4.3 Tscan VEGA3 scanning electron microscope (SEM)

Figure 4.4 JEOL model JEM-2100F STEM

Figure 4.5 Rigaku SmartLab system

Figure 4.6 WITEC Confocal Raman System

Figure 4.7 Hitachi UH4150 UV-VIS-NIR spectrophotometer

Figure 4.8 Infrared thermal imaging camera

Figure 4.9 Sindatek 100SB optical contact angle meter

4.2.3 Solar evaporation experiment

The evaporation performance of the fabricated evaporator was assessed within a custom-built solar irradiation system. To simulate solar radiation, a solar lamp (WXS-50S-1.5, AM 1.5G) purchased from WACOM ELECTRIC Co., LTD was employed to provide a simulated solar spectrum. The evaluation of the steam generation rate was conducted under a solar irradiance of 1 kW/m^2. For the experimental setup, a simple interfacial evaporator with dimensions of 5cm × 5cm was suspended on the water surface inside a beaker. The beaker, along with the evaporator, was placed on an electronic balance connected to a computer. To calculate the evaporation efficiency of the novel porous evaporator membrane, the mass change of water was continuously monitored and recorded in real time, with the mass change under dark conditions subtracted for accurate measurement. Furthermore, an infrared thermal imaging camera was utilized to monitor and measure the surface temperature variation on the evaporator during the evaporation process. This allowed for the visualization and analysis of temperature distribution across the evaporator's surface.

4.3 Results and discussion

In this study, the selection of non-woven fabric as the support and water absorption layer was based on its favorable properties, including low weight and synergistic hydrophilicity. Figure 4.10 illustrates the physical characteristics of the plasmonic Cu NPs/LIG nanocomposite-coated non-woven fabric. Scanning electron microscopy (SEM) images presented in Figure 4.10(a) and Figure 4.10(b) reveal the aligned fibrous structure of the pristine non-woven fabric. Following the laser treatment, Figure 4.10(c) shows the formation of numerous micro-pores and architectures on the surface of the non-woven fabric, resulting from the presence of the porous Cu NPs/LIG nanocomposite. These pores have an approximate dimension of 100 μm. Additionally, Figure 4.10(d) provides a magnified view of the highly porous structured Cu NPs/LIG nanocomposite, which is stacked in multiple layers. The incorporation of the plasmonic Cu NPs/LIG nanocomposite onto the non-woven fabric results in a unique and highly porous architecture, significantly improving the performance and functionality of the composite material. This is demonstrated by the EDX mapping results shown in Figure 4.10(e) and Figure 4.10(f), which reveal the uniform distribution of Cu nanoparticles within the porous LIG on the fabric surfaces. The wettability of the evaporator was also investigated, as shown in Figure 4.11. The upper side of the evaporator exhibits excellent super-hydrophobic performance, with a water droplet contact angle (CA) of approximately 140° (Figure 4.11(a)). Additionally, the sliding angle (SA) of water on the upper side is very low, measuring around 1.4°, according to the test result. On the other hand, the bottom side of the evaporator demonstrates excellent water absorption performance from the dynamic water contact angle measurement. The unique characteristics of the evaporator highlight its dual functionality, with the upper side providing efficient water repellency and the lower side enabling effective water absorption. This design allows for enhanced control over the water evaporation process and significantly contributes to the overall performance and versatility of the evaporator system. The excellent super-hydrophobicity of the upper side can be attributed to the free stacking of the porous structured graphene. This arrangement creates a surface with high roughness and low surface energy, enabling the rapid shedding of water droplets and preventing their adhesion to the surface. As a result, the upper side exhibits exceptional water-repellent properties, promoting efficient steam generation during the evaporation process. The lower side of the evaporator, on the other hand, is designed to facilitate water absorption. This enables the effective utilization and retention of water, allowing for sustained evaporation and continuous operation of the evaporator system. By combining these two functionalities, the evaporator offers enhanced control over the water evaporation process, maximizing its efficiency and adaptability for various applications [189]. The fabricated evaporator exhibits intriguing wettability characteristics on both the upper solar absorption surface and the bottom water contact surface. The exceptional water absorption property of the bottom layer plays a significant role in facilitating efficient water transport to the evaporation interface. Simultaneously, the hydrophobic nature of the upper layer greatly enhances vapor escape while preventing heat transfer to the bulk water. The combination of these distinct wettability properties contributes to the overall performance of the evaporator. The bottom layer's excellent water absorption ensures a continuous and sufficient water supply to the evaporation interface, promoting efficient steam generation. At the same time, the hydrophobic upper layer effectively facilitates the escape of vapor, preventing heat loss and optimizing the energy conversion process. This unique wettability design enhances the evaporator's functionality, making it well-suited for applications requiring efficient water utilization, enhanced heat transfer, and improved energy conversion efficiency.

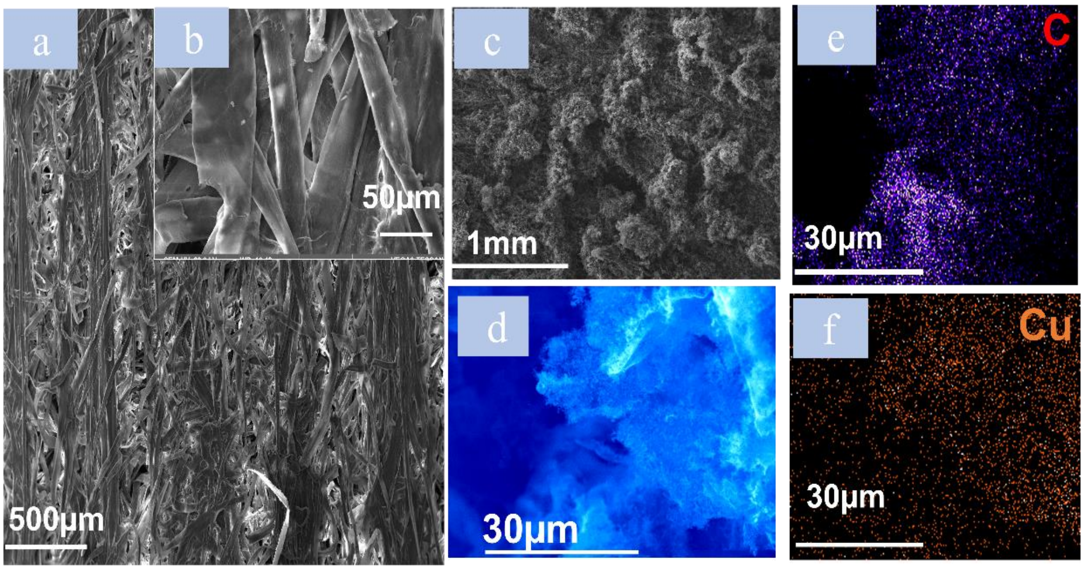

Figure 4.10 SEM images of the pristine non-woven fabric (a) and (b), Cu NPs/LIG coated non-woven fabric (c), Porous Cu NPs/LIG(d), Elements distribution of Cu NPs /LIG coated non-woven fabric (e and f).

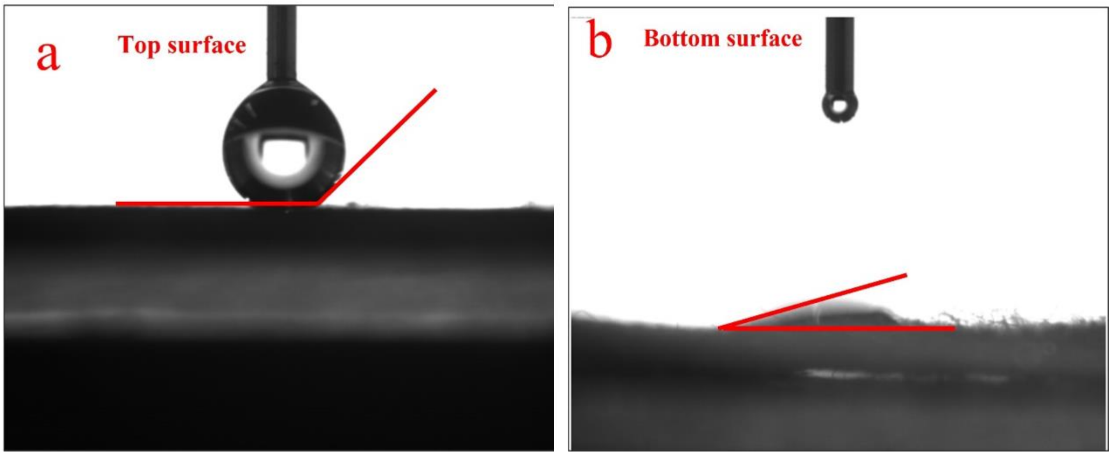

Figure 4.11 The water contact test of upper side(a) and bottom side(b) of the fabricated evaporator.

The distinctive catalytic, electrical, and optical properties of non-noble metal nanomaterials/nanostructures present a wide range of possibilities across various fields. These materials offer diverse opportunities for innovative applications, leveraging their unique characteristics [190-193]. Nevertheless, a challenge in the application of non-noble metal nanomaterials/nanostructures lies in optimizing the synthesis methods to precisely control their dimensional uniformity and morphology. This is crucial for achieving desired properties and ensuring consistent performance across different applications [194]. TEM analysis was conducted to investigate the morphology of the Cu NPs/LIG nanocomposite prepared from PI sheets coated with different thicknesses of Cu layer. The TEM images (Figure 4.15) revealed that the spherical Cu particles, ranging in size from a few nanometers, were uniformly dispersed within the graphene matrix. Notably, an increasing trend in nanoparticle size was observed with the increase in the thickness of the Cu layer. To confirm the crystal structure of the nanoparticles, X-ray diffraction (XRD) analysis was performed on the powder. The XRD pattern (Figure 4.12(a)) indicated that the peaks at 43.3º and 74.2º corresponded to the (111) and (220) planes of Cu, respectively (PDF#04-0836). This confirmed the metallic nature of the Cu NPs resulting from the laser treatment. However, a clear impurity peak was observed in the 100 nm Cu/LIG and 5 nm Cu/LIG samples, suggesting the presence of metal complexes induced in the graphene after laser treatment. Raman spectroscopy was employed to further investigate the formation of graphene during the laser treatment. The Raman spectrum (Figure 4.12(b)) showed three peaks at approximately 1348 cm^{-1}, 1583 cm^{-1}, and 2703 cm^{-1}, corresponding to the D peak, G peak, and 2D peak of graphene, respectively. These findings provided additional evidence for the successful formation of graphene through the laser treatment process.

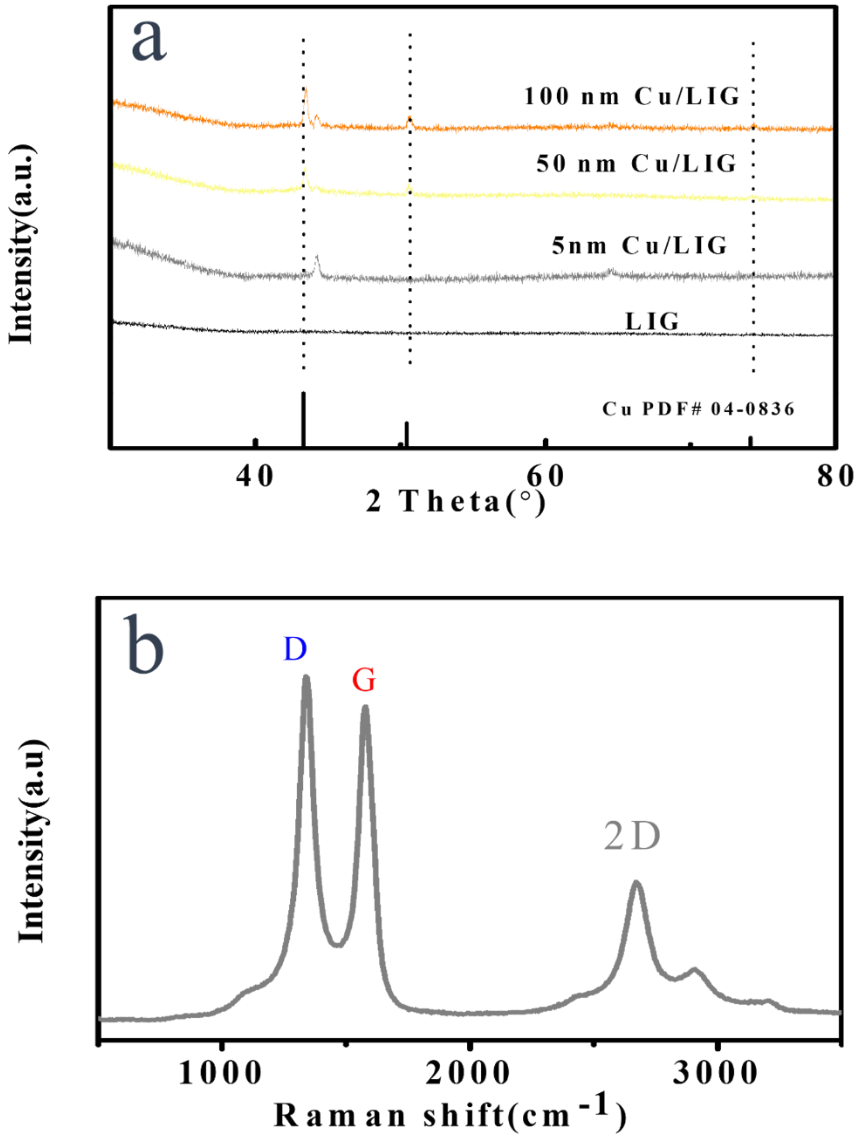

Figure 4.12 XRD patterns(a) of Cu NPs/LIG nanocomposite, Raman spectra(b) of LIG.

Figure 4.13(a) illustrates the light absorption characteristics of the laser-treated non-woven fabric evaporator incorporating plasmonic Cu/LIG nanocomposites. To examine the impact of Cu nanoparticle concentration on light absorption performance, Cu layers of varying thicknesses were initially coated on PI sheets for the fabrication of the solar steam generator. Thanks to the highly porous structures and innovative material design, the plasmonic Cu NPs/LIG nanocomposites, serving as the solar absorber in the evaporator, exhibit remarkable light absorption of over 90% across a broad solar spectrum. Compared to pure LIG, the inclusion of Cu NPs within the LIG matrix significantly enhances light capture and absorption, benefiting from synergistic optical effects. When a Cu layer of 50 nm or 100 nm is coated on the PI sheet, the resulting deposited nanocomposite demonstrates similar light absorption capacities. This observation aligns with the XRD results, indicating the presence of impurities induced during laser treatment of the PI/Cu 100 nm sample.

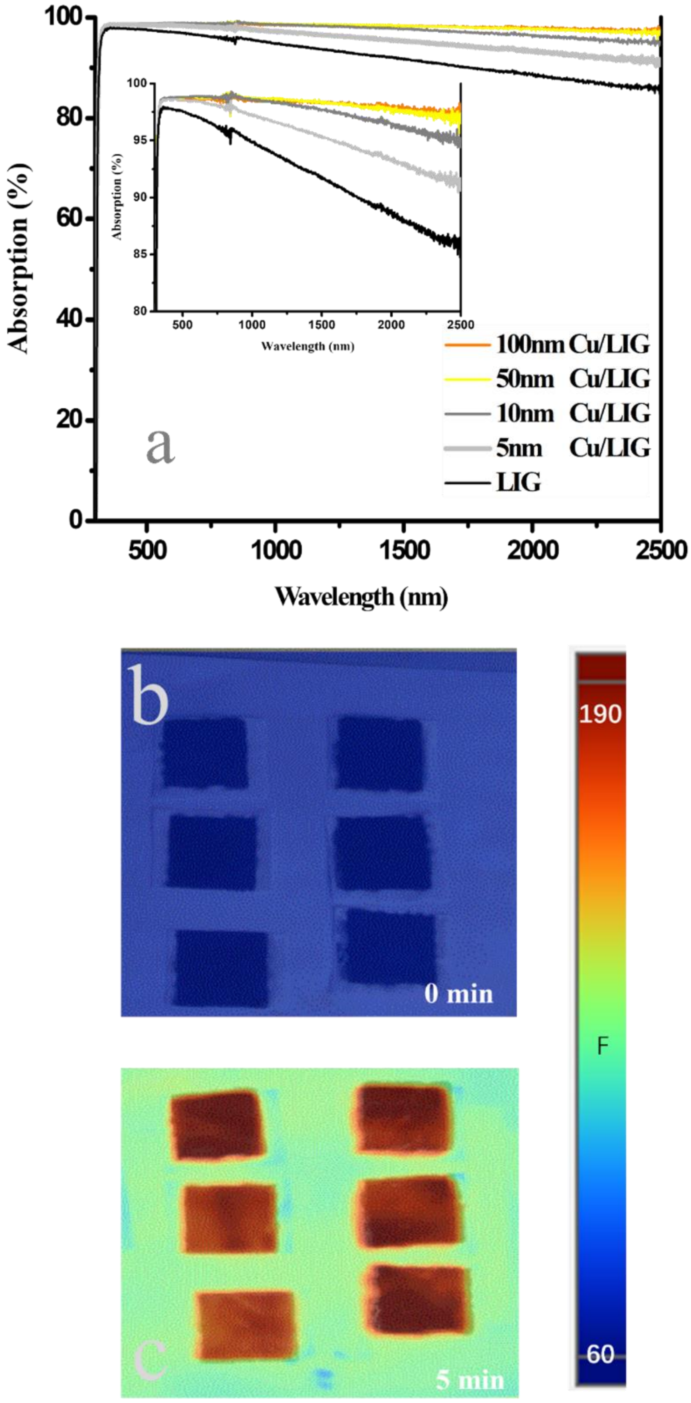

Figure 4.13 (a) Solar absorption spectrum of the fabricated evaporator from PI sheets coated by Cu layer in different thicknesses, (b) the IR camera images of the evaporator surface under 1 kW m^{-2} at 0 min and 5 min.

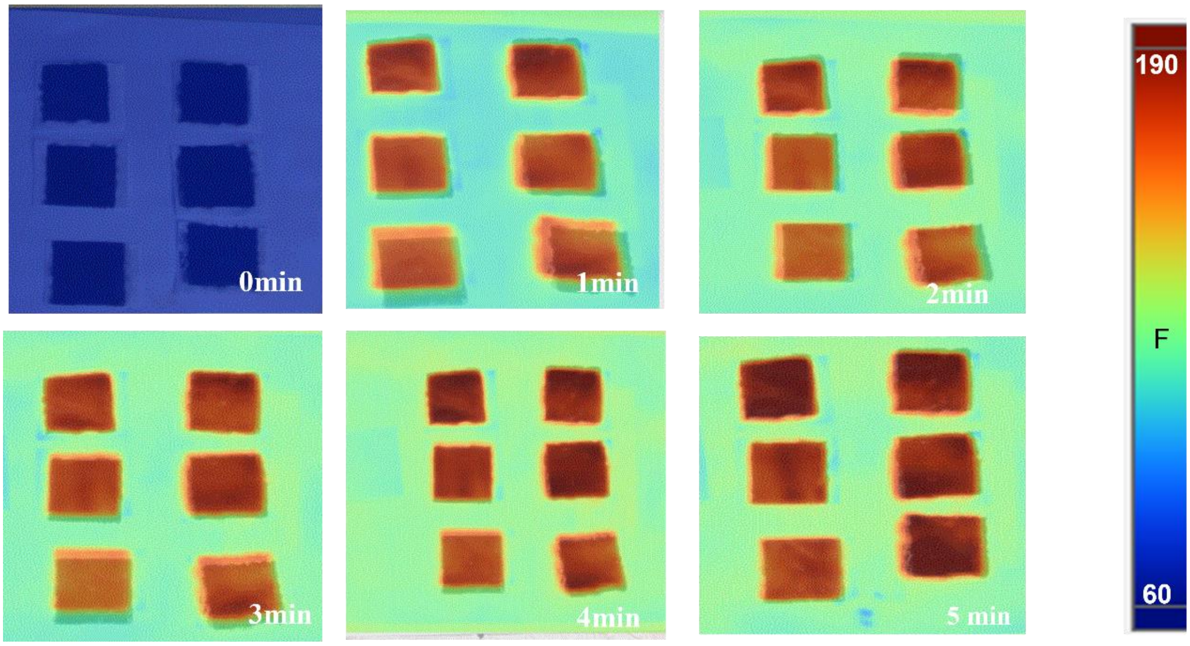

Figure 4.14 IR camera images of the evaporator surface made from different thickness Cu layer coated PI sheets (#LIG 1, #LIG2, #5nm Cu/LIG, # 10nm Cu/LIG, # 50nm Cu/LIG, #100nm Cu/LIG) under 1 kW m^{-2} solar illumination

Through calculations, the fabricated device achieves exceptional light absorption of over 98% across the entire solar spectrum (250 nm to 2500 nm) when the Cu layer thickness exceeds 50 nm. Photothermal conversion tests (Figure 4.13(b) and Figure 4.13(c))exhibit a consistent trend, with both the 50 nm and 100 nm Cu layers reaching a maximum temperature of 87℃ after 5 minutes (Table 4.1). This indicates that the incorporation of plasmonic Cu NPs significantly enhances the localized heating of the nanocomposites. The temperature increase over time is depicted in Figure 4.14. This revealed that the efficient solar absorption and photothermal conversion performance of the solar absorber were achieved when the thickness of the Cu nanocoating on the PI sheet reached 50nm. The synergistic light absorption and photothermal conversion effects of the obtained nanocomposite materials in this study were attributed to photothermal effect of carbon materials in synergy with the Localized Surface Plasmon Resonance (LSPR) photothermal effect copper nanoparticles. Therefore, the amount of Cu loaded on the 3-D graphene structure was identified as crucial, affecting both light absorption and photothermal conversion. Additionally, due to the excellent thermal conductivity of Cu, heat generated was efficiently transferred to the 3-D graphene structure. Consequently, the thickness of the Cu layer is vital for the solar-thermal performance of the prepared material, providing sufficient light absorption area, efficient photothermal conversion, and effective heat conduction. At the same time, combining production cost and performance, in this study, a copper layer thickness over 50 nm can achieve optimal material performance. From Figure 4.15, it can be observed that with the increase in Cu layer thickness, more Cu nanoparticles are loaded on the surface of graphene, providing additional sites for light absorption and enhancing the heat transfer performance.

Table 4.1 The surface temperature variation of the prepared samples under 1 solar illumination

	Sample					
Time	LIG1	LIG2	5nm Cu/LIG	10nm Cu/LIG	50nm Cu/LIG	100nmCu/LIG
0s	20.7	20.8	20.9	22.1	20.9	21.2
60s	70.0	71.3	73.1	76.7	78.9	80.5
120s	70.6	71.9	77.5	76.9	81.3	82.9
180s	74.4	77.8	84.4	83.2	85.9	86.5
240s	75.7	77.9	84.8	83.8	86.3	87.0
300s	76.8	78.2	85.1	84.5	87.2	87.8

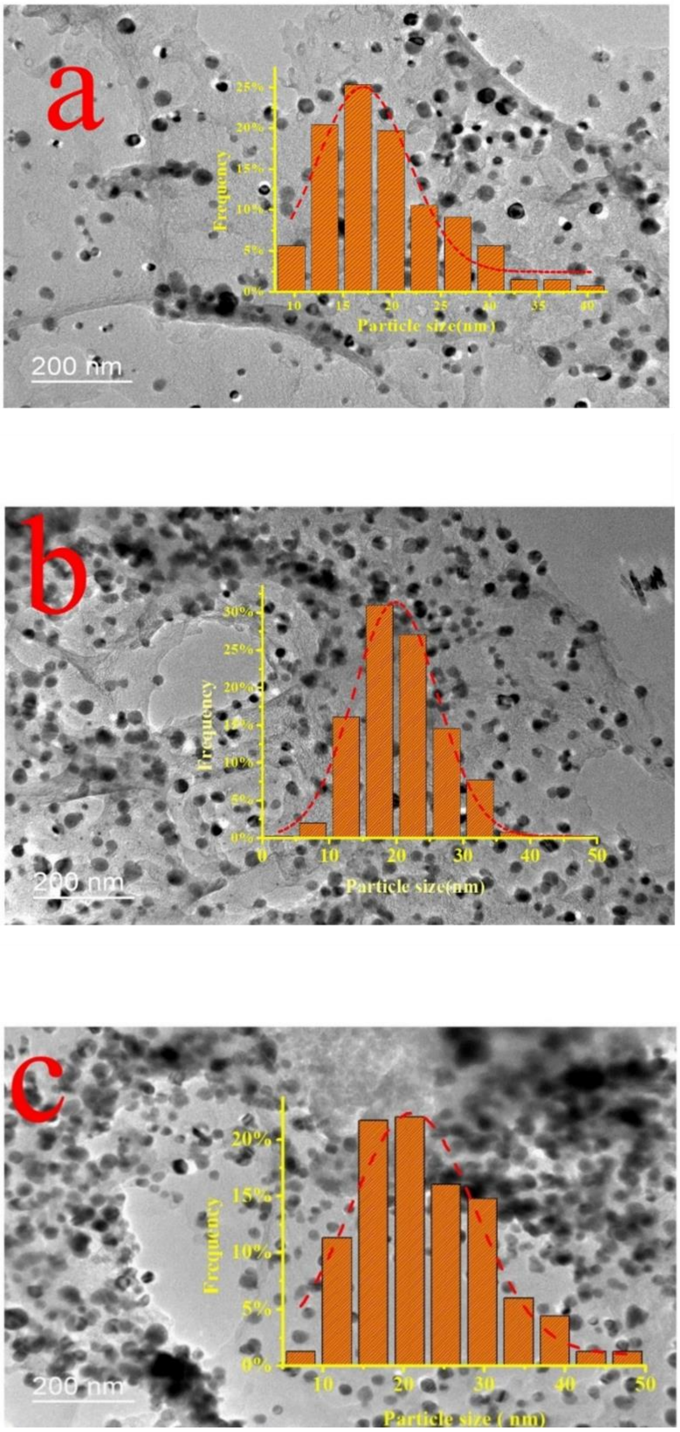

Figure 4.15 TEM images of Cu NPs/LIG nanocomposite made from 10 nm Cu/PI sheet(a)，50nm Cu/PI sheet (b), 100 nm Cu/PI sheet (c)

Figure 4.16(a) displays the mass change of the evaporation system with an exposed solar evaporation area of 25 cm^2 under simulated illumination of 1 kW/m^2. Real-time recording of the weight loss of the experimental set-up was conducted during clean water evaporation. The introduction of plasmonic Cu NPs in the solar absorber resulted in a significant increase in weight loss for the evaporation system. Notably, the evaporator prepared with a 50 nm Cu layer and a 100 nm Cu layer exhibited a nearly identical and the highest evaporation rate of 2.29 kg/m^2 h. When subjected to 20 wt.% NaCl saltwater, the desalination rate of the system was measured at 1.82 kg/m2 h (Figure 4.16(b)). Furthermore, the evaporator fabricated with the 50 nm Cu/PI sheet demonstrated stable evaporation efficiency during a long-term desalination process (Figure 4.16(c)). To maintain the performance of Cu NPs and their plasmonic effect, preventing their oxidation is crucial. Encapsulating Cu nanoparticles with a porous graphene layer serves as an effective strategy for maintaining performance. Additionally, the evaporator's anti-salt capability plays a vital role in sustaining long-term evaporation efficiency. Importantly, no visible salt crystallization occurred on the surface of the evaporator based on the plasmonic Cu NPs/LIG nanocomposite (Figure 4.16(d)). This outcome can be attributed to two factors. Firstly, the super hydrophilic non-woven fabric as the bottom substrate ensures rapid and continuous water transfer to the solar absorption layer, reducing the likelihood of salt formation. Secondly, the micro-pores formed by the stacked porous LIG provide ample and unobstructed pathways for spontaneous salt diffusion along vertical concentration gradients. These combined factors contribute to the evaporator's ability to maintain efficient evaporation while preventing salt accumulation.

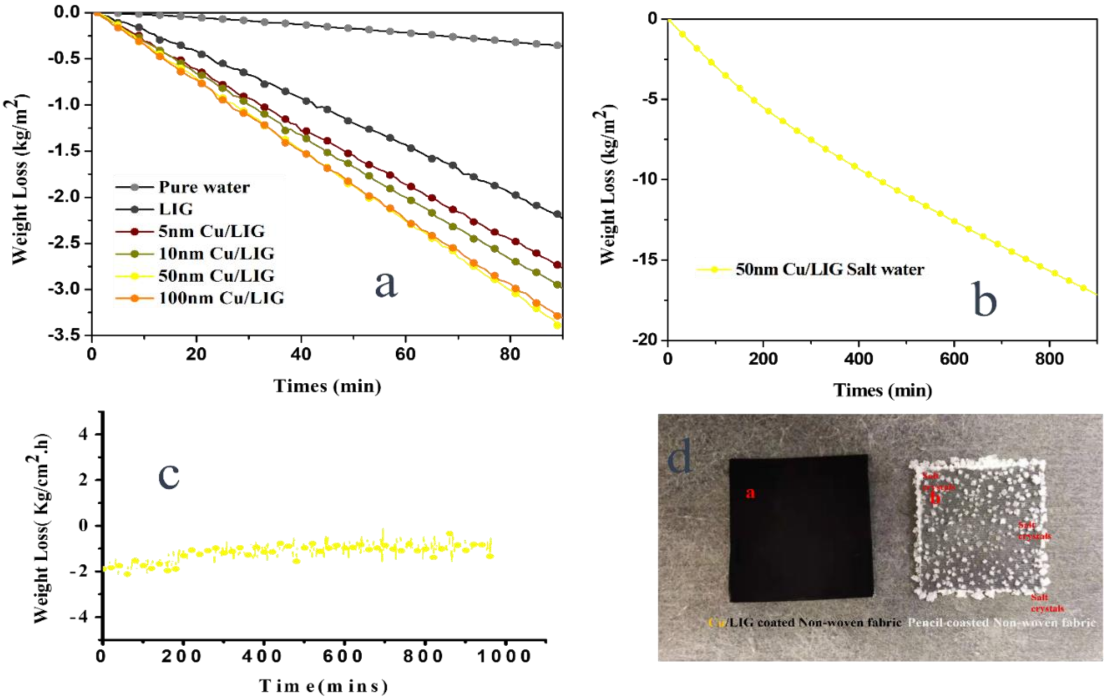

Figure 4.16 The weight change of the fabricated evaporator from different thickness Cu layer/PI films on clean water evaporation, (b) saltwater evaporation, (c) under solar irradiation of 1 kW.m-2, the calculated evaporation rate of the evaporator, (d) the salt formation on the evaporation surface(d).

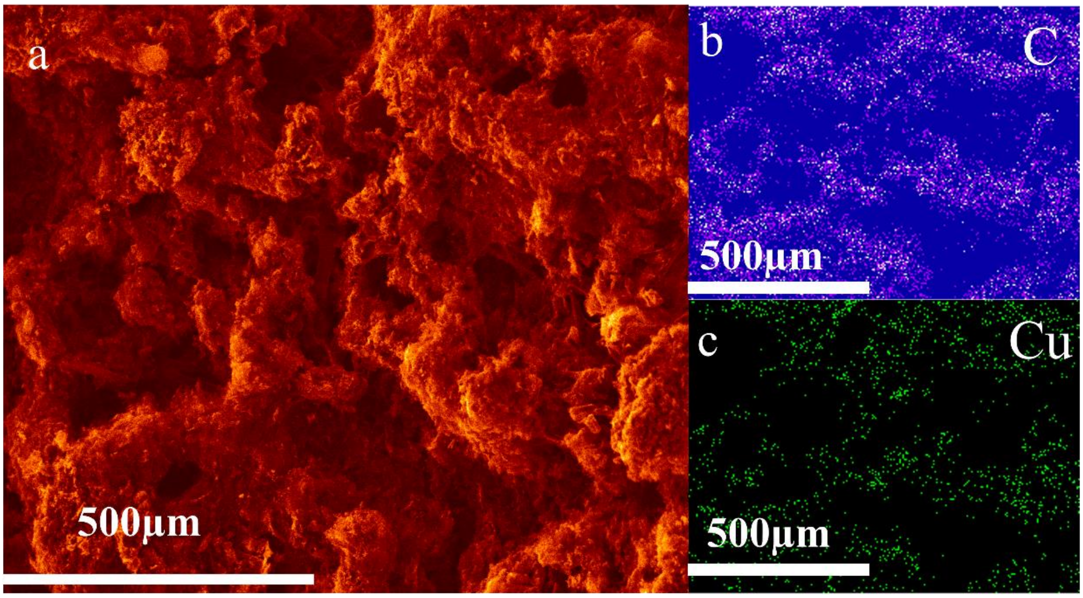

Figure 4.17 （a）SEM images of Cu NPs/LIG composite coated evaporator after durability test, (b) (c) Elements distribution

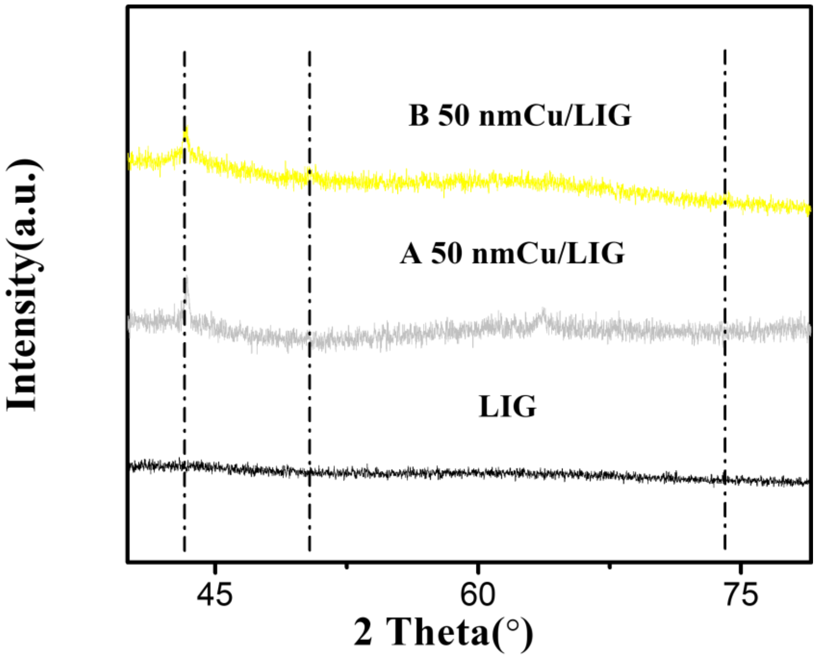

Figure 4.18 XRD patterns of 5nm Cu NPs/LIG nanocomposite before (B 50 nm Cu/LIG) and after (A 50nm Cu/LIG) the durability test

The tested samples were subjected to physical property analysis. From the SEM results (Figure 4.17), it can be observed that the morphology of the Cu NPs/LIG nanocomposite material on the evaporator remains intact, exhibiting a porous structure with clearly visible and well-preserved stacked pores. Additionally, combined with EDX analysis, it is evident that the Cu nanoparticles in the Cu NPs/LIG nanocomposite are uniformly distributed on the porous LIG substrate. The XRD results of the tested material (Figure 4.18) indicate that the crystalline structure of the Cu nanoparticles remains unchanged, suggesting that they were not corroded by water or oxygen during the interface evaporation process. In conclusion, it can be verified that this material can maintain its structural stability and integrity during long-term use in the interface evaporation process, thereby ensuring the durability of its performance.

To assess the practical applicability of the fabricated evaporator under natural solar illumination, a simple outdoor prototype was constructed (Figure 4.19(a)). The prototype consisted of an evaporation box with four inserted layer evaporators (3.5 cm × 10 cm) floating on a water sink. The setup was placed on the open terrace of The Hong Kong Polytechnic University on 28th November 2021.To evaluate the solar evaporation performance, the outdoor experiment commenced at 7:00 a.m. and concluded at 5:00 p.m. on a sunny day (Figure 4.19(b)). The generated clean water was collected and weighed. Throughout the 10-hour outdoor evaporation process, an average evaporation rate of 0.18 L/m^2.h was observed. To ensure the quality of the purified water, a sample resistance test was conducted. The test results indicated that the resistance values for saltwater and purified water were 1.5 MΩ and 24.3 MΩ, respectively (Figure 4.19 (c) and Figure 4.19 (d)). These findings confirm the successful purification of water through the evaporation process.

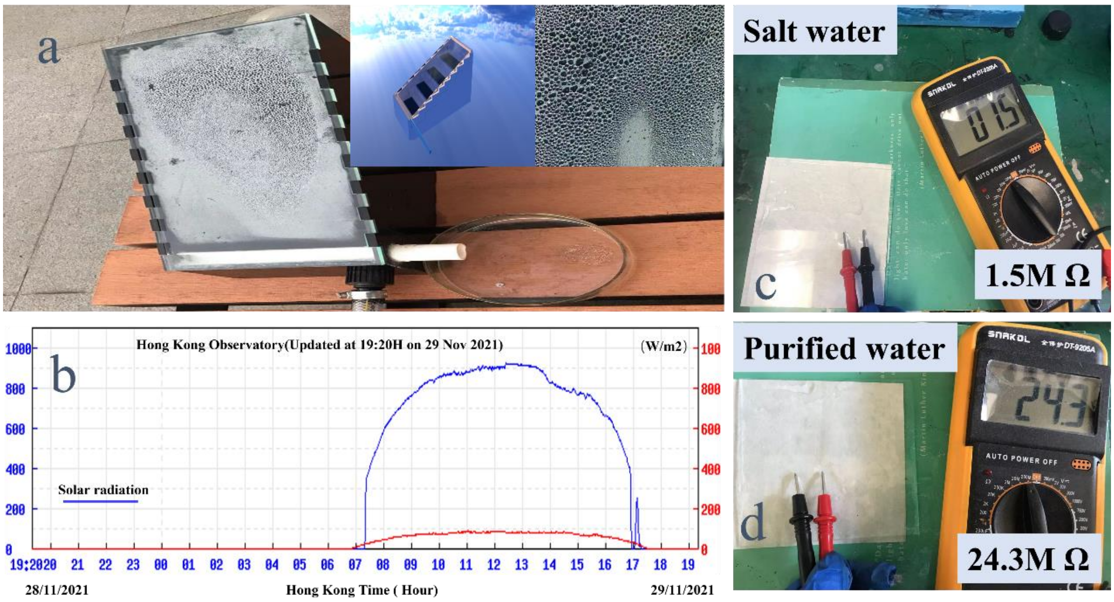

Figure 4.19 (a) the prototype for the outdoor experiment (b) the solar irradiation data on a sunny day (c) Resistance of saltwater and (d) purified water.

4.4 Conclusion

In summary, we successfully developed a portable solar steam generator by employing a facile one-step laser deposition method to create a plasmonic Cu NPs/LIG nanocomposite with super-hydrophobicity on the upper side. This nanocomposite serves as an efficient solar absorber, exhibiting high optical absorption and solar-thermal conversion capabilities. The evaporator achieved an impressive water evaporation rate of 2.29 kg/m^2.h. Its exceptional performance in saltwater evaporation makes it a promising solution for addressing freshwater scarcity in the future. The well-designed wettability structure of the evaporator contributes to its desirable anti-salt capacity, enabling a continuous evaporation process for long-term applications. Importantly, the fabrication process is environmentally friendly and can be scaled up for large-scale implementation. The utilization of low-cost raw materials and a fabrication method demonstrate significant potential for enhancing the efficient utilization of solar energy and enabling scalable clean water generation.

Chapter 5

Flexoelectric energy harvesting achieved by external polarization of nonpolar single-walled carbon nanotubes

Functionalization is another important strategy for the preparation of novel carbon nanomaterials. In the context of renewable energy utilization, functionalization of carbon nanomaterials can enhance their performance and broaden their applications. Therefore, in this chapter, we investigate the engineering interface enhancement of carbon nanotubes through surface functionalization, focusing on the flexoelectric effect and energy harvesting.

5.1 Introduction

Piezoelectricity is a widely recognized phenomenon in electromechanics that describes the relationship between induced electric polarization and applied strain. Extensively studied, this coupling has found various applications in energy harvesting, sensors, and transducers [195-197]. Piezoelectricity is commonly observed in materials that possess a non-centrosymmetric crystal structure, such as piezoelectric ceramics. However, certain polymers, such as polyvinylidene fluoride (PVDF) and certain liquid crystal polymers, also exhibit piezoelectric properties [198, 199]. Piezoelectric materials lack inversion symmetry, which enables deformations to induce internal polarizations due to the absence of ionic charge compensation [200]. This characteristic gives rise to the piezoelectric effect. Additionally, the flexoelectric effect, which refers to the electrical polarization induced by a strain gradient in a material, has gained significant attention as another form of electromechanical coupling phenomenon [201]. Unlike piezoelectricity, flexoelectric effects can occur in crystals with Centrosymmetry [202]. In solid ionic crystals, for instance, flexoelectricity arises from the displacement of ions when subjected to a nonuniform strain. This phenomenon allows for the generation of electrical polarization, highlighting the unique nature of flexoelectricity in materials without inherent piezoelectric properties [203]. In soft materials, such as certain polymers or liquid crystal materials, the flexoelectric response arises due to the reorientation of polarized molecules [204-206]. When these materials experience a nonuniform strain, the polarized molecules within them undergo reorientation, resulting in the generation of an electrical polarization. This unique behavior highlights the flexoelectric effect in soft materials, where the reorientation of polarized molecules plays a crucial role in the electromechanical coupling phenomenon.

Flexoelectricity was first termed by Kogen, inspired by the research conducted by Tolpygo and Mashkevich, who discovered that inhomogeneous deformations of the lattice (acoustic and optical phonons) in homopolar crystals like silicon can generate electrostatic potential [207]. Unlike the piezoelectric effect, flexoelectricity is not restricted to materials with unsymmetrical structures, and it also exhibits less dependence on temperature [208, 209]. These characteristics make flexoelectricity highly promising in the field of material science and electronic devices. Moreover, by reducing the size of the material to micro- and nanoscales, the strain gradients and electric dipoles become more pronounced [210, 211]. This size reduction effectively enhances the flexoelectric response, opening up possibilities for further advancements in flexoelectric-based technologies. Such enhancements in flexoelectricity at the micro- and nanoscales have significant implications for the development of miniaturized devices and systems with improved performance and efficiency [212]. Although the flexoelectric effect was discovered in 1960, it was largely overlooked for a long time due to its minimal impact on the macroscopic scale [211]. However, recent advancements in nanotechnology have sparked renewed interest and accelerated research on flexoelectricity across various fields. Unlike the piezoelectric effect, flexoelectricity is not limited by material symmetry and is believed to exist in most dielectric materials. As a result, extensive theoretical and experimental studies have been conducted to investigate and understand the flexoelectric effect [213]. The fundamental theory of flexoelectricity plays a crucial role in comprehending this phenomenon in different materials and exploring its potential applications. With a deeper understanding of flexoelectricity, researchers can unlock its potential for use in various devices and systems. This renewed focus on flexoelectricity has the potential to revolutionize fields such as energy harvesting, sensors, actuators, and micro/nanoelectromechanical systems (MEMS/NEMS) [214, 215]. By harnessing the flexoelectric effect, novel technologies and devices with enhanced performance and functionality can be developed, paving the way for future advancements in material science and electronic devices.

However, the mechanism of the flexoelectric effects is complex in different materials [211]. It is regarded that the caused nonuniformed strain can disrupt the symmetry of the materials to form lattice deformation, flexoelectricity can exist in all dielectric materials. For all the solid ionic materials， the flexoelectricity can be described together with the piezoelectricity as the electric polarization component P_i. . Initially, there has been long term the flexoelectricity cannot be distinguished from the piezoelectric effect due the limited understanding and lack of theoretical research. For the non-conductive materials and structures, the termed flexoelectric effect will result from the induced polarization upon the deformation of the structure when being subjected to a nonuniform strain gradients [216]. However, the flexoelectric effect is hardly detected due to that the materials' electric polarization will encompasses both effects, especially when the measurement is conducted at macroscopic level, posing significant challenges to study the flexoelectric effect in the materials [217]. Herin, some scholars tried to conduct the measurement to exclude the influence of piezoelectric response [218, 219]. The value of the flexoelectric coefficient is to quantify the magnitude of the materials' flexoelectric effect. Thus, the flexoelectric effect is centrosymmetric materials without piezoelectric effect has been thoroughly studied. Take the cubic crystals with symmetric structures for instance, the measurement of flexoelectric response includes transverse flexoelectric response, longitudinal flexoelectric response and shear flexoelectric response [220]. According to the equation, the piezoelectric constant of d is zero for Centro-symmetry crystals, while the flexoelectric constant can be induced by the disrupt of the inversion symmetry. Therefore, the flexoelectric effect is more universal than the piezoelectric effect. Measuring the flexoelectric coefficient requires introducing strain gradients in the material. However, generating and controlling precise strain gradients is a complex task that requires sophisticated experimental techniques and equipment. In experiments, it is necessary to apply precise mechanical deformations or strain gradients and measure the resulting changes in polarization, which can be challenging for many materials. The heterogeneity of materials can pose challenges in measuring the flexoelectric coefficient [221]. Real materials often exhibit non-uniform structures, compositions, or lattice defects, which can affect the generation of strain gradients and the accuracy of measurement results. This heterogeneity adds complexity to the measurement of the flexoelectric coefficient [222]. The flexoelectric effect is typically a phenomenon at the microscopic scale, involving the microstructure and charge distribution within the material. Therefore, measuring the flexoelectric coefficient requires high-resolution characterization and analysis of the material to understand the polarization response at the microscopic level. This presents challenges for many materials and requires the use of advanced experimental and theoretical techniques. The differences between flexoelectric testing and simulation results can be attributed to several factors, including experimental conditions, material properties, boundary conditions, model assumptions, and experimental techniques and measurement errors [223, 224]. To better understand and apply the flexoelectric effect, it is necessary to consider these factors comprehensively and conduct accurate experimental and simulation analyses.

Soft materials often exhibit non-centrosymmetric molecular structures, such as in liquid crystals, providing the foundation for the flexoelectric effect [225]. The mechanism of flexoelectric response in soft materials is more complicated due to its non-centrosymmetricity. Understanding and controlling the mechanism of the flexoelectric effect in soft materials are of great significance for the development of new soft electronic devices and smart materials. In non-centrosymmetric materials, strain gradients give rise to non-uniform charge distribution, leading to polarization. For example, the orientation and alignment of molecules in soft materials play a crucial role in the flexoelectric effect [205]. When soft materials experience external forces or strains, the molecular orientation and alignment change, resulting in non-uniform charge distribution and triggering the flexoelectric response. By controlling the molecular orientation and alignment, the flexoelectric effect can be enhanced. Soft materials typically exhibit high energy dissipation and deformation capabilities. When subjected to external forces or strains, soft materials undergo elastic deformation and energy dissipation. The interaction between these changes and charge distribution leads to the occurrence of the flexoelectric effect. The energy dissipation and deformation characteristics of soft materials contribute to their significant flexoelectric response. Various coupling effects in soft materials can influence the flexoelectric effect. For example, the electric-mechanical and thermal-mechanical coupling effects can enhance the flexoelectric response by modifying the charge distribution and strain state within the material [226]. These multidomain coupling effects result in complex flexoelectric responses exhibited by soft materials. The mechanism of flexoelectric effect in soft materials involves several aspects. Precise manipulation of the molecular structure, orientation, and coupling effects in soft materials enables the achievement of more efficient, flexible, and controllable flexoelectric responses, opening up new possibilities for applications in the field of soft electronics [227]. The measurement methods of flexoelectric response in soft materials include bending beam method, capacitance method, digital image correlation, scanning probe microscopy (Atomic force microscopy (AFM) or scanning tunneling microscopy (STM)) [218, 228].

By designing and synthesizing specific material structures, the flexoelectric effect can be enhanced [229]. Methods such as introducing non-centrosymmetric, modifying crystal structures, or controlling lattice distortions can increase the flexoelectric response of materials [230, 231]. This approach often involves engineered material design and synthesis to achieve higher flexoelectric coefficients. The flexoelectric effect can be enhanced at material interfaces or in thin films [232]. The unique properties of interfaces or thin film structures can lead to increased local strain gradients, thereby enhancing the flexoelectric effect [233]. Therefore, considering the utilization of interface or thin film structures can enhance the flexoelectric effect in material design. Nanostructures and nanoscale effects can significantly enhance the flexoelectric effect [214]. When materials exhibit special structures, morphologies, or size effects at the nanoscale, their flexoelectric coefficients may increase significantly. Strain gradients are more easily formed at the nanoscale, and the interaction with charge distribution is stronger, enhancing the flexoelectric effect. External fields such as electric fields, strains, or magnetic fields can modulate the flexoelectric effect. By applying appropriate external fields, it is possible to change the charge distribution and strain state within materials, thereby enhancing the flexoelectric response. This method can be controlled experimentally, providing a viable approach for manipulating the flexoelectric effect.

The flexoelectric effect has a wide range of potential applications. Here are some common application areas such as flexible electronic devices. The flexoelectric effect can be used to manufacture flexible electronic devices such as flexible sensors, touch screens, and wearable devices [234, 235]. By harnessing the flexoelectric response of soft materials, high sensitivity detection and response to mechanical deformations can be achieved, enabling more comfortable, wearable, and bendable electronic devices. The flexoelectric effect can be utilized for energy harvesting and conversion, converting mechanical energy into electrical energy [236]. For example, by integrating flexoelectric materials into flexible structures, flexural motion from the external environment can be used to collect energy and drive sensors, wireless communication modules, or other electronic devices. The flexoelectric effect allows soft materials to respond to external stimuli and achieve adaptive functionality. This capability can be used to manufacture smart materials and adaptive systems, such as self-adjusting optical elements, deformable surfaces, and shape memory materials. The flexoelectric response of soft materials enables controlled adjustments of shape, optics, or surface characteristics. In micro and nanoscale systems, the flexoelectric effect can be used to manipulate and regulate the shape and properties of micro and nanostructures. By introducing flexoelectric materials into micro and nanostructures, precise control and adjustment of micro and nanodevices can be achieved, offering new possibilities for the field of micro and nanoelectronics and nano mechanics. The flexoelectric effect also holds potential applications in the biomedical field. For example, flexible biosensors or implantable devices can be manufactured using the flexoelectric effect, enabling monitoring of physiological parameters or medical treatments with bendable characteristics. These are just some potential application areas of the flexoelectric effect. With further understanding of its underlying mechanisms and technological advancements, we can expect innovative developments and applications in various fields.

The unique mechanical and electrical properties of carbon nanostructures, making them potential candidates for flexoelectric applications. Carbon nanotubes have gained tremendous attractions since their discovery in 1993 [237]. The single-walled carbon nanotubes can be regarded as rolled-up graphene sheet. Due to its unique structure, the single-walled carbon nanotube has several excellent properties. It is known that single-walled carbon nanotubes can be metallic or semiconducting with different helicity of the graphitic rings and diameters [238]. The SWNTs also have unusual properties including good mechanical properties, high thermal conductivity, and unique chemical performance [239]. Recently, the presence and magnitude of flexoelectric effect in carbon nanostructures have been a subject of interest and research. Traian Dumitric studied the polarization of carbon nanotubes depending on the curvature [240]. When a graphite sheet is bent to form a carbon nanotube, it introduces an asymmetry in the overlap of p-orbitals. This causes the p-orbitals inside the cavity to come closer to the outer wings. Consequently, the Coulomb repulsion within the cavity increases with curvature, resulting in a redistribution (rehybridization) of the p-orbitals from the sp2 state of graphite to an intermediate state between sp2 and sp3. This redistribution leads to an electronic charge transfer from the concave to the convex region. By calculation, they gave the conclusion that the curvature of CNTs leads to a notable rehybridization of the p-orbitals, which can be quantified by the pyramidalization angle. This rehybridization causes the center of electronic charge at each atomic site to shift away from the nuclear charge. This phenomenon characterizes the distinctive piezoelectric properties of monoatomic graphene layers. Alexander G. Kvashnin theoretically studied the flexoelectric response in carbon nanostructures with sp2 structure [241]. Take graphene for example, due to the central symmetry center of the graphene lattice, a non-uniform mechanical distortion of graphene does not result in the induction of an electrical dipole, thereby lacking a piezoelectric effect. The situation is different for the flexoelectric effect. For the nonpolar 2-dimential structure with atomic monolayer, the electric polarization will result from the electric redistribution with the deformation of the symmetry. However, wrapped graphene sheet of carbon nanotubes, due to its cylindrical symmetry, the total dipole moment of CNT is zero. Meanwhile, it is expected that local dipole moments would emerge in a small portion of the CNT. Compared with CNT, the curvature structure based on graphene gains more interest because of their nonequivalent carbon atomic structure, such fullerenes. Vasilii I.

Artyukhov studied the flexoelectric response in carbon nanotubes [216]. By using the first-principles calculations, they investigated the significance of the flexoelectric volage, and its influence on electric distribution and optical properties. Based on their theoretical analysis, the flexoelectric effect will be boosted due to disrupting π-orbital symmetry by the curvature. At the time, they predicted that the flexoelectric voltage will be further enhanced by functionalization, such as absorbing polar materials. Finally, by DTF calculation, they confirmed their prediction that the remarkable flexoelectric voltage is real existed across the wall, although may be subtle for potential applications. In SWCNTs, the potential distribution in the outer region of the tube and the inner channel, except for a few of the thinnest tubes, exhibits distinctive uniform plateaus. This clearly demonstrates the cylindrical capacitor-like behavior of the tube wall. However, so far, research and predictions regarding the flexoelectric effect in carbon nanotubes have only been confirmed through theoretical calculations and there are no reported experimental findings to date.

This investigation proposes a paradigm to achieve energy harvesting from flexoelectricity. This microminiaturized flexoelectric is of external polarization by embedding the polar molecules into the carbon nanotube to form composite with engineered interface. Applied with technology of atomic force scanning, this polarization is demonstrated to cause the phase difference among the nanotubes. In this study, two chemically modified SWCNTs described in Feng Yang’ s work was used [242]. Specifically, semiconductor SWCNTs with diameters ranging from 1.0 nm to 1.5 nm were selected. Two types of polar molecules, namely spherical

$H_3PW_{12}O_{40}$ and elliptical $K_{12}H_2P_2W_{12}O_{48}$, were embedded within the SWCNTs. Based on the reported structures and DFT calculations of electron density interactions between the SWCNTs and the embedded polar molecules, it was observed that there is electron transfer from the tube walls to the embedded molecules in the structure of SWCNTs containing spherical $H_3PW_{12}O_{40}$. This finding is consistent with their hypothesis that the inclusion of an electron reservoir containing both anions and cations can modulate the π-π conjugation interaction on the outer wall of the carbon nanotubes, thereby altering the electronic state of the tube walls. Based on these computational results, this study suggests that this chemical modification approach also creates an effective interface for flexoelectricity. However, according to literature research, investigations into the flexoelectric effect of carbon nanotubes are currently limited to theoretical calculations. Therefore, experimentally verifying the construction of a flexoelectric interface through the incorporation of polarized molecules within non-planar carbon nanotubes and understanding its underlying principles would be a highly meaningful endeavor.

5.2 Instruments and characterization

The flexoelectric effect in modified non-polarized carbon nanotubes was investigated. This was primarily achieved by applying point forces, line forces, and surface forces on the surface of the modified carbon nanotubes to induce localized asymmetric strain distribution and induce charge density migration, resulting in polarization and capturing polarized electrical signals. First, the samples were prepared on silicon substrates and characterized using field emission scanning electron microscopy (Figure 5.3). The point forces and line forces were applied using a circular AFM probe (Cypher S/Oxford Instruments Asylum Research) (Figure 5.1), which caused localized non-uniform strain and broke the local center symmetry at the probe-surface contact. The DC electrical transport properties of the carbon nanotubes after intrinsic polarization under nanoscale indentation were characterized using a conductive AFM measurement system. Next, the polarization-induced properties of the chemically modified carbon nanotubes under point force mode were investigated using the piezo response（PMF） and capacitance(SCM) modes of atomic force microscopy to validate the reliability of the strategy for constructing an enhanced flexoelectric effect interface through chemical means. The micro-mechanical properties of the chemically modified carbon nanotubes were also evaluated using the mechanical mode of AFM. The study of the surface force-induced flexoelectric effect was realized using Keysight B1500A combined with a probe system (Figure 5.2). By varying the internal pressure of the chamber, isotropic out-of-plane pressure was applied to the chemically modified carbon nanotubes to induce an out-of-plane strain gradient and break the center symmetry, while capturing the current response. The molecular vibrations of the chemically modified carbon nanotubes were characterized using the Horiba/LabRam HR Evolution system (Figure 5.4).

Figure 5.1 Cypher S/Oxford Instruments Asylum Research

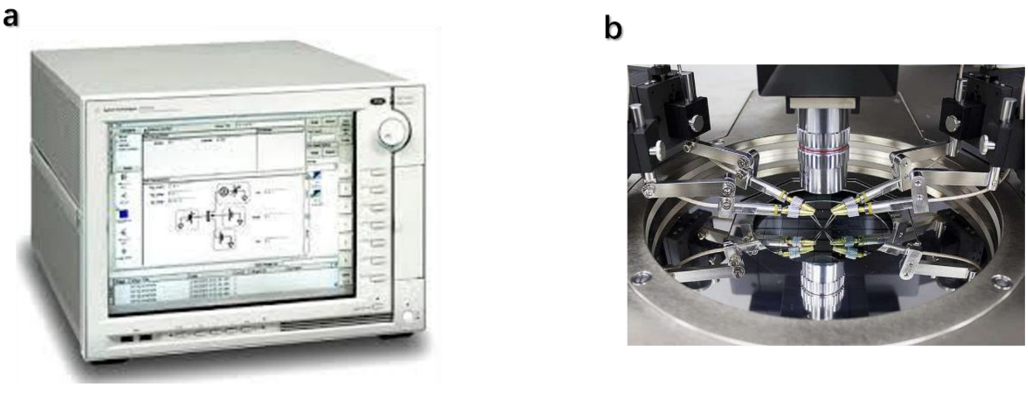

Figure 5.2 Keysight B1500A (a), MPI TS3000 probing system(b)

Figure 5.3 HRSEM ZEISS Gemini 300

Figure 5.4 Horiba/LabRam HR Evolution

5.3 Results and discussion

5.3.1 Tip nano-indentation in point touch mode

The flexoelectric characteristics of SWCNTs with two types of embedded polarizable molecules were studied by using AFM under modes of nanoindentation. Initially, tip-nanoindentation tests were performed on unmodified carbon nanotubes (Figure 5.5). A conductive probe of HQ:NSC18/pt, with a platinum-coated surface and a radius less than 8 nm, was used. The probe had a force constant of 2.8 N/m, and the current measurements were conducted with ORCA module with a range of 20 nA. The morphology and electrical signals of the carbon nanotubes were captured by scanning in the height retrace and electric retrace modes, respectively, as shown in Figure 5.6 (a), (b). Then, different forces were applied by pressing the probe, and the I-V curves under nanoindentation were measured while applying a bias voltage through the substrate. The AFM tip was brought into contact with the surface of the SWCNTs, and a preset force was applied by the tip. Once the preset force reached its maximum and stabilized, a set voltage bias was applied to the tip for I-V scanning. The preset force can be calculated and set using the inverse optical lever sensitivity (InvOLS) and the probe's spring constant (force = spring constant × InvOLS × (preset deflection – initial deflection)).

For the pristine SWCNTs, I-V curves under point indentation revealed minimal changes when vertical stresses of 1/5/10/100/150/200/250 n N were applied to the nanotube walls by the probe. However, the induced current linearly increased with increasing bias voltage (Figure 5.6(c)). These results indicated that the charge transfer between the probe and the surface of the unmodified carbon nanotubes remained relatively unchanged with applied surface strain. Under a bias voltage setting of 2 V, the measured current for different preset forces was less than 1 nA and increased with increasing bias voltage. The I-V curves exhibited a weak asymmetric trend for positive and negative bias voltages. In the case of modified carbon nanotubes with polarizable molecules PW12@SWCNTs and P2W12@SWCNTs, the behavior was significantly different. For the spherical-structured polarizable molecule-modified carbon nanotubes (PW12@SWCNTs), the selected test regions in Figure 5.7 (a) and (b) showed that the current became more sensitive, and the V-I slope increased with increasing preset force and applied strain. Similar to the unmodified nanotubes, the current response exhibited a weak asymmetric trend for positive and negative bias voltages, increasing with increasing bias voltage. At a bias voltage of 2 V and a preset force of 200 nN, the detected current approached 5 nA (Figure 5.7 (c)). For the elliptical-structured polarizable molecule-modified carbon nanotubes (P2W12@SWCNTs), the selected test regions in Figure 5.8 (a) and (b) also exhibited increased sensitivity in current response and an increasing V-I slope with increasing preset force and applied strain. However, the current response showed an obvious asymmetrical trend for positive and negative bias voltages. In both positive and negative regions, the current response increased with increasing bias voltage. At a bias voltage of 2 mV and a preset force of 200 nN, the detected positive current approached 7.5 nA (Figure 5.8 (c)), while the negative current approached 5 nA.

Based on the I-V test results obtained from the point-indentation mode, a preliminary conclusion can be drawn. In pristine SWCNTs, it was observed that indentation signals could be detected. However, the electrical signals induced by indentation did not vary with the applied strain, which is consistent with the theoretical findings in the literature. It is known that in curved graphene structures such as carbon nanotubes, there can be a strain gradient-electrostatic polarization coupling in localized regions. However, the flexoelectric effect in these localized regions is not prominent. Furthermore, through chemical modification, by introducing polarizable molecules onto the surface of carbon nanotubes, it is possible to alter the π-π conjugation of the tube surface, thereby modifying the electron density distribution. This modification enhances the surface polarization, leading to an increased flexoelectric effect on the tube surface, as observed in the experimental results. Moreover, the flexoelectric effect is more pronounced in SWCNTs with embedded elliptical-structured polarizable molecules compared to SWCNTs with embedded spherical-structured polarizable molecules. In other words, electrical signals can be captured at a microvolt-level bias voltage. This is attributed to the additional structural asymmetry introduced by the elliptical structure of the polarizable molecules in the modified carbon nanotubes.

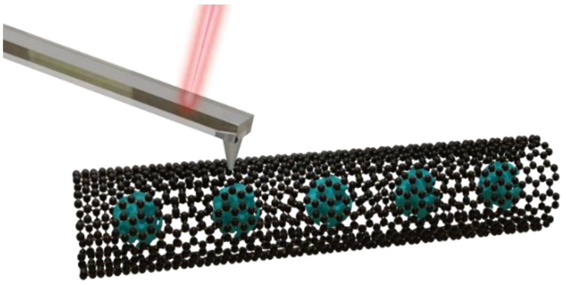

Figure 5.5 The schematic illustration of the experimental configuration involving AFM probe

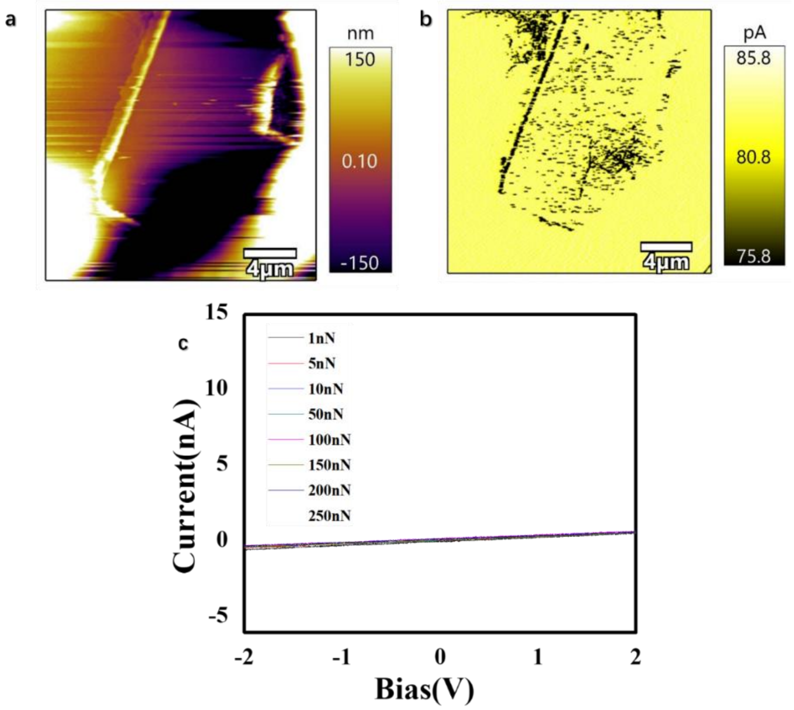

Figure 5.6 The AFM topography of single-walled carbon nanotubes in Orca mode: Height retraces(a), and Current retrace(b) and characteristics of tip point nano-indentation triggered flexoelectric effect (Current @varied applied force VS Bias)

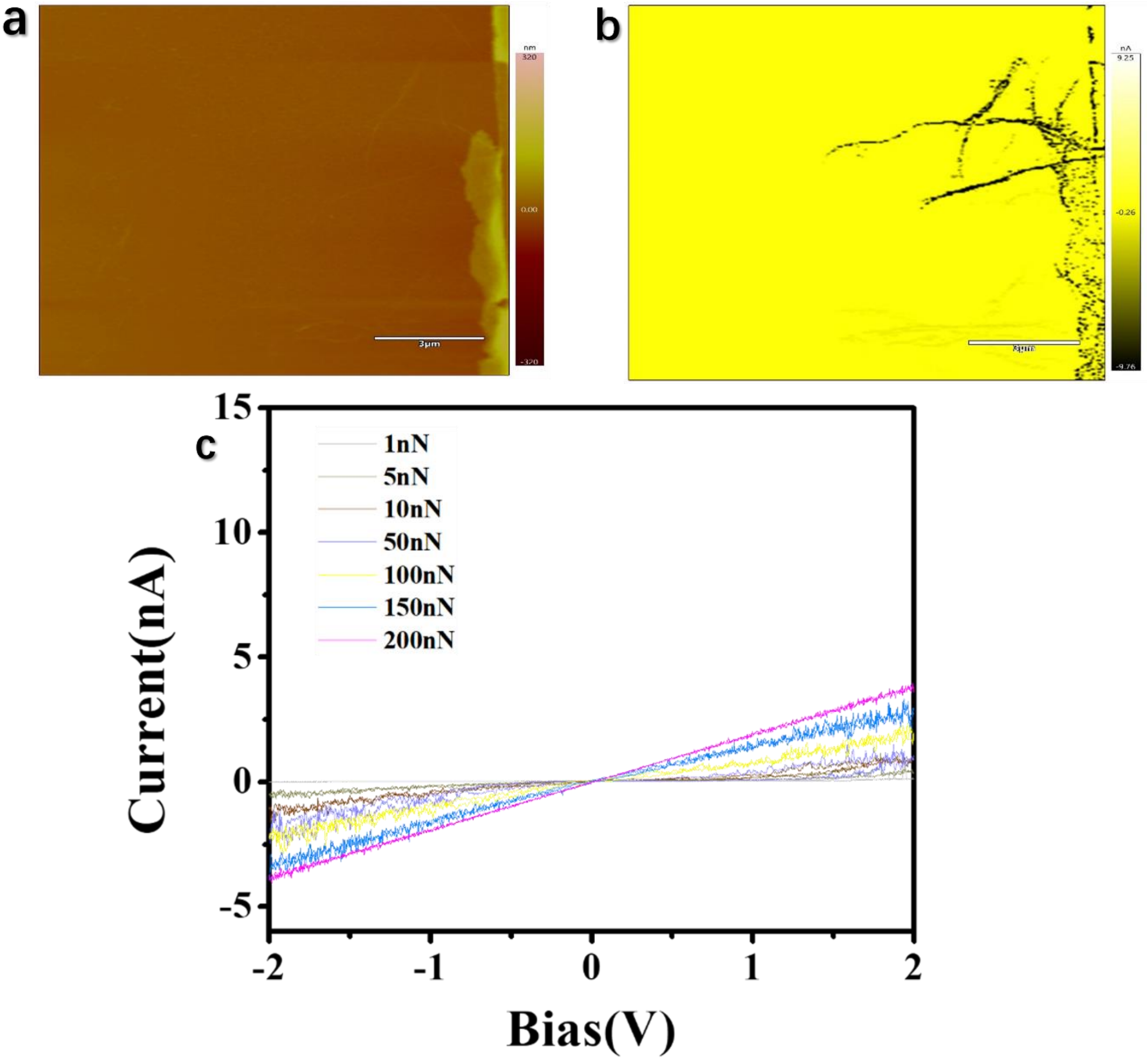

Figure 5.7 The AFM topography of PW12@SWCNTs in Orca mode: Height retrace (a) and Current retrace(b) and characteristics of tip point nano-indentation triggered flexoelectric effect (Current @varied applied force VS Bias)

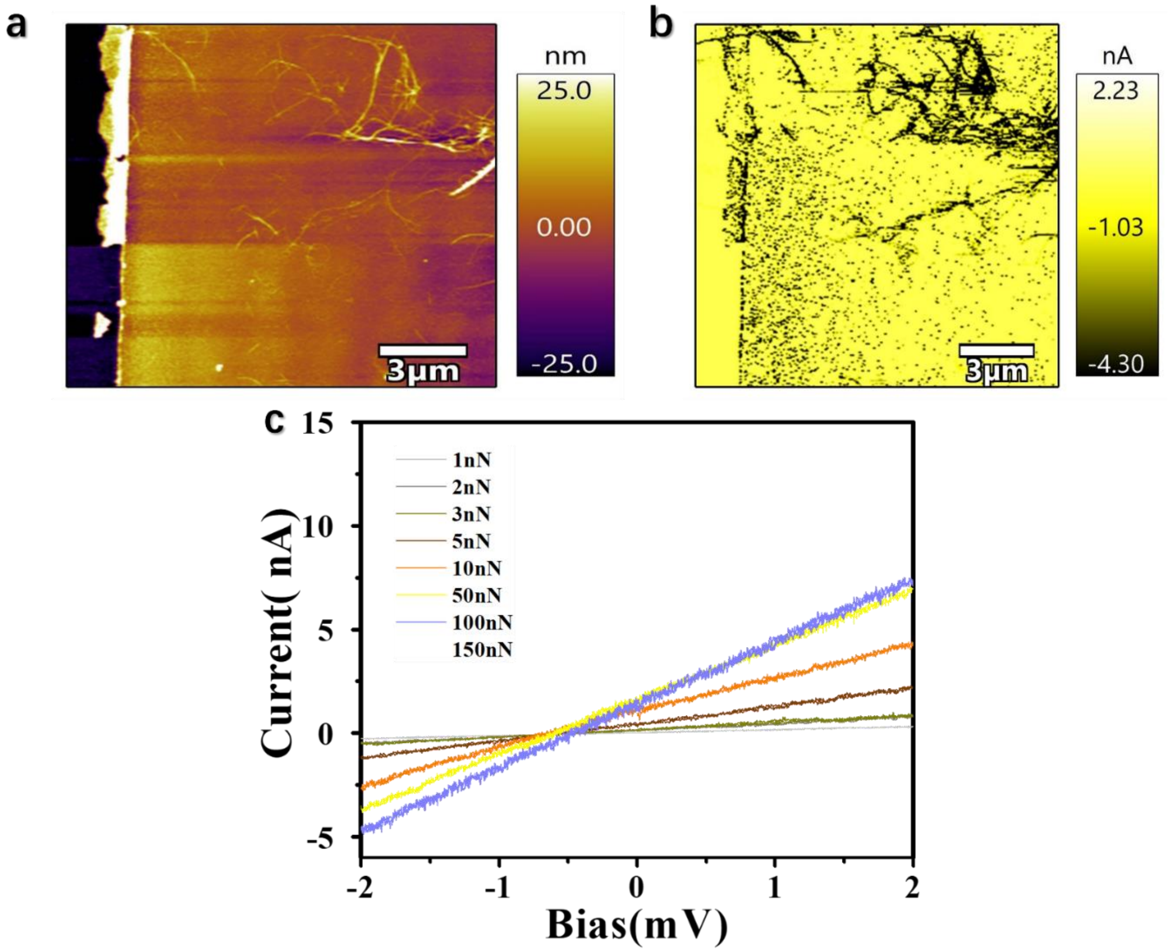

Figure 5.8 The AFM topography of P2W12@SWCNTs in Orca mode: Height retrace(a) and Current retrace(b) and characteristics of tip point nano-indentation triggered flexoelectric effect (Current @varied applied force VS Bias)

5.3.2 Line-force tip-nanoindentation

Using the AFM Orca module in line-force mode, further investigation was conducted on the flexoelectric properties of modified carbon nanotubes to study the flexoelectric effect at the modified interface. In the preliminary findings using point-force mode, it was observed that point-tip nanoindentation on the polarized molecularly modified SWCNT surface could detect local flexoelectric effects. In the typical contact mode force curve, the probe moves downwards until it reaches the set threshold force (trigger point), after which the probe reverses its direction and moves upwards, detaching from the sample. In this scenario, the probe undergoes a certain distance of sliding on the surface of the test object during the application and release of stress, enabling the measurement of force-electric response on a specific region of the carbon nanotube surface.

Based on this, in the line-force testing of unmodified carbon nanotubes, trigger points were set at 1/10/50 nN, and the probe sliding distance was set to 200 nm. However, no significant electrical signal was detected during the application of stress as the probe slid on the surface (Figure 5.9 (a) (b) (c)). In the case of polarized molecularly modified carbon nanotubes with a spherical structure (PW12@SWCNTs), trigger points were set at 1/20/40 nN, and the probe sliding distance was set to 200 nm. In this case, a noticeable electrical signal was detected during the application of stress as the probe slid on the surface (Figure 5.10 (a) (b) (c)), with current levels in the pA range. It can be observed from the graph that as the applied stress increases after probe contact, the corresponding current also increases, reaching its maximum at the respective threshold force. When the threshold forces reached 1/20/40 nN, the corresponding currents detected were 6 pA, 185 pA, and 345 pA, respectively. For polarized molecularly modified carbon nanotubes with an elliptical structure (P2W12@SWCNTs), trigger points were set at 1/20/40 nN, and the probe sliding distance was set to 200 nm. Similar to the spherical structure, a noticeable electrical signal was detected during the application of stress as the probe slid on the surface (Figure 5.11 (a) (b) (c)), with current levels in the nA range. When the threshold forces reached 1/20/40 nN, the corresponding currents detected were 1 nA, 11 nA, and 18 nA, respectively.

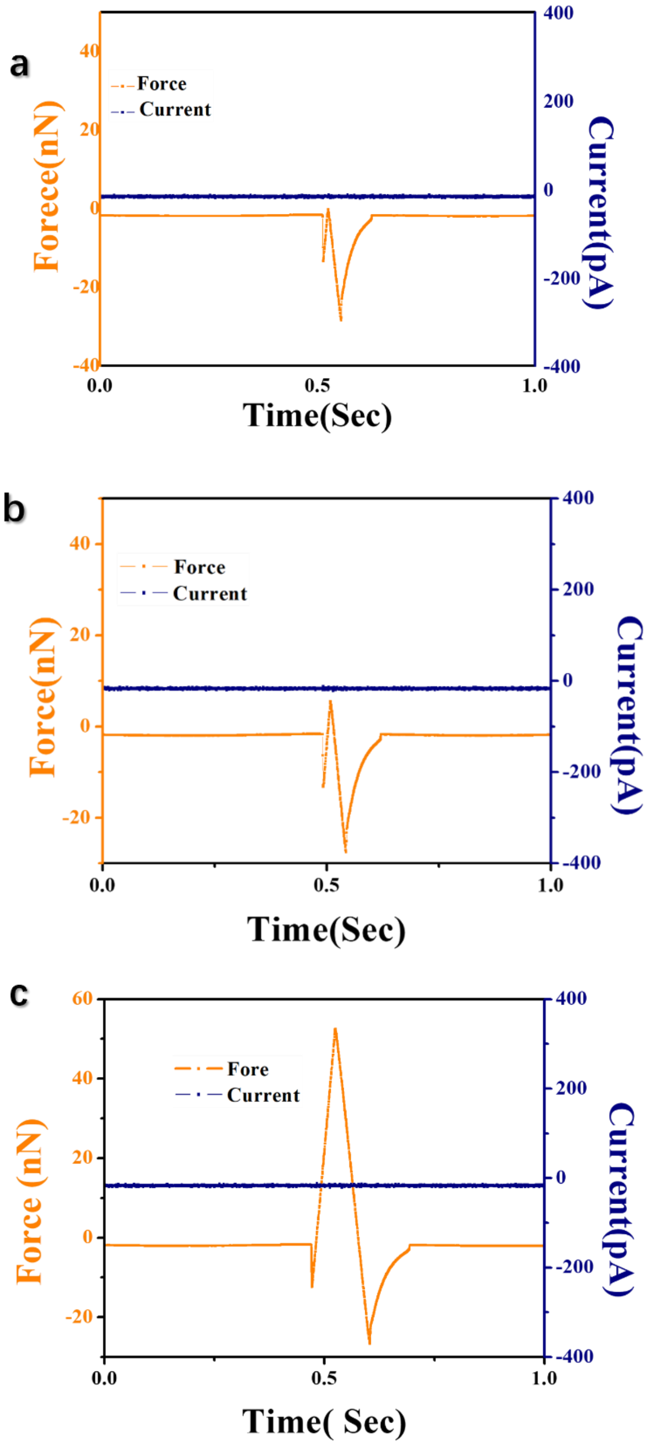

Figure 5.9 Characteristics of tip line nano-indentation triggered flexoelectric effect of SWCNTs: under trigger setpoint of 1nN (a), 10nN(b), 50nN(c)

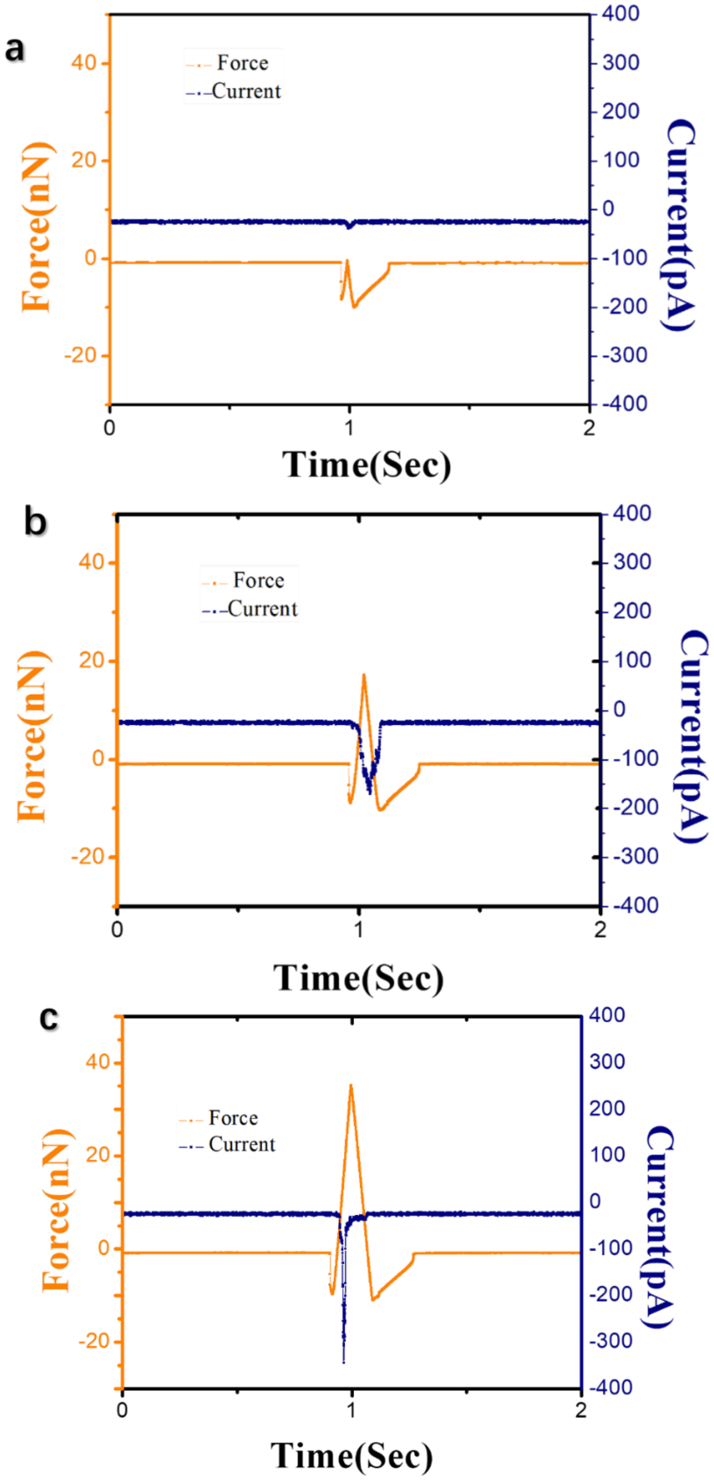

Figure 5.10 Characteristics of tip line nano-indentation triggered flexoelectric effect of PW12@SWCNTs: under trigger setpoint of 1nN (a), 20nN(b), 40nN(c)

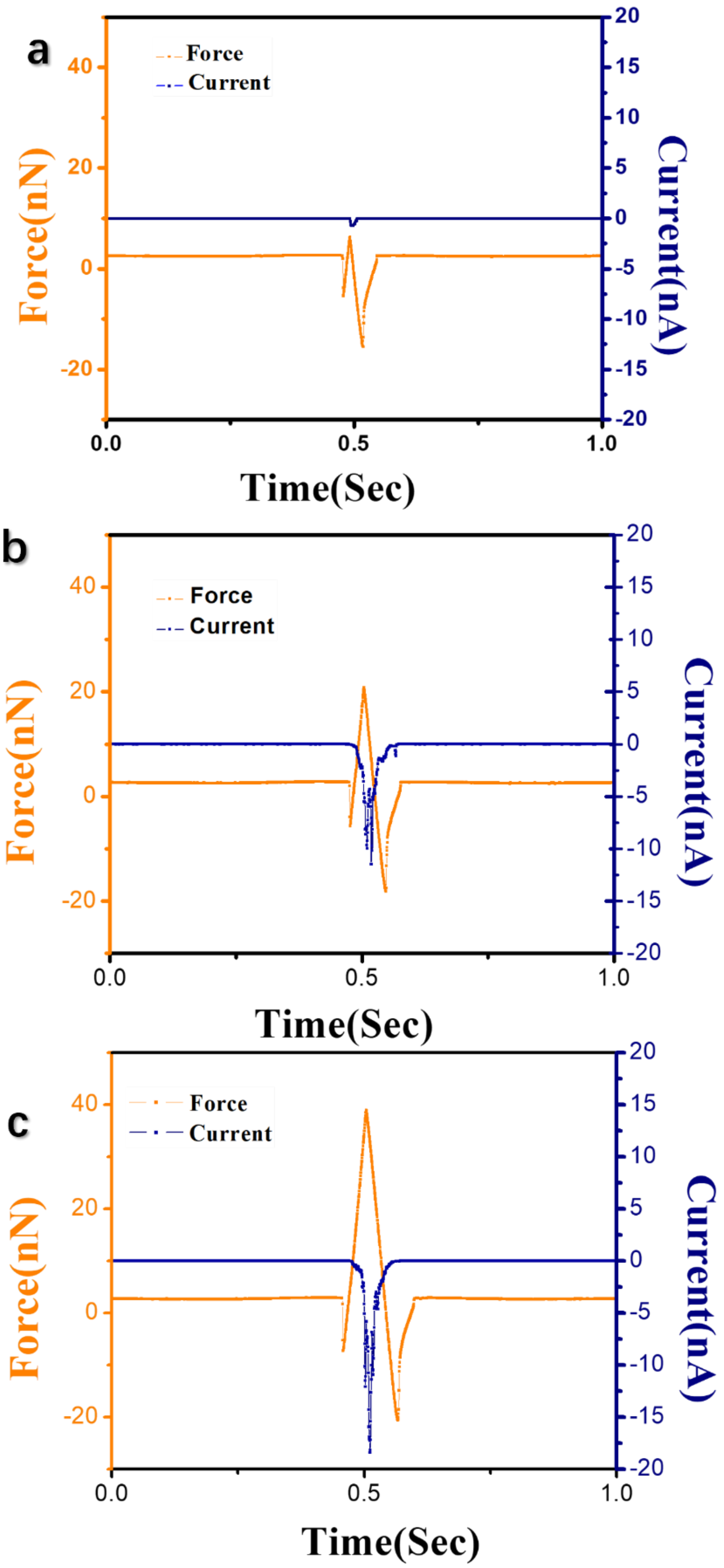

Figure 5.11 Characteristics of tip line nano-indentation triggered flexoelectric effect of P2W12@SWCNTs: under trigger setpoint of 1nN (a), 20nN(b), 40nN(c)

5.3 PFM probing results

PFM (Piezoresponse Force Microscopy) is a typical scanning probe technique used for qualitative and quantitative analysis of the piezoelectric effects in materials. It enables the characterization of the electric-mechanical coupling and piezoelectric coefficients through PFM image analysis. Similarly, in PFM images, the amplitude image provides information about the variations in piezoelectric performance and domain structures of the material. The phase image reveals the phase variations associated with the piezoelectric effects and is utilized to study the polarization direction in electric-mechanical coupling. Therefore, by analyzing the PFM images, combining the amplitude and phase images, it is possible to detect the presence of polarization reversal in the material. Additionally, PFM imaging can be used to observe polarization phenomena induced by flexoelectric coupling.

For pristine single-walled carbon nanotubes (SWCNTs), using PFM's height retrace (Figure 5.12(a)) and Z-sensor retrace techniques (Figure 5.12(b)), it is possible to locate individual regions of SWCNTs. However, in the phase images (Figure 5.12(c), Figure 5.12(d)) and amplitude (Figure 5.12(e), Figure 5.12(f)) obtained from both the left and right channels, no polarization interface was observed. In the case of polarized molecularly modified spherical SWCNTs (PW12@SWCNTs), by employing PFM's height retrace (Figure 5.13(a)) and Z-sensor retrace techniques (Figure 5.13(b)), it is possible to locate individual regions of spherical SWCNTs. By examining the phase images (Figure 5.13(c), Figure 5.13(d)) and (Figure 5.13(e),

Figure 5.13(f)) amplitude from both the left and right channels, almost symmetric interface effects were observed on the SWCNT walls, accompanied by phase variations at the interfaces, indicating the presence of polarization reversal on the tube walls. From Figure 5.13(g), it can be observed that there is a distinct pole domain wall-like structure on the PW12@SWCNTS tube wall.

Similarly, for polarized molecularly modified elliptical SWCNTs (P2W12@SWCNTs), using PFM's height retrace (Figure 5.14(a)) and Z-sensor retrace (Figure 5.14(b)) techniques, it is possible to locate individual regions of elliptical SWCNTs. By examining the amplitude (Figure 5.14(e), Figure 5.14(f)) and phase images (Figure 5.14(c), Figure 5.14(d)) from both the left and right channels, completely asymmetric interface effects were observed on the SWCNT walls, along with phase variations at the interfaces, indicating polarization reversal on the tube walls. According to Figure 5.14(g), distinct pole domain wall-like structure can also be observed on the P2W12@SWCNTS tube wall.

The analysis of PFM images has confirmed and demonstrated that introducing polarized molecules on the surface of carbon nanotubes can modify the π-π conjugation on the tube surface combined with chemical methods, leading to changes in the electron density distribution. This redistribution of electron density alters the local electronic properties of the carbon nanotubes, making it easier to disrupt the interaction between the tube wall and polarized molecules when subjected to external strain gradients, thus inducing polarization and enhancing the flexoelectric effect.

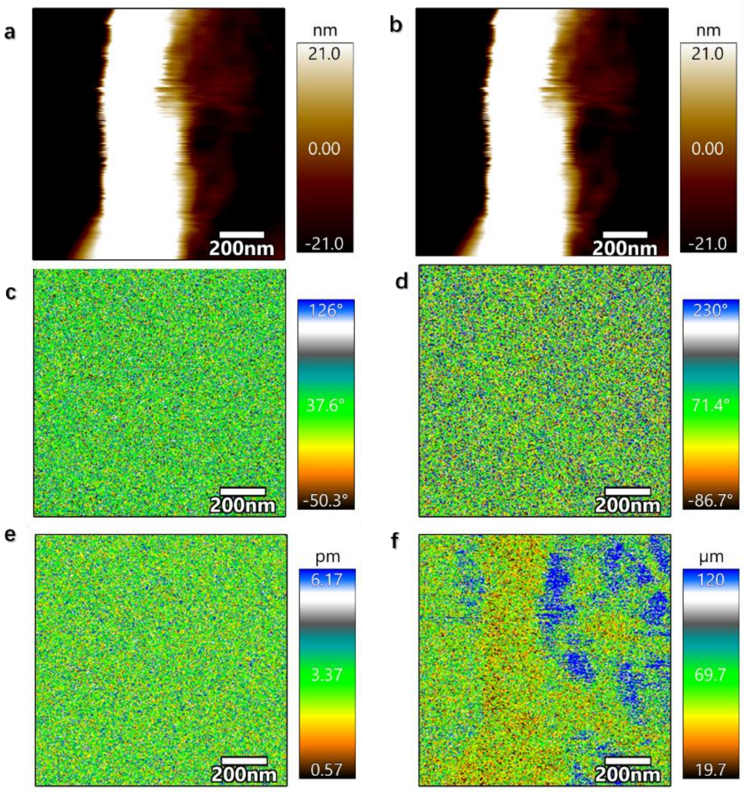

Figure 5.12 PFM Probing of SWCNTs: height retrace (a) and Z-sensor retrace(b), and phase L-Retrace(c), phase R-Retrace(d), amplitude-L (e), amplitude-R (f)

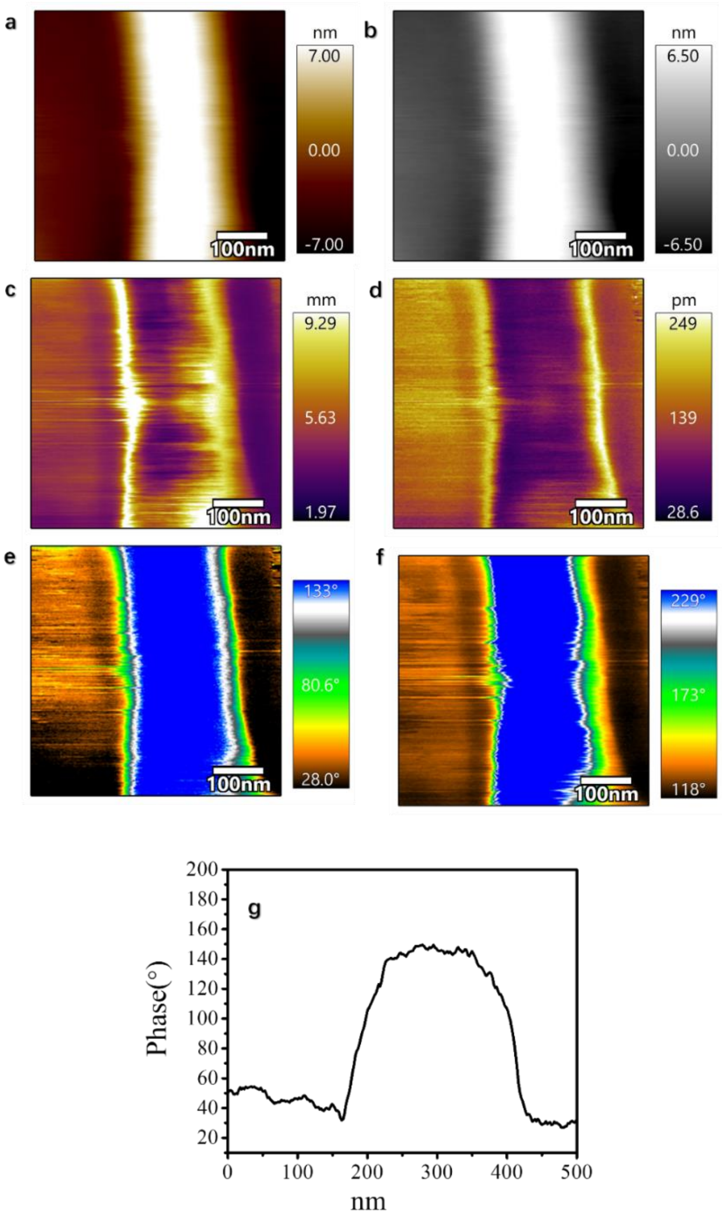

Figure 5.13 PFM Probing of P2W12@SWCNTs：height retrace (a) and Z-sensor retrace(b), and amplitude-L (c), amplitude-R(d), phase L-Retrace(e), phase R-Retrace(f), phase across the radial direction (g)

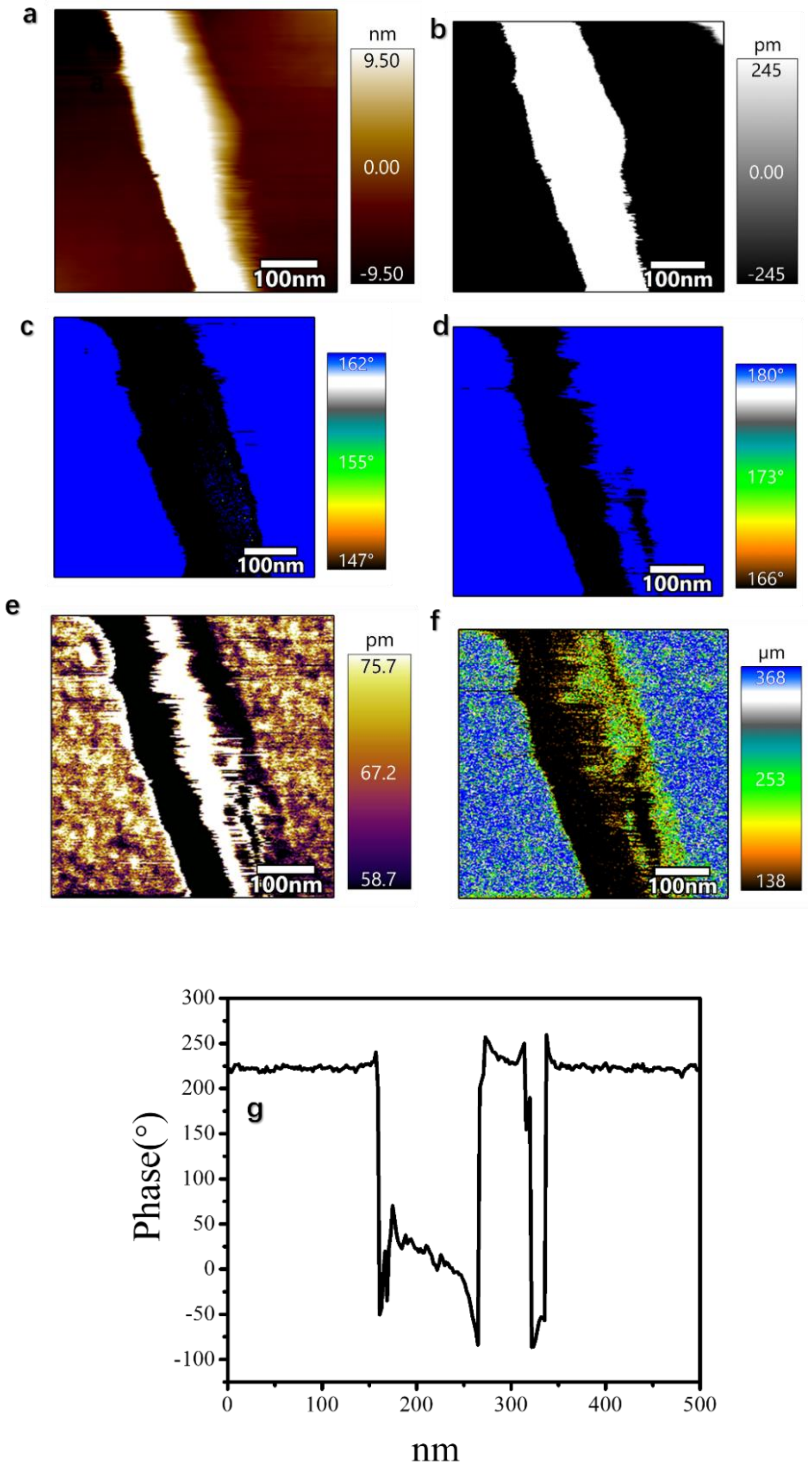

Figure 5.14 PFM Probing of P2W12@SWCNTs: height retrace (a), and Z-sensor retrace(b), and phase L-Retrace(c), phase R-Retrace(d), amplitude-L (e), amplitude-R (f), phase across the radial direction (g)

5.4 SCM probing results

The SCM (Scanning Capacitance Microscopy) probe technique in AFM can be utilized to measure the capacitance properties and electron distribution of semiconductor materials. It provides information about the electron concentration, carrier distribution, and capacitance changes on the material's surface. The principle of this testing method involves bringing the probe close to the material's surface and applying an alternating voltage to measure the capacitance between the electrode and the material. This capacitance measurement can be used to study properties such as the electronic density of states, carrier concentration, and charge distribution in the material. By continuously changing the voltage and position during the scanning process, capacitance images of the material's surface can be obtained, providing information about electron distribution and capacitance variations. Specifically, in the case of semiconductors, the amplitude image of SCM indicates the density of carriers, while the phase image of SCM indicates the type of carriers. The research focuses on the chemical modification of carbon nanotubes with polarizable molecules to create an effective interface that enhances the flexoelectric effect. The concept is based on the idea that the structure of polar molecules attached to the inner wall of carbon nanotubes affects their local electrical properties through π-π conjugation. The enhanced flexoelectric effect is induced by strain gradient and behaves like a capacitor. Based on the hypothesis that the structural mismatch between the polar molecules and carbon nanotubes, along with the interaction between them, will induce an enhanced flexoelectric effect under external stress and asymmetric strain at the interface, it is predicted that there will be changes in the capacitive properties on the surface of carbon nanotubes.

In the SCM probing results, for unmodified single-walled carbon nanotubes (SWCNTs), it can be observed from the SCM probing images (Figure 5.15 and Figure 5.16) of height, deflection, and Z sensor that no electrical signal related to capacitance characteristics is detected in amplitude, phase, or capacitance. This indicates that unmodified carbon nanotubes do not exhibit any capacitance properties, as no phase difference or capacitance characteristics are observed on the carbon nanotube surface. However, for the spherical polarized molecule-modified carbon nanotubes (PW12@SWCNTs), it can be observed from the SCM probing images of height (Figure 5.17(a)), deflection (Figure 5.17(b)), and Z sensor (Figure 5.17(c)) that electrical signals related to capacitance are detected in amplitude(Figure 5.18(d)), phase(Figure 5.17(e)), and capacitance(Figure 5.17(f)), This indicates the presence of capacitance characteristics in the modified carbon nanotubes under probe pressure. From the phase image across the radial direction (Figure 5.17(g), it can be seen that there is a polarity reversal on the carbon nanotube walls. Similarly, for the elliptical polarized molecule-modified carbon nanotubes (P2W12@SWCNTs), it can be observed from the SCM probing images of height (Figure 5.18(a)), deflection (Figure 5.18(b)), and Z sensor (Figure 5.18(c)) that electrical signals related to capacitance are detected in amplitude (Figure 5.18(d)), phase (Figure 5.18(e)), and capacitance (Figure 5.18(f)). This indicates the presence of capacitance characteristics in the modified carbon nanotubes under probe pressure. From the phase image, it (Figure

5.18(g) can be seen that there is a polarity reversal on the carbon nanotube walls. Additionally, when combined with the C-V curve (Figure 5.19), it can be observed that the capacitance of unmodified carbon nanotubes does not change with voltage. However, for the spherical polarized molecule-modified carbon nanotubes (PW12@SWCNTs) and elliptical polarized molecule-modified carbon nanotubes (P2W12@SWCNTs), the trend of capacitance variation resembles that of a "pseudo" P-type doped semiconductor curve.

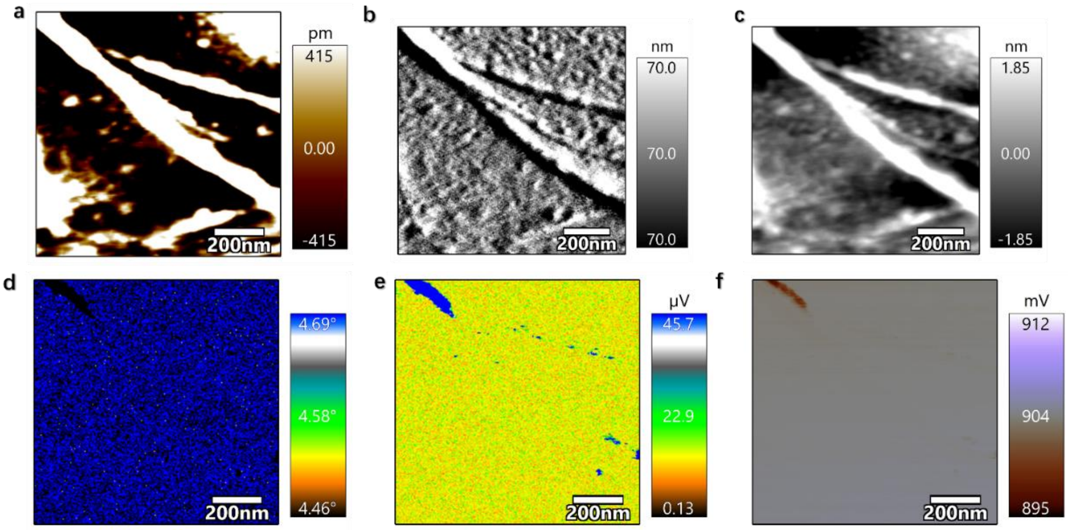

Figure 5.15 SCM probing of SWCNTs: Height retrace (a), Deflection retrace(b), Z-sensors retrace(c), phase retrace (d), amplitude retrace (e), capacitance (f)

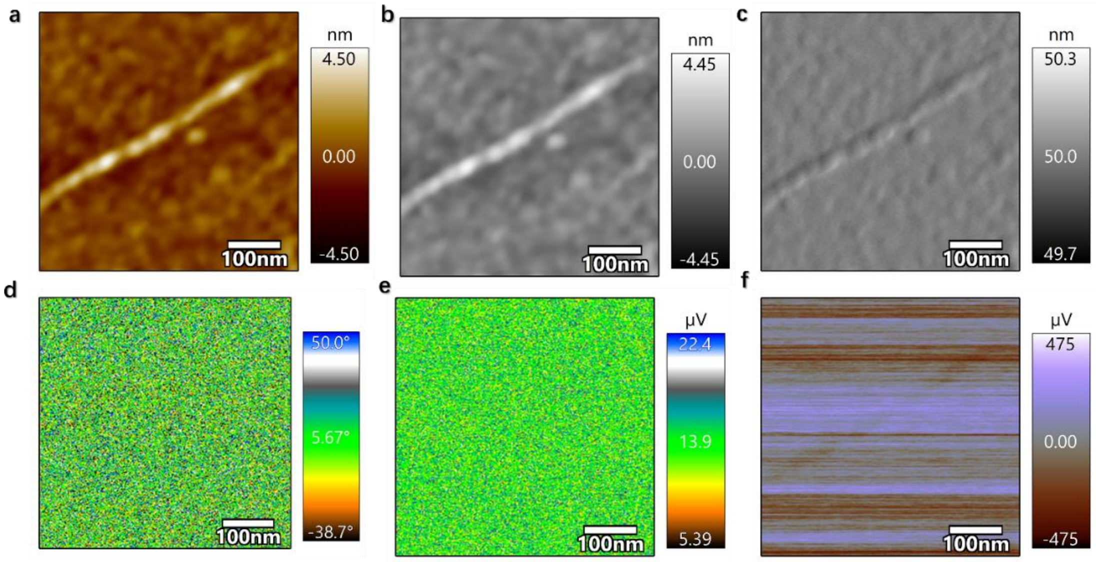

Figure 5.16 SCM probing of SWCNTs: Height retrace (a), Deflection retrace(b), Z-sensors retrace(c), phase retrace (d), amplitude retrace (e), capacitance (f)

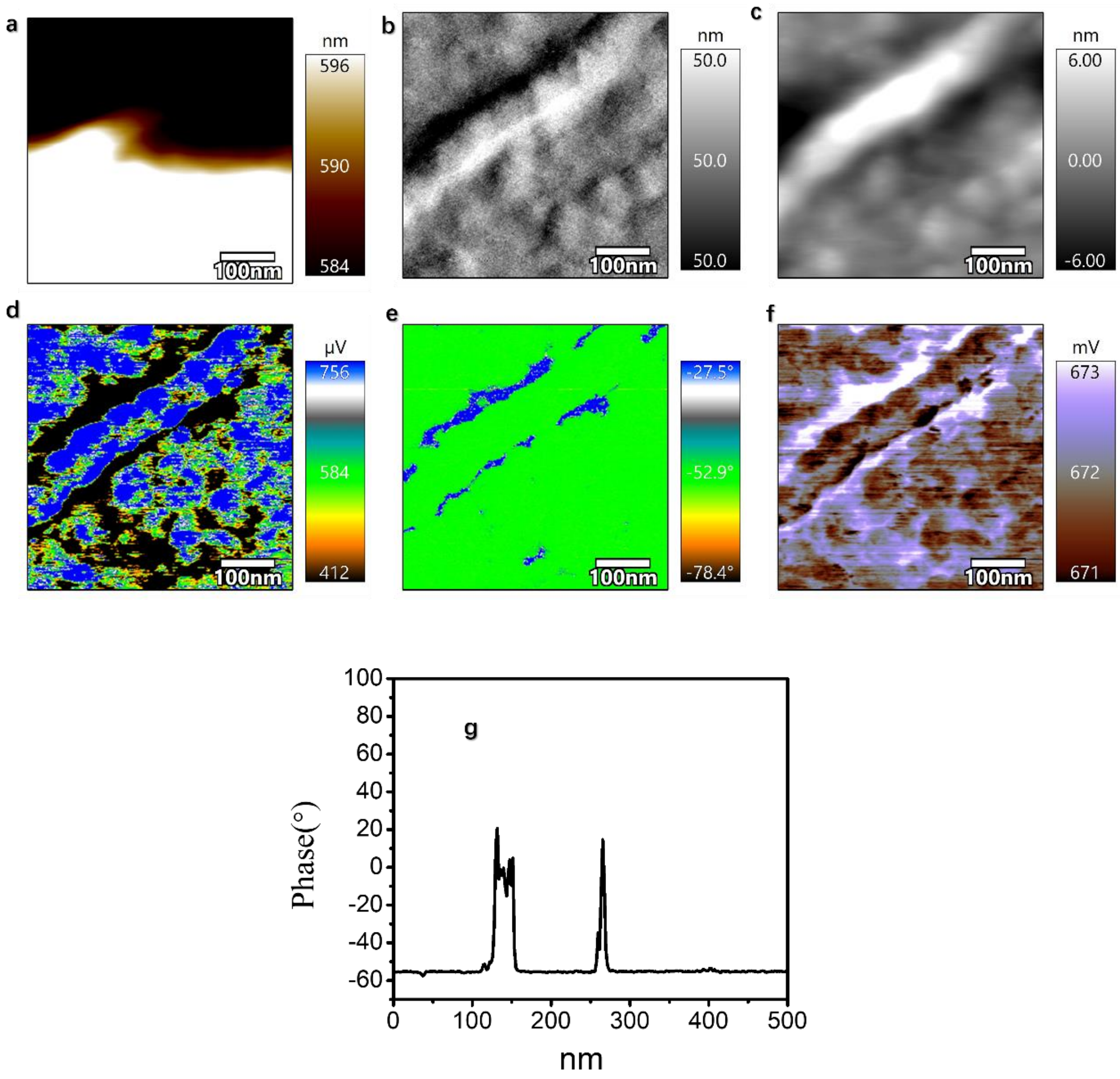

Figure 5.17 SCM probing of PW12@ SWCNTs: Height retrace (a), Deflection retrace(b), Z-sensors retrace(c), phase retrace (d), amplitude retrace (e), capacitance (f), Phase across the radial direction(g)

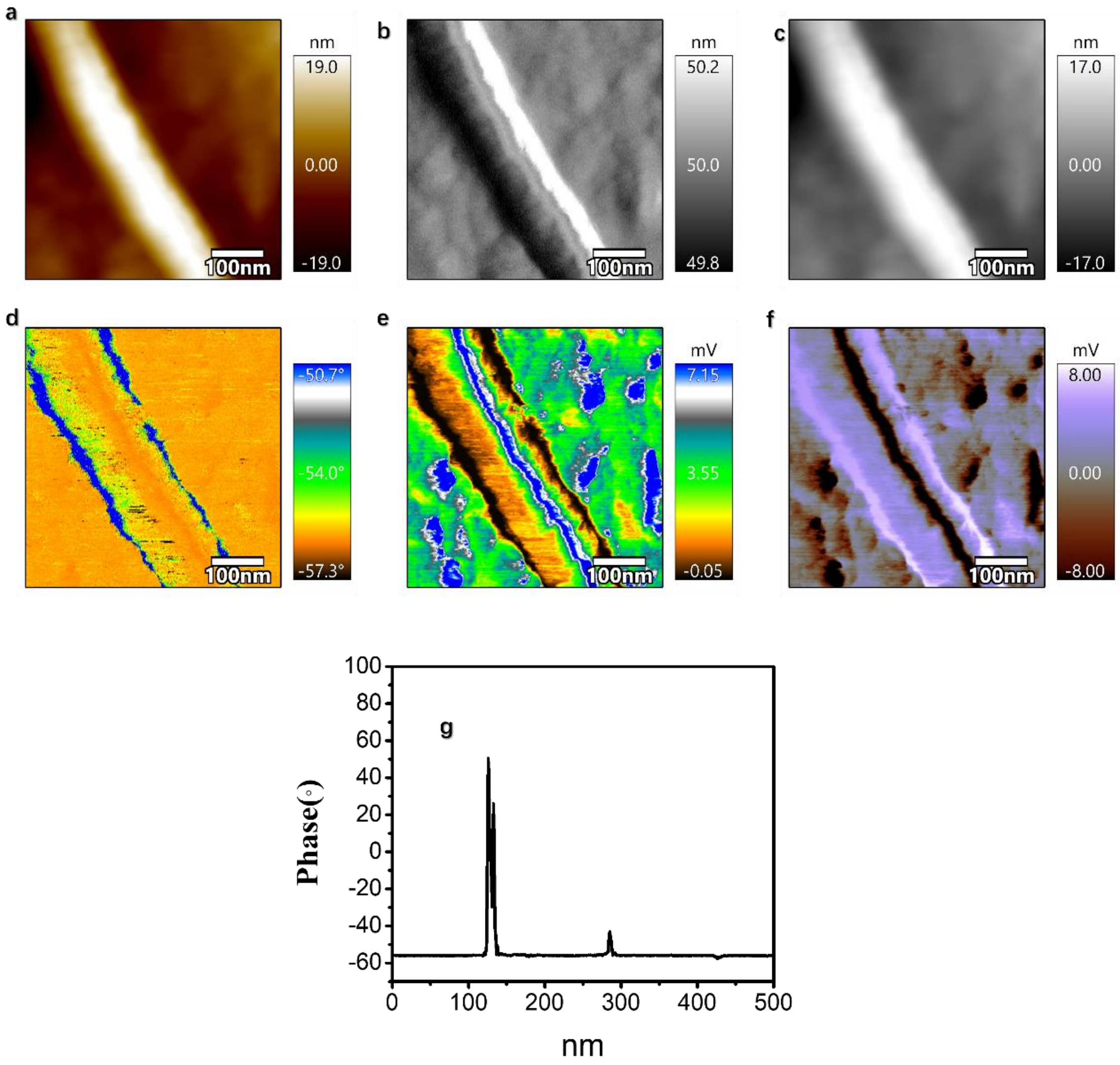

Figure 5.18 SCM probing of P2W12@ SWCNTs: Height retrace (a), Deflection retrace(b), Z-sensors retrace(c), phase retrace (d), amplitude retrace (e), capacitance (f), Phase across the radial direction(g)

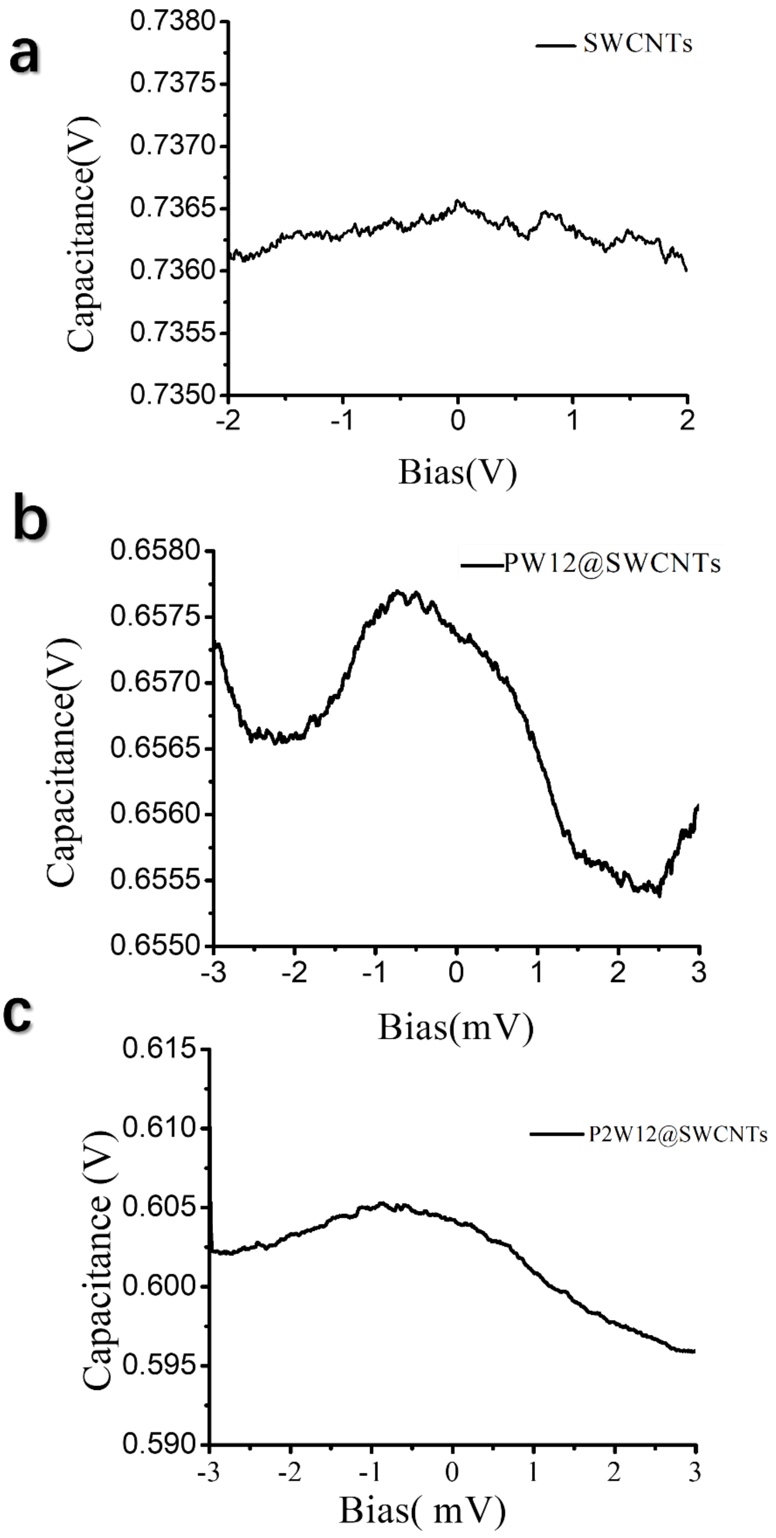

Figure 5.19 C-V curves: SWCNTs(a), PW12@SWCNTs(b), P2W12@SWCNTs(c)

5.5 AMFM probing results

Due to the direct contact of the AFM probe with the surface of the tested material, it is an ideal tool for measuring the mechanical properties of low-dimensional materials such as carbon nanotubes. The AM-FM viscoelasticity imaging technique of AFM allows for the quantitative derivation of energy dissipation and stiffness of carbon nanotubes in the nano scale. Regarding the flexoelectric effect, strategies for enhancing the effect can be divided into two parts: modulation of the local electric field, such as doping or creating structural defects, and strain engineering from external sources. Strain engineering for modulation involves constructing mechanical interfaces, creating heterogeneous junction structures, applying epitaxial strain, or mechanically pre-straining the material. These methods encompass controlling the material through its structure, composition, and formation, ultimately aiming to facilitate or increase the flexoelectric effect through strain gradients and mechanical means.

Based on previous electrical tests, it has been observed that the strategy of incorporating polar molecules within single-walled carbon nanotubes can alter the local electron density distribution on the nanotube walls, thereby promoting dipole moments. From one perspective, it is speculated that the strategy of incorporating polar molecules can create a mechanically unbalanced interface. This hypothetical assumption is based on the notion that the mechanical properties of the nanotube walls would be changed due to the mismatch with the incorporated polar molecules, and the viscoelastic characteristics of the tube-wall interface would promote the generation of strain gradients, thus enhancing the flexoelectric effect. Based on this, we conducted tests on both modified and unmodified single-walled carbon nanotubes' nanomechanical properties.

For unmodified single-walled carbon nanotubes, using the AM-FM module of AFM, we first identified the material region (Figure 5.20) and focused on a single carbon nanotube (Figure 5.21). By scanning across the nanotube and drawing a line, we were able to quantitatively obtain variations in the nanotube's Young's modulus and loss factor. The test results (Figure 5.21(d)) showed that the unmodified carbon nanotubes had a Young's modulus of approximately 3 GPa, and the radial distribution trend of the Young's modulus remained unchanged. The measured loss tangent (Figure 5.21(e)) ranged from 0.16 to 0.18, with no significant radial variation.

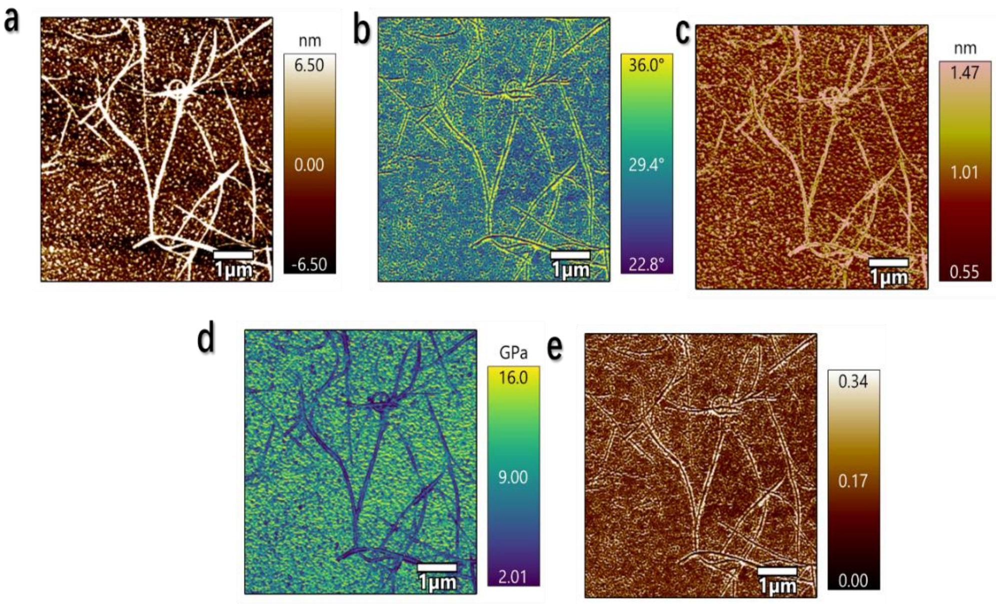

Figure 5.20 AMFM probing of SWCNTs: Height retrace (a), phase(b), Indentation (c), Young's Modulus(d), Loss tangent(e)

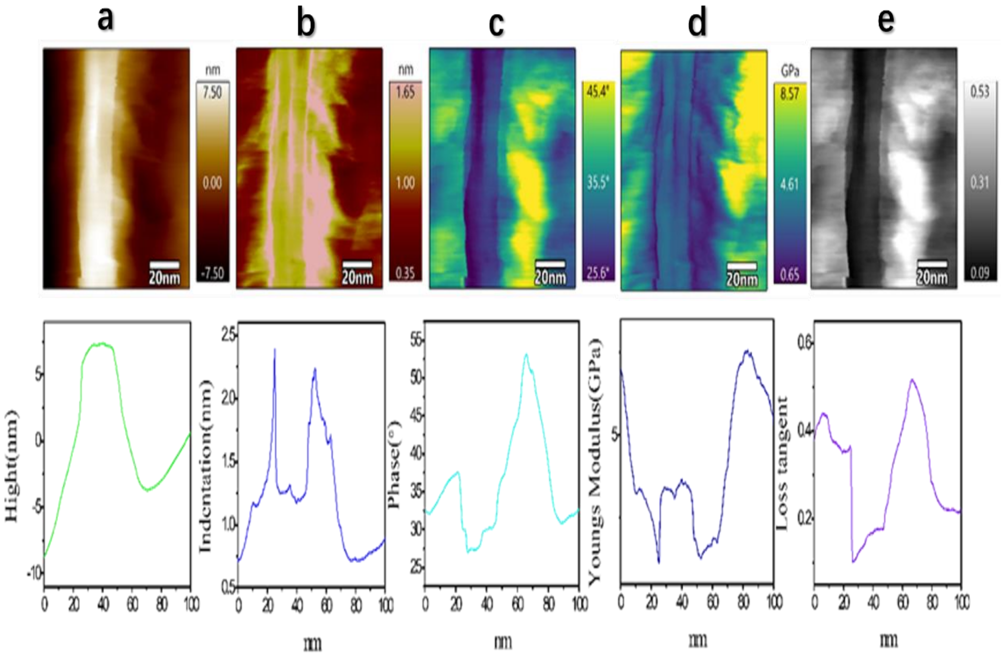

Figure 5.21 AMFM probing of SWCNTs: Height retrace (a), Indentation (b), phase(c), Young’s Modulus(d), Loss tangent(e)

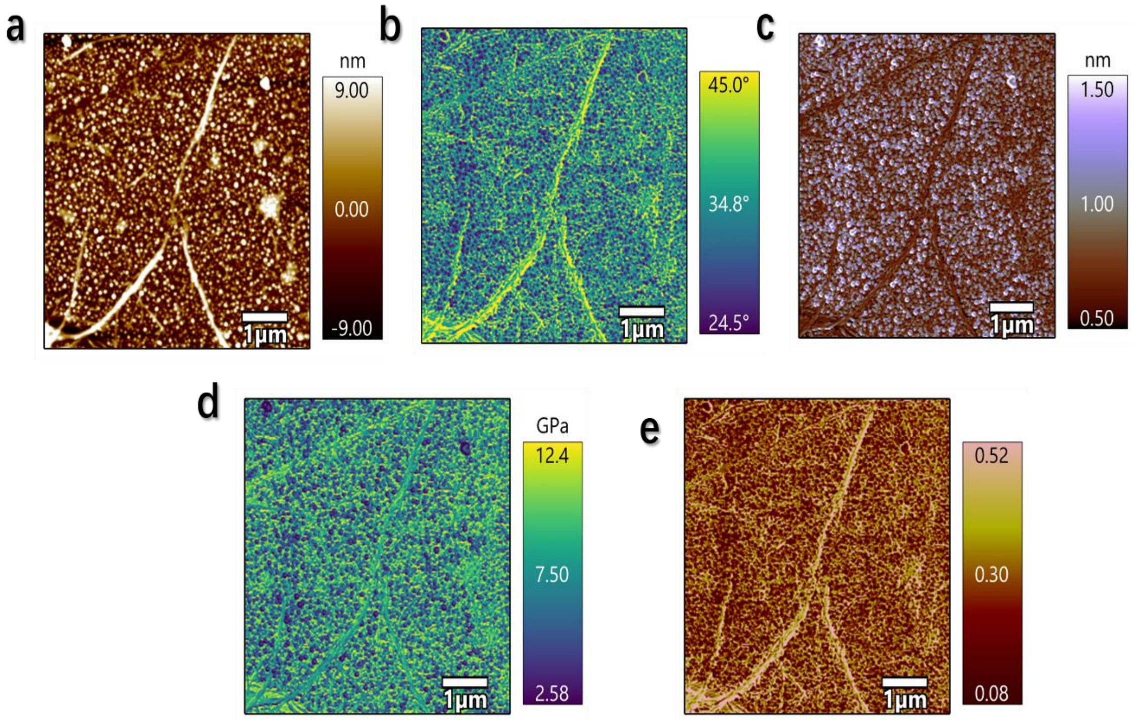

Figure 5.22 AMFM probing of PW12@SWCNTs: Height retrace (a), phase(b), Indentation (c), Young's Modulus(d), Loss tangent(e)

For spherical structure polar molecule-modified carbon nanotubes (PW12@SWCNTs), using the AM-FM module of AFM, we again identified the material region (Figure 5.22) and focused on a single carbon nanotube (Figure 5.23). By scanning across the nanotube and drawing a line, we obtained a Young's modulus ranging from 7 to 12 GPa. The Young's modulus showed a noticeable variation trend along the cross-section. Similarly, the measured loss tangent ranged from 0.15 to 0.25, with a significant variation trend along the cross-section.

For elliptical structure polar molecule-modified carbon nanotubes (P2W12@SWCNTs), using the AM-FM module of AFM, we performed the same procedure of identifying the material region (Figure 5.24) and focusing on a single carbon nanotube (Figure 5.24). The measured Young's modulus was around 4-8 GPa, while the loss tangent was approximately 0.45-0.5. Both the Young's modulus and loss factor exhibited significant variation along the cross-section. The results of the AM-FM mapping indicate that the incorporation of polar molecules and their interaction with carbon nanotubes alter the nanomechanical properties of the nanotubes. The combination of materials with significantly different mechanical properties, such as in the case of modified carbon nanotubes, creates an effective mechanical performance interface, leading to the generation of large stress gradients at the nanotube interface.

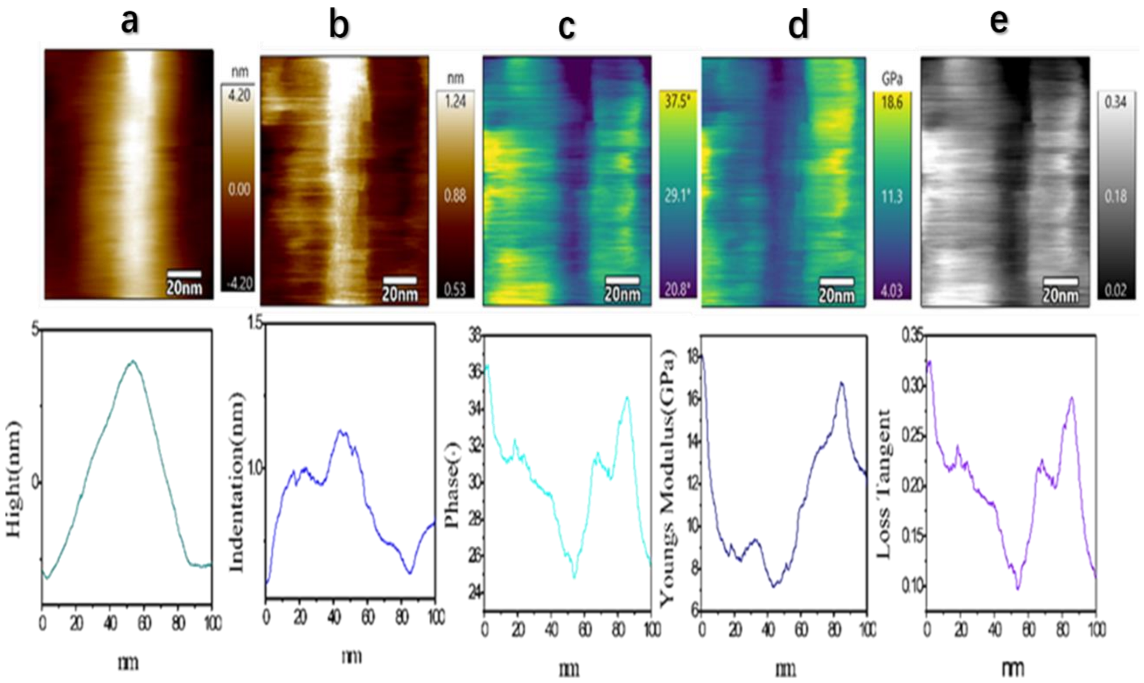

Figure 5.23 AMFM probing of PW12@SWCNTs: Height retrace (a), phase(b), Indentation (c), Young's Modulus(d), Loss tangent(e)

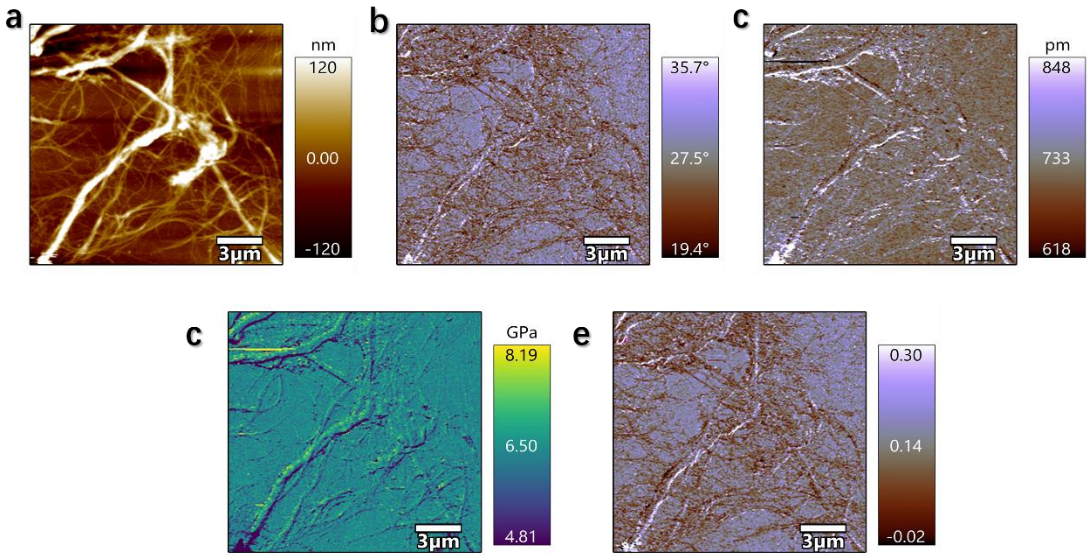

Figure 5.24 AMFM probing of P2W12@SWCNTs: Height retrace (a), phase(b), Indentation (c), Young's Modulus(d), Loss tangent(e)

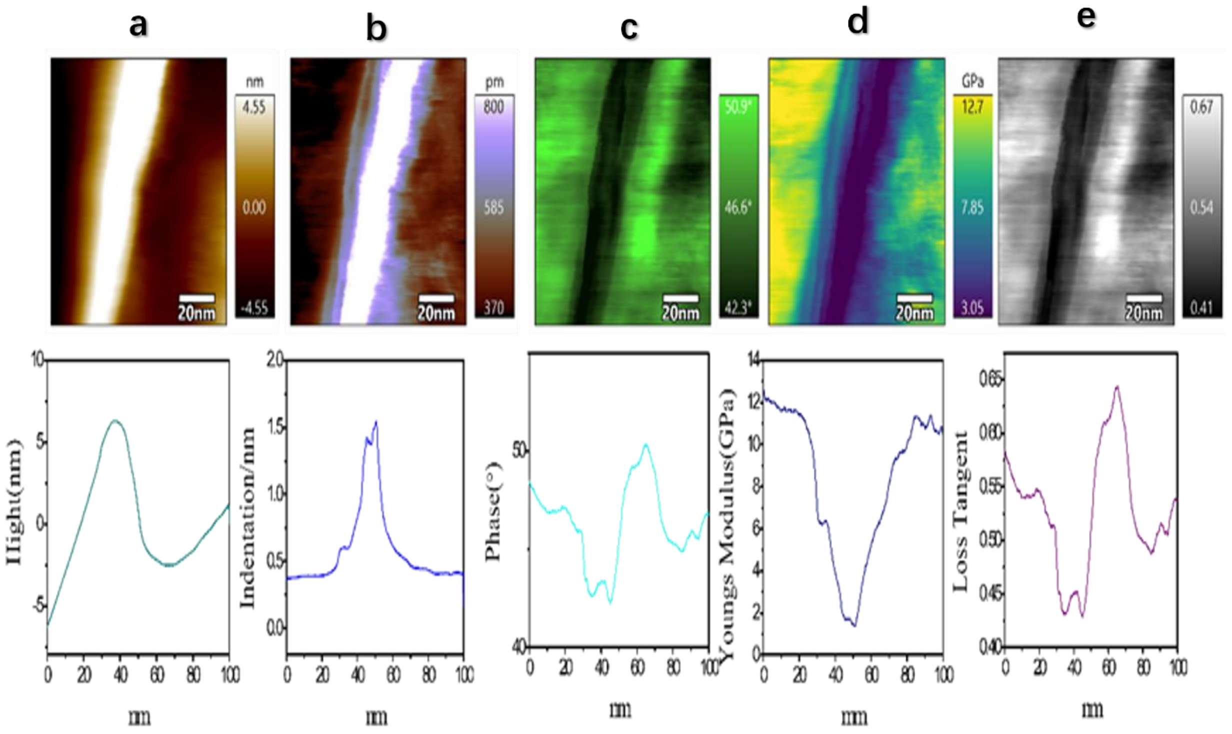

Figure 5.25 AMFM probing of P2W12@SWCNTs: Height retrace (a), Indentation (b), phase(c), Young's Modulus(d), Loss tangent(e)

5.6 Raman spectrum under different pressures

Raman spectroscopy is a commonly used method to characterize the structure and properties of carbon nanotubes. For carbon nanotubes, the Raman spectrum typically exhibits two main characteristic peaks, namely the G band and the D band. The D band peak is located at approximately 1350 cm^{-1} and provides information about the presence of amorphous carbon, defects, or edge structures in the carbon nanotubes. The G band peak is located at approximately 1580 cm^{-1} and arises from the C-C bond vibration between sp2 hybridized carbon atoms in the carbon nanotubes. Additionally, for single-walled carbon nanotubes, the position and shape of the G band can reveal their chirality. In this study, we proposed a strategy for flexoelectric enhancement of carbon nanotubes through the introduction of polarizable molecules. The interaction between the polarizable molecules and carbon atoms on the carbon nanotube surface affects the bonding and local electronic structure of sp2 hybridized carbon atoms, thereby enabling the construction of an effective flexoelectric enhancement interface. Based on this, we conducted Raman spectroscopy tests on modified and unmodified carbon nanotubes under different pressures. From the Raman spectra (Figure 5.26), the G and D peaks of the carbon nanotubes can be observed. When the pressure in the testing environment increases, the positions of the G and D peaks remain unchanged for unmodified single-walled nanotubes, indicating that the pressure variation does not alter the structure of the carbon nanotubes. However, for polarizable molecule-modified carbon nanotubes with a spherical structure (PW12@SWCNTs) and an elliptical structure (P2W12@SWCNTs), the position of the D peak remains unchanged, while the G peak shifts to the left by 1 wavenumber. This indicates a change in the C-C bond vibration between sp2 hybridized carbon atoms and a modification in the electronic transport properties on the surface of the carbon nanotubes. This is consistent with the previous hypothesis.

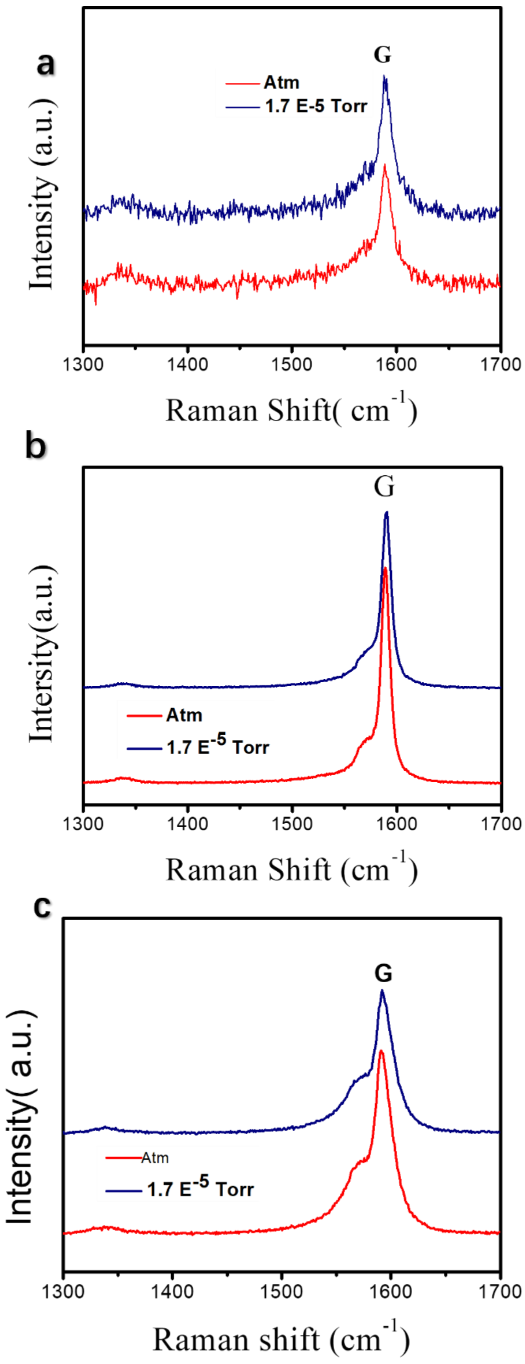

Figure 5.26 Raman Spectrums: SWCNTs(a), PW12@SWCNTs(b), P12W12@ SWCNTs(c) under different pressure

5.7 Conclusion

In conclusion, this study successfully constructed an interface that effectively enhances the flexoelectric effect by investigating the incorporation of spherical or elliptical polarizable molecules within nonpolarized SWCNTs. By combining AFM scanning with conductive probe tapping, strain gradient-induced electric signals were obtained from individual modified carbon nanotubes through point and line approaches. This experimental verification of the engineered interface-enhanced flexoelectric signal breaks new ground in theoretical research. Additionally, through AFM-based electrical, PFM, SCM, and AM-FM mode imaging, this study validated and visualized the strategy of engineering interface enhancement, which successfully alters the local electrical properties of carbon nanotube walls by redistributing electron cloud density and nanomechanical properties. This approach effectively serves as an enhanced interface for flexoelectric energy harvesting. Furthermore, Raman spectroscopy was employed to confirm the change in surface π-π conjugation of carbon nanotubes. Consequently, this study lays the foundation for expanding the structural design and application of novel carbon-based nanomaterials in flexoelectricity.

Chapter 6
Conclusions and Perspectives

To meet the increasingly severe global energy crisis and environmental issues, aiming for enhancing renewable energy harness, the development of novel and reliable nanomaterials are of vital importance in expanding their application areas. Therefore, this study focused on the development of novel carbon nanomaterials and structures based on facile fabrication, as well as the exploration of new strategies for sustainable energy conversion and utilization. Based on this, thesis focuses on three main tasks. This chapter provides a summary and conclusion of these tasks, along with a discussion on future work plans.

6.1 Conclusions

1. A novel 3-D nanocomposites of LIFT graphene/CuxO have been prepared using the laser-induced forward transfer method, working as the catalysts for hydrogen production. These nanocomposites were transferred onto nickel foam to fabricate electrodes for hydrogen production through water electrolysis. Due to the advantages of the rapid and simple LIFT fabrication method and the high specific surface area of LIFT graphene/CuxO, the prepared nanocomposites demonstrated excellent catalytic performance for low-cost hydrogen production. This work provides a novel approach for the development of novel carbon-based composites for hydrogen generation.

2. Portable solar evaporator based on LIFT graphene/Cu@non-woven fabric has been made by using the laser-induced forward transfer method combined with thermal evaporation. With a large solar capturing surface area, high spectral absorption of the full solar spectrum, and high photothermal conversion efficiency of LIFT graphene/Cu, as well as the Janus wettability exhibited on its designed structure and the constructed water transport channels from the porous structures, the solar evaporator showed excellent performance in light-to-heat interface evaporation. This research opens up opportunities for efficient solar-driven water evaporation.

3. The engineered interface constructed by incorporation of polarizable molecules inside SWCNTs has been investigated for enhanced flexoelectric effects. Through AFM scanning and characterization, the mechanism behind the engineered interface-enhanced flexoelectric effects have been validated and revealed, providing a foundation for the development of carbon-based nanomaterials for flexoelectric energy harvesting.

6.2 Perspectives

This thesis focuses on the utilization of advanced techniques to prepare novel carbon nanocomposites and structures, and the investigation of their applications in hydrogen energy generation, solar thermal utilization, and electromechanical energy harvesting. However, further efforts are still needed for deeper and broader research, development, and exploration of the challenges associated with the practical implementation of these new carbon nanomaterials in renewable energy collection, conversion, acquisition, and utilization. In future research, additional investigations will be directed towards the following directions:

1. The LIFT graphene/CuxO nanocomposites has been successfully prepared by using the laser-induced forward transfer method combined with the drop-casting technique and transferred them onto nickel foam to fabricate electrodes for hydrogen gas production through water electrolysis. The fabricated electrodes exhibited considerable HER performance. However, the system's hydrogen collection efficiency, system optimization, and yield assessment require further research.

2. The portable solar evaporator of LIFT graphene/Cu@non-woven solar evaporators has been fabricated by using the laser-induced forward transfer method combined with thermal evaporation. The prepared LIFT graphene/Cu composites showed promising photothermal characteristics. However, further research is needed on the thermal management of the entire evaporator in the infrared wavelength range, as well

as the construction of microstructures in the device and the understanding of the photothermal-enhanced solar interface evaporation mechanisms.

3. The engineered interfaces have been constructed by incorporation of polarizable molecules inside SWCNTs through enhanced flexoelectric effects. In the study, the generated electromechanical coupling electrical signals have been successfully captured through AFM tip nano-indentation, achieving a breakthrough in flexoelectric energy harvesting in nanostructured carbon materials. However, further research is required for its application at the micro or macro scale, including device design and energy harvesting.

Reference

[1] R. Newell, D. Raimi, G.J.R.f.t.F. Aldana, Global energy outlook 2019: the next generation of energy, 1(8) (2019).

[2] A.M.J.R. Omer, s.e. reviews, Green energies and the environment, 12(7) (2008) 1789-1821.

[3] J. Li, N.J.C.S. Wu, Technology, Semiconductor-based photocatalysts and photoelectrochemical cells for solar fuel generation: a review, 5(3) (2015) 1360-1384.

[4] N. Mahmood, C. Zhang, H. Yin, Y.J.J.o.M.C.A. Hou, Graphene-based nanocomposites for energy storage and conversion in lithium batteries, supercapacitors and fuel cells, 2(1) (2014) 15-32.

[5] O. Ellabban, H. Abu-Rub, F.J.R. Blaabjerg, s.e. reviews, Renewable energy resources: Current status, future prospects and their enabling technology, 39 (2014) 748-764.

[6] G.V. Ochoa, J.N. Alvarez, C.J.I.J.o.E.E. Acevedo, Policy, Research evolution on renewable energies resources from 2007 to 2017: A comparative study on solar, geothermal, wind and biomass energy, 9(6) (2019) 242-253.

[7] P.J.C.T. Ray, E. Policy, Renewable energy and sustainability, 21 (2019) 1517-1533.

[8] S. Bilgen, K. Kaygusuz, A.J.E.s. Sari, Renewable energy for a clean and sustainable future, 26(12) (2004) 1119-1129.

[9] M.P. Paranthaman, W. Wong-Ng, R.N. Bhattacharya, Semiconductor materials for solar photovoltaic cells, Springer2016.

[10] E. Miyako, C. Hosokawa, M. Kojima, M. Yudasaka, R. Funahashi, I. Oishi, et al., A Photo‐Thermal‐Electrical Converter Based On Carbon Nanotubes for Bioelectronic Applications, 50(51) (2011) 12266-12270.

[11] N. Li, D.J. Yang, Y. Shao, Y. Liu, J. Tang, L. Yang, et al., Nanostructured Black Aluminum Prepared by Laser Direct Writing as a High-Performance Plasmonic Absorber for Photothermal/Electric Conversion, ACS Appl Mater Interfaces 13(3) (2021) 4305-4315.

[12] J. Chen, B. Li, G. Hu, R. Aleisa, S. Lei, F. Yang, et al., Integrated Evaporator for Efficient Solar-Driven Interfacial Steam Generation, Nano Lett 20(8) (2020) 6051-6058.

[13] X. Chen, J. Zhang, C. Huang, Q. Wu, J. Wu, L. Xia, et al., Modification of Black Phosphorus Nanosheets with a Ni-Containing Carbon Layer as Efficient and Stable Hydrogen Production Electrocatalysts, ACS Appl Mater Interfaces 12(49) (2020) 54619-54626.

[14] X. Zou, Y.J.C.S.R. Zhang, Noble metal-free hydrogen evolution catalysts for water splitting, 44(15) (2015) 5148-5180.

[15] C.W. Tan, K.H. Tan, Y.T. Ong, A.R. Mohamed, S.H.S. Zein, S.H.J.E.C.f.a.S.W.V.N. Tan, et al., Carbon nanotubes applications: solar and fuel cells, hydrogen storage, lithium batteries, supercapacitors, nanocomposites, gas, pathogens, dyes, heavy metals and pesticides, (2012) 3-46.

[16] J. Gong, K. Sumathy, Q. Qiao, Z.J.R. Zhou, S.E. Reviews, Review on dye-sensitized solar cells (DSSCs): Advanced techniques and research trends, 68 (2017) 234-246.

[17] S. Ayachi, X. He, H.J.J.A.E.M. Yoon, Solar thermoelectricity for power generation, 13(28) (2023) 2300937.

[18] S.P. Philipps, A.W. Bett, K. Horowitz, S. Kurtz, Current status of concentrator photovoltaic (CPV) technology, National Renewable Energy Lab.(NREL), Golden, CO (United States), 2015.

[19] R. Zakharchenko, L. Licea-Jimenez, S. Pérez-Garcıa, P. Vorobiev, U. Dehesa-Carrasco, J. Perez-Robles, et al., Photovoltaic solar panel for a hybrid PV/thermal system, 82(1-2) (2004) 253-261.

[20] P. Cheng, D. Wang, P.J.A.S.S. Schaaf, A Review on Photothermal Conversion of Solar Energy with Nanomaterials and Nanostructures: From Fundamentals to Applications, Advanced Sustainable Systems 6(9) (2022) 2200115.

[21] X. Fu, L. Xu, J. Li, X. Sun, H.J.C. Peng, Flexible solar cells based on carbon nanomaterials, 139 (2018) 1063-1073.

[22] A.B. Asha, R. Narain, Nanomaterials properties, Polymer science and nanotechnology, Elsevier2020, pp. 343-359.

[23] U. Banin, N. Waiskopf, L. Hammarström, G. Boschloo, M. Freitag, E.M. Johansson, et al., Nanotechnology for catalysis and solar energy conversion, 32(4) (2020) 042003.

[24] P.S. Shuttleworth, H. Parker, A. Hunt, V. Budarin, A. Matharu, J.J.G.c. Clark, Applications of nanoparticles in biomass conversion to chemicals and fuels, 16(2) (2014) 573-584.

[25] N.S. Hudak, Nanostructured electrode materials for lithium-ion batteries, Lithium-Ion Batteries, Elsevier2014, pp. 57-82.

[26] H.K.J.M.R.B. Liu, An overview—Functional nanomaterials for lithium rechargeable batteries, supercapacitors, hydrogen storage, and fuel cells, 48(12) (2013) 4968-4973.

[27] B. Liu, C. Wang, S. Bazri, I.A. Badruddin, Y. Orooji, S. Saeidi, et al., Optical properties and thermal stability evaluation of solar absorbers enhanced by nanostructured selective coating films, 377 (2021) 939-957.

[28] G. Li, M. Li, R. Taylor, Y. Hao, G. Besagni, C.J.A.T.E. Markides, Solar energy utilisation: Current status and roll-out potential, 209 (2022) 118285.

[29] S. Shoeibi, H. Kargarsharifabad, M. Sadi, A. Arabkoohsar, S.A.A.J.S.E.T. Mirjalily, Assessments, A review on using thermoelectric cooling, heating, and electricity generators in solar energy applications, 52 (2022) 102105.

[30] A.W. Copeland, O.D. Black, A.J.C.r. Garrett, The Photovoltaic Effect, 31(1) (1942) 177-226.

[31] N.J.C.R. Hoffmann, Photochemical reactions as key steps in organic synthesis, 108(3) (2008) 1052-1103.

[32] J.-W. Xu, K. Yao, Z.-K.J.N. Xu, Nanomaterials with a photothermal effect for antibacterial activities: an overview, 11(18) (2019) 8680-8691.

[33] M.J.J.o.P. Ochsner, P.B. Biology, Photophysical and photobiological processes in the photodynamic therapy of tumours, 39(1) (1997) 1-18.

[34] M.N. Eke, Photovoltaic Characteristics and Applications, Electrode Materials for Energy Storage and Conversion, CRC Press2021, pp. 351-364.

[35] P. Douglas, H.D. Burrows, R.C. Evans, Foundations of photochemistry: a background on the interaction between light and molecules, Applied photochemistry, Springer2013, pp. 1-88.

[36] X. Wu, G.Y. Chen, G. Owens, D. Chu, H.J.M.T.E. Xu, Photothermal materials: A key platform enabling highly efficient water evaporation driven by solar energy, 12 (2019) 277-296.

[37] R.U. Tanvir, J. Zhang, T. Canter, D. Chen, J. Lu, Z.J.R. Hu, et al., Harnessing solar energy using phototrophic microorganisms: A sustainable pathway to bioenergy, biomaterials, and environmental solutions, 146 (2021) 111181.

[38] X. Cui, Q. Ruan, X. Zhuo, X. Xia, J. Hu, R. Fu, et al., Photothermal nanomaterials: a powerful light-to-heat converter, 123(11) (2023) 6891-6952.

[39] N.S. Fuzil, N.H. Othman, N.H. Alias, F. Marpani, M.H.D. Othman, A.F. Ismail, et al., A review on photothermal material and its usage in the development of photothermal membrane for sustainable clean water production, 517 (2021) 115259.

[40] B. Han, Y.L. Zhang, Q.D. Chen, H.B.J.A.F.M. Sun, Carbon‐based photothermal actuators, 28(40) (2018) 1802235.

[41] L. Ruiz-Perez, L. Rizzello, J. Wang, N. Li, G. Battaglia, Y.J.S.M. Pei, Polypyrrole and polyaniline nanocomposites with high photothermal conversion efficiency, 16(19) (2020) 4569-4573.

[42] K.W. Tan, C.M. Yap, Z. Zheng, C.Y. Haw, P.S. Khiew, W.S.J.A.S.S. Chiu, State‐of‐the‐Art Advances, Development, and Challenges of Metal Oxide Semiconductor Nanomaterials for Photothermal Solar Steam Generation, 6(4) (2022) 2100416.

[43] Z. Li, X. Xu, X. Sheng, P. Lin, J. Tang, L. Pan, et al., Solar-powered sustainable water production: state-of-the-art technologies for sunlight–energy–water nexus, 15(8) (2021) 12535-12566.

[44] F. Ni, N. Qiu, P. Xiao, C. Zhang, Y. Jian, Y. Liang, et al., Tillandsia‐inspired hygroscopic photothermal organogels for efficient atmospheric water harvesting, 59(43) (2020) 19237-19246.

[45] C. Chen, M. Wang, X. Chen, X. Chen, Q. Fu, H.J.C.E.J. Deng, Recent progress in solar photothermal steam technology for water purification and energy utilization, (2022) 137603.

[46] M. Gao, C.K. Peh, F.L. Meng, G.W.J.S.M. Ho, Photothermal membrane distillation toward solar water production, 5(5) (2021) 2001200.

[47] M. Gao, L. Zhu, C.K. Peh, G.W. Ho, Solar absorber material and system designs for photothermal water vaporization towards clean water and energy production, Energy Environmental Science 12(3) (2019) 841-864.

[48] W. Yao, X. Zhu, Z. Xu, R.A. Davis, G. Liu, H. Zhong, et al., Loofah sponge-derived hygroscopic photothermal absorber for all-weather atmospheric water harvesting, 14(3) (2022) 4680-4689.

[49] X. Wang, Y. He, Y. Hu, G. Jin, B. Jiang, Y.J.S.E. Huang, Photothermal-conversion-enhanced photocatalytic activity of flower-like CuS superparticles under solar light irradiation, 170 (2018) 586-593.

[50] D.R. Palo, R.A. Dagle, J.D.J.C.r. Holladay, Methanol steam reforming for hydrogen production, 107(10) (2007) 3992-4021.

[51] G. Chisholm, T. Zhao, L. Cronin, Hydrogen from water electrolysis, Storing Energy, Elsevier2022, pp. 559-591.

[52] M. Benghanem, A. Mellit, H. Almohamadi, S. Haddad, N. Chettibi, A.M. Alanazi, et al., Hydrogen production methods based on solar and wind energy: a review, 16(2) (2023) 757.

[53] J. Yu, Y. Dai, Q. He, C. Cheng, Z. Shao, M.J.A.P.R. Ni, Robust non-Pt noble metal-based nanomaterials for electrocatalytic hydrogen generation, 7(4) (2020).

[54] S. Shen, J. Chen, M. Wang, X. Sheng, X. Chen, X. Feng, et al., Titanium dioxide nanostructures for photoelectrochemical applications, 98 (2018) 299-385.

[55] M. Aziz, A. Darmawan, F.B.J.I.J.o.H.E. Juangsa, Hydrogen production from biomasses and wastes: A technological review, 46(68) (2021) 33756-33781.

[56] Y. Zeng, L. Wang, C. Wu, J. Wang, B. Shen, X.J.A.C.B.E. Tu, Low temperature reforming of biogas over K-, Mg-and Ce-promoted Ni/Al2O3 catalysts for the production of hydrogen rich syngas: Understanding the plasma-catalytic synergy, 224 (2018) 469-478.

[57] J. Chi, H.J.C.J.o.C. Yu, Water electrolysis based on renewable energy for hydrogen production, 39(3) (2018) 390-394.

[58] M.J.R.i.E. El-Shafie, Hydrogen production by water electrolysis technologies: a review, (2023) 101426.

[59] J. Garche, U. Stimming, A. Friedrich, R. Feidenhans, Hydrogen in portable devices, Risø energy report 3. Hydrogen and its competitors2004, pp. 47-51.

[60] C. Deng, C.Y. Toe, X. Li, J. Tan, H. Yang, Q. Hu, et al., Earth‐abundant metal‐based electrocatalysts promoted anodic reaction in hybrid water electrolysis for efficient hydrogen production: recent progress and perspectives, 12(25) (2022) 2201047.

[61] A.S. Emam, M.O. Hamdan, B.A. Abu-Nabah, E.J.I.J.o.H.E. Elnajjar, A review on recent trends, challenges, and innovations in alkaline water electrolysis, 64 (2024) 599-625.

[62] V. Vij, S. Sultan, A.M. Harzandi, A. Meena, J.N. Tiwari, W.-G. Lee, et al., Nickel-based electrocatalysts for energy-related applications: oxygen reduction, oxygen evolution, and hydrogen evolution reactions, 7(10) (2017) 7196-7225.

[63] J. Huang, Y. Jiang, T. An, M.J.J.o.M.C.A. Cao, Increasing the active sites and intrinsic activity of transition metal chalcogenide electrocatalysts for enhanced water splitting, 8(48) (2020) 25465-25498.

[64] B. You, M.T. Tang, C. Tsai, F. Abild‐Pedersen, X. Zheng, H.J.A.m. Li, Enhancing electrocatalytic water splitting by strain engineering, 31(17) (2019) 1807001.

[65] Y. Li, Z. Dong, L.J.A.E.M. Jiao, Multifunctional transition metal‐based phosphides in energy‐related electrocatalysis, 10(11) (2020) 1902104.

[66] W. Choi, N. Choudhary, G.H. Han, J. Park, D. Akinwande, Y.H.J.M.T. Lee, Recent development of two-dimensional transition metal dichalcogenides and their applications, 20(3) (2017) 116-130.

[67] W. Xiong, H. Yin, T. Wu, H.J.C.A.E.J. Li, Challenges and opportunities of transition metal oxides as electrocatalysts, 29(5) (2023) e202202872.

[68] J. Liu, J. Ma, Z. Zhang, Y. Qin, Y.-J. Wang, Y. Wang, et al., 2021 Roadmap: electrocatalysts for green catalytic processes, 4(2) (2021) 022004.

[69] Y. Wang, Y. Zhao, X. Ding, L.J.J.o.E.C. Qiao, Recent advances in the electrochemistry of layered post-transition metal chalcogenide nanomaterials for hydrogen evolution reaction, 60 (2021) 451-479.

[70] M. Ahmadi, O. Zabihi, S. Jeon, M. Yoonessi, A. Dasari, S. Ramakrishna, et al., 2D transition metal dichalcogenide nanomaterials: advances, opportunities, and challenges in multi-functional polymer nanocomposites, 8(3) (2020) 845-883.

[71] H. Fei, R. Liu, Y. Zhang, H. Wang, M. Wang, S. Wang, et al., Extending MoS2-based materials into the catalysis of non-acidic hydrogen evolution: challenges, progress, and perspectives, 2(2) (2023) 022103.

[72] Q. Zhai, Y. Pan, L.J.A.o.M.R. Dai, Carbon-based metal-free electrocatalysts: past, present, and future, 2(12) (2021) 1239-1250.

[73] P.J.E. Ligęza, On Search for Unconventional Energy Sources for Harvesting, 17(5) (2024) 1091.

[74] A. Ahmed, A. Azam, Y. Wang, Z. Zhang, N. Li, C. Jia, et al., Additively manufactured nano-mechanical energy harvesting systems: advancements, potential applications, challenges and future perspectives, 8 (2021) 1-42.

[75] L. Liu, X. Guo, W. Liu, C.J.N. Lee, Recent progress in the energy harvesting technology—from self-powered sensors to self-sustained IoT, and new applications, 11(11) (2021) 2975.

[76] L. Dong, A.B. Closson, C. Jin, I. Trase, Z. Chen, J.X.J.A.m.t. Zhang, Vibration ‐ energy ‐ harvesting system: transduction mechanisms, frequency tuning techniques, and biomechanical applications, 4(10) (2019) 1900177.

[77] V. Georgakilas, J.A. Perman, J. Tucek, R.J.C.r. Zboril, Broad family of carbon nanoallotropes: classification, chemistry, and applications of fullerenes, carbon dots, nanotubes, graphene, nanodiamonds, and combined superstructures, 115(11) (2015) 4744-4822.

[78] I. Suarez-Martinez, N. Grobert, C.J.C. Ewels, Nomenclature of sp2 carbon nanoforms, 50 (2011) 741-747.

[79] J.J.N. Vejpravová, Mixed sp2–sp3 nanocarbon materials: A status quo review, 11(10) (2021) 2469.

[80] A.O. Egbedina, O.P. Bolade, U. Ewuzie, E.C.J.J.o.E.C.E. Lima, Emerging trends in the application of carbon-based materials: A review, 10(2) (2022) 107260.

[81] Y. Peng, J. Hu, Y. Huan, Y.J.N. Zhang, Chemical Vapor Deposition Growth of Graphene and Other Nanomaterials with 3D Architectures towards Electrocatalysis and Secondary Batteries Related Applications, (2024).

[82] N. Jain, E. Gupta, N.J.J.S.S. Kanu, Plethora of Carbon nanotubes applications in various fields–A state-of-the-art-review, 10(1) (2022) 1-24.

[83] Z. Yang, J. Ren, Z. Zhang, X. Chen, G. Guan, L. Qiu, et al., Recent advancement of nanostructured carbon for energy applications, 115(11) (2015) 5159-5223.

[84] A. Armano, S.J.C. Agnello, Two-dimensional carbon: a review of synthesis methods, and electronic, optical, and vibrational properties of single-layer graphene, 5(4) (2019) 67.

[85] M. Sumdani, M. Islam, A. Yahaya, S.J.J.o.N.R. Safie, Recent advances of the graphite exfoliation processes and structural modification of graphene: a review, 23 (2021) 1-35.

[86] M. Yi, Z. Shen, A review on mechanical exfoliation for the scalable production of graphene, Journal of Materials Chemistry A 3(22) (2015) 11700-11715.

[87] H.J. Park, J. Meyer, S. Roth, V.J.C. Skákalová, Growth and properties of few-layer graphene prepared by chemical vapor deposition, 48(4) (2010) 1088-1094.

[88] R. Munoz, C. Gómez‐Aleixandre, Review of CVD synthesis of graphene, Chemical Vapor Deposition 19(10-11-12) (2013) 297-322.

[89] K.E. Whitener Jr, P.E. Sheehan, Graphene synthesis, Diamond and related materials 46 (2014) 25-34.

[90] A. Aqel, K.M. Abou El-Nour, R.A. Ammar, A.J.A.J.o.C. Al-Warthan, Carbon nanotubes, science and technology part (I) structure, synthesis and characterisation, 5(1) (2012) 1-23.

[91] W. Zhou, X. Bai, E. Wang, S.J.A.M. Xie, Synthesis, structure, and properties of single‐walled carbon nanotubes, 21(45) (2009) 4565-4583.

[92] R. Sharma, A.K. Sharma, V.J.C.E. Sharma, Synthesis of carbon nanotubes by arc-discharge and chemical vapor deposition method with analysis of its morphology, dispersion and functionalization characteristics, 2(1) (2015) 1094017.

[93] V. Jourdain, C.J.C. Bichara, Current understanding of the growth of carbon nanotubes in catalytic chemical vapour deposition, 58 (2013) 2-39.

[94] N. Arora, N.J.D. Sharma, r. materials, Arc discharge synthesis of carbon nanotubes: Comprehensive review, 50 (2014) 135-150.

[95] D. Tasis, N. Tagmatarchis, A. Bianco, M.J.C.r. Prato, Chemistry of carbon nanotubes, 106(3) (2006) 1105-1136.

[96] Z. Li, L. Wang, Y. Li, Y. Feng, W.J.C.S. Feng, Technology, Carbon-based functional nanomaterials: Preparation, properties and applications, 179 (2019) 10-40.

[97] Z. Xu, W. Deng, X.J.E.E.R. Wang, 3D hierarchical carbon-rich micro-/nanomaterials for energy storage and catalysis, 4 (2021) 269-335.

[98] B. Qiu, M. Xing, J.J.C.S.R. Zhang, Recent advances in three-dimensional graphene based materials for catalysis applications, 47(6) (2018) 2165-2216.

[99] J. Mao, J. Iocozzia, J. Huang, K. Meng, Y. Lai, Z.J.E. Lin, et al., Graphene aerogels for efficient energy storage and conversion, 11(4) (2018) 772-799.

[100] X. Zhang, J. Zhou, Y. Zheng, H. Wei, Z.J.C.E.J. Su, Graphene-based hybrid aerogels for energy and environmental applications, 420 (2021) 129700.

[101] Z. Liu, G. Du, Y. Zhou, X.J.D. Tian, R. Materials, Freeze-casting preparation of three-dimensional directional porous LiFePO4-graphene composite aerogel for lithium-ion battery, 137 (2023) 110074.

[102] M. Plata-Gryl, R. Castro-Muñoz, G.J.C. Boczkaj, S.A. Physicochemical, E. Aspects, Chemically reduced graphene oxide based aerogels-Insight on the surface and textural functionalities dependent on handling the synthesis factors, 675 (2023) 132005.

[103] J. Han, I. Johnson, M.J.A.M. Chen, 3D continuously porous graphene for energy applications, 34(15) (2022) 2108750.

[104] X. Xu, H. Liang, F. Ming, Z. Qi, Y. Xie, Z.J.A.C. Wang, Prussian blue analogues derived penroseite (Ni, Co) Se2 nanocages anchored on 3D graphene aerogel for efficient water splitting, 7(9) (2017) 6394-6399.

[105] P. Zhang, Q. Liao, H. Yao, H. Cheng, Y. Huang, C. Yang, et al., Three-dimensional water evaporation on a macroporous vertically aligned graphene pillar array under one sun, 6(31) (2018) 15303-15309.

[106] Z. Zhang, Y. Dong, F. Xiao, S.J.R.a. Wang, Multifunctional magnetic graphene hybrid architectures: one-pot synthesis and their applications as organic pollutants adsorbents and supercapacitor electrodes, 5(101) (2015) 83480-83485.

[107] H. Tetik, Y. Wang, X. Sun, D. Cao, N. Shah, H. Zhu, et al., Additive manufacturing of 3D aerogels and porous scaffolds: a review, 31(45) (2021) 2103410.

[108] N. Karousis, I. Suarez-Martinez, C.P. Ewels, N.J.C.r. Tagmatarchis, Structure, properties, functionalization, and applications of carbon nanohorns, 116(8) (2016) 4850-4883.

[109] V.K. Thakur, M.K. Thakur, Chemical functionalization of carbon nanomaterials, CRC Press Warentown (NJ2018.

[110] N. Karousis, N. Tagmatarchis, D.J.C.r. Tasis, Current progress on the chemical modification of carbon nanotubes, 110(9) (2010) 5366-5397.

[111] L.J.A.o.c.r. Dai, Functionalization of graphene for efficient energy conversion and storage, 46(1) (2013) 31-42.

[112] Z. Wei, D. Wang, S. Kim, S.-Y. Kim, Y. Hu, M.K. Yakes, et al., Nanoscale tunable reduction of graphene oxide for graphene electronics, 328(5984) (2010) 1373-1376.

[113] Y. Zhang, L. Guo, S. Wei, Y. He, H. Xia, Q. Chen, et al., Direct imprinting of microcircuits on graphene oxides film by femtosecond laser reduction, 5(1) (2010) 15-20.

[114] M.F. El-Kady, R.B.J.N.c. Kaner, Scalable fabrication of high-power graphene micro-supercapacitors for flexible and on-chip energy storage, 4(1) (2013) 1475.

[115] J. Lin, Z. Peng, Y. Liu, F. Ruiz-Zepeda, R. Ye, E.L. Samuel, et al., Laser-induced porous graphene films from commercial polymers, Nat Commun 5(5714) (2014) 5714.

[116] L.X. Duy, Z. Peng, Y. Li, J. Zhang, Y. Ji, J.M.J.C. Tour, Laser-induced graphene fibers, 126 (2018) 472-479.

[117] M. Abdulhafez, G.N. Tomaraei, M.J.A.A.N.M. Bedewy, Fluence-dependent morphological transitions in laser-induced graphene electrodes on polyimide substrates for flexible devices, 4(3) (2021) 2973-2986.

[118] D.X. Luong, K. Yang, J. Yoon, S.P. Singh, T. Wang, C.J. Arnusch, et al., Laser-induced graphene composites as multifunctional surfaces, 13(2) (2019) 2579-2586.

[119] Y. Dong, S.C. Rismiller, J.J.C. Lin, Molecular dynamic simulation of layered graphene clusters formation from polyimides under extreme conditions, 104 (2016) 47-55.

[120] A.F. Carvalho, A.J. Fernandes, C. Leitão, J. Deuermeier, A.C. Marques, R. Martins, et al., Laser‐induced graphene strain sensors produced by ultraviolet irradiation of polyimide, 28(52) (2018) 1805271.

[121] Y. Chen, J. Long, S. Zhou, D. Shi, Y. Huang, X. Chen, et al., UV laser‐induced polyimide‐to‐graphene conversion: modeling, fabrication, and application, 3(10) (2019) 1900208.

[122] B. Kulyk, B.F. Silva, A.F. Carvalho, P. Barbosa, A.V. Girão, J. Deuermeier, et al., Laser‐induced graphene from paper by ultraviolet irradiation: humidity and temperature sensors, 7(7) (2022) 2101311.

[123] W.K. Yung, J. Liu, H.C. Man, T.M.J.J.o.M.P.T. Yue, 355 nm Nd: YAG laser ablation of polyimide and its thermal effect, 101(1-3) (2000) 306-311.

[124] B. Shin, J. Oh, H.J.J.o.m.p.t. Sohn, Theoretical and experimental investigations into laser ablation of polyimide and copper films with 355-nm Nd: YVO4 laser, 187 (2007) 260-263.

[125] Q. Du, T. Chen, J. Liu, X.J.A.S.S. Zeng, Surface microstructure and chemistry of polyimide by single pulse ablation of picosecond laser, 434 (2018) 588-595.

[126] H. Zhong, Z. Zhu, J. Lin, C.F. Cheung, V.L. Lu, F. Yan, et al., Reusable and Recyclable Graphene Masks with Outstanding Superhydrophobic and Photothermal Performances, ACS Nano 14(5) (2020) 6213-6221.

[127] G. Li, Direct laser writing of graphene electrodes, Journal of Applied Physics 127(1) (2020) 010901.

[128] L. Huang, J. Su, Y. Song, R. Ye, Laser-Induced Graphene: En Route to Smart Sensing, Nano-Micro Letters 12(1) (2020).

[129] H. Zhong, Z. Zhu, P. You, J. Lin, C.F. Cheung, V.L. Lu, et al., Plasmonic and Superhydrophobic Self-Decontaminating N95 Respirators, ACS Nano 14(7) (2020) 8846-8854.

[130] D. Xu, K.C. Chan, H. Guo, H. Zhong, L. Lu, One-step fabrication of a laser-induced forward transfer graphene/CuxO nanocomposite-based electrocatalyst to promote hydrogen evolution reaction, Journal of Materials Chemistry A 9(30) (2021) 16470-16478.

[131] L. Li, J. Zhang, Z. Peng, Y. Li, C. Gao, Y. Ji, et al., High‐performance pseudocapacitive microsupercapacitors from laser‐induced graphene, Advanced Materials 28(5) (2016) 838-845.

[132] Y. Zhang, N. Li, Y. Xiang, D. Wang, P. Zhang, Y. Wang, et al., A flexible non-enzymatic glucose sensor based on copper nanoparticles anchored on laser-induced graphene, Carbon 156 (2020) 506-513.

[133] J. Zhang, C. Zhang, J. Sha, H. Fei, Y. Li, J.M. Tour, Efficient water-splitting electrodes based on laser-induced graphene, ACS applied materials & interfaces 9(32) (2017) 26840-26847.

[134] R. Ye, Z. Peng, T. Wang, Y. Xu, J. Zhang, Y. Li, et al., In Situ Formation of Metal Oxide Nanocrytals Embedded in Laser-Induced Graphene, ACS Nano 9(9) (2015) 9244-9251.

[135] J. Yeo, S. Hong, G. Kim, H. Lee, Y.D. Suh, I. Park, et al., Laser-Induced Hydrothermal Growth of Heterogeneous Metal-Oxide Nanowire on Flexible Substrate by Laser Absorption Layer Design, ACS Nano 9(6) (2015) 6059-6068.

[136] L. Ge, Q. Hong, H. Li, F. Li, A laser-induced TiO2-decorated graphene photoelectrode for sensitive photoelectrochemical biosensing, Chem Commun (Camb) 55(34) (2019) 4945-4948.

[137] X. Sun, X. Gao, J. Chen, X. Wang, H. Chang, B. Li, et al., Ultrasmall Ru Nanoparticles Highly Dispersed on Sulfur-Doped Graphene for HER with High Electrocatalytic Performance, ACS Appl Mater Interfaces 12(43) (2020) 48591-48597.

[138] S. Zhang, M. Jin, T. Shi, M. Han, Q. Sun, Y. Lin, et al., Electrocatalytically Active Fe-(O-C2)4 Single-Atom Sites for Efficient Reduction of Nitrogen to Ammonia, Angew Chem Int Ed Engl 59(32) (2020) 13423-13429.

[139] F. Wang, Y.p. Liu, H. Zhang, K. Chu, CuO/Graphene Nanocomposite for Nitrogen Reduction Reaction, ChemCatChem 11(5) (2019) 1441-1447.

[140] K. Wang, B. Huang, F. Lin, F. Lv, M. Luo, P. Zhou, et al., Wrinkled Rh2P Nanosheets as Superior pH-Universal Electrocatalysts for Hydrogen Evolution Catalysis, Advanced Energy Materials 8(27) (2018) 1801891.

[141] M.G. Walter, E.L. Warren, J.R. McKone, S.W. Boettcher, E.A.S. Qixi Mi, a.N.S. Lewis, Solar Water Splitting Cells, Chemical Reviews 110(11) (2010) 6446-6473.

[142] J.L. Fajin, D.S.C. MN, J.R. Gomes, Density functional theory study of the water dissociation on platinum surfaces: general trends, J Phys Chem A 118(31) (2014) 5832-40.

[143] Z. Dong, F. Lin, Y. Yao, L. Jiao, Crystalline Ni(OH)2/Amorphous NiMoOxMixed‐Catalyst with Pt‐Like Performance for Hydrogen Production, Advanced Energy Materials 9(46) (2019) 1902703.

[144] J. Li, Z. Wen, Z.X. Hui, Z.W. Chen, C.C. Yang, Q. Jiang, Graphene-MoS2 vertically anchored on an MXene-derived accordion-like TiO2/C skeleton: an ultrastable HER catalyst, Journal of Materials Chemistry A 8(28) (2020) 14223-14233.

[145] F. Zare Bidoky, B. Tang, R. Ma, K.S. Jochem, W.J. Hyun, D. Song, et al., Sub‐3 V ZnO Electrolyte‐Gated Transistors and Circuits with Screen‐Printed and Photo‐Crosslinked Ion Gel Gate Dielectrics: New Routes to Improved Performance, Advanced Functional Materials 30(20) (2019) 1902028.

[146] B. Long, H. Yang, M. Li, M.-S. Balogun, W. Mai, G. Ouyang, et al., Interface charges redistribution enhanced monolithic etched copper foam-based Cu2O layer/TiO2 nanodots heterojunction with high hydrogen evolution electrocatalytic activity, Applied Catalysis B: Environmental 243 (2019) 365-372.

[147] A. Dey, G. Chandrabose, L.A.O. Damptey, E.S. Erakulan, R. Thapa, S. Zhuk, et al., Cu_2O/CuO heterojunction catalysts through atmospheric pressure plasma induced defect passivation, Applied Surface Science (2020) 148571.

[148] A. Aktar, S. Ahmmed, J. Hossain, A.B.M. Ismail, Solution-Processed Synthesis of Copper Oxide (CuxO) Thin Films for Efficient Photocatalytic Solar Water Splitting, ACS Omega 5(39) (2020) 25125-25134.

[149] Q. Liu, Q. Liu, X. Kong, Cu-Based Nanosheet Arrays for Water-Splitting, ACS Applied Nano Materials 2(9) (2019) 6000-6009.

[150] X. Zhang, J. Wang, D. Liu, Y. Zhang, P.K. Chu, Z.-Y. Zhou, et al., Insight into the overpotentials of electrocatalytic hydrogen evolution on black phosphorus decorated with metal clusters, Electrochimica Acta 358 (2020) 136902.

[151] J. Pan, P. Wang, P. Wang, Q. Yu, J. Wang, C. Song, et al., The photocatalytic overall water splitting hydrogen production of g-C3N4/CdS hollow core–shell heterojunction via the HER/OER matching of Pt/MnOx, Chemical Engineering Journal 405 (2021) 126622.

[152] K. Chu, Y.P. Liu, Y.B. Li, Y.L. Guo, Y. Tian, Two-dimensional (2D)/2D Interface Engineering of a MoS2/C3N4 Heterostructure for Promoted Electrocatalytic Nitrogen Fixation, ACS Appl Mater Interfaces 12(6) (2020) 7081-7090.

[153] J.L. Silva, B. Brena, C.M. Araujo, g-C3N4/WTe2 Hybrid Electrocatalyst for Efficient Hydrogen Evolution Reaction, The Journal of Physical Chemistry C 124(16) (2020) 8726-8735.

[154] J. Joyner, E.F. Oliveira, H. Yamaguchi, K. Kato, S. Vinod, D.S. Galvao, et al., Graphene Supported MoS2 Structures with High Defect Density for an Efficient HER Electrocatalysts, ACS Appl Mater Interfaces 12(11) (2020) 12629-12638.

[155] S. Afroj, S. Tan, A.M. Abdelkader, K.S. Novoselov, N. Karim, Highly Conductive, Scalable, and Machine Washable Graphene‐Based E‐Textiles for Multifunctional Wearable Electronic Applications, Advanced Functional Materials 30(23) (2020) 2000293.

[156] M. Tavakkoli, E. Flahaut, P. Peljo, J. Sainio, F. Davodi, E.V. Lobiak, et al., Mesoporous Single-Atom-Doped Graphene–Carbon Nanotube Hybrid: Synthesis and Tunable Electrocatalytic Activity for Oxygen Evolution and Reduction Reactions, ACS Catalysis 10(8) (2020) 4647-4658.

[157] N. Jiang, Y. Wang, K.C. Chan, C.Y. Chan, H. Sun, G. Li, Additive Manufactured Graphene Coating with Synergistic Photothermal and Superhydrophobic Effects for Bactericidal Applications, Glob Chall 4(1) (2020) 1900054.

[158] Y.L. Wang, G.J. Li, K.C. Chan, Cost-effective and eco-friendly laser-processed cotton paper for high-performance solar evaporation, Solar Energy Materials and Solar Cells 218 (2020) 110693.

[159] H. Zhang, Z. Luo, Y. Liu, Y. Jiang, Noble-metal-free Ni3C as co-catalyst on LaNiO3 with enhanced photocatalytic activity, Applied Catalysis B: Environmental 277 (2020) 119166.

[160] G. Li, X. Mo, W.-C. Law, K.C. Chan, 3D printed graphene/nickel electrodes for high areal capacitance electrochemical storage, Journal of Materials Chemistry A 7(8) (2019) 4055-4062.

[161] Z. Lu, L. Wu, X. Dai, Y. Wang, M. Sun, C. Zhou, et al., Novel flexible bifunctional amperometric biosensor based on laser engraved porous graphene array electrodes: Highly sensitive electrochemical determination of hydrogen peroxide and glucose, J Hazard Mater 402(123774) (2021) 123774.

[162] W. Ma, J. Zhu, Z. Wang, W. Song, G. Cao, Recent advances in preparation and application of laser-induced graphene in energy storage devices, Materials Today Energy 18 (2020) 100569.

[163] S.-L. Wu, H. Chen, H.-L. Wang, X. Chen, H.-C. Yang, S.B. Darling, Solar-driven evaporators for water treatment: challenges and opportunities, Environmental Science: Water Research & Technology 7(1) (2021) 24-39.

[164] M. Badruzzaman, N. Voutchkov, L. Weinrich, J.G.J.D. Jacangelo, Selection of pretreatment technologies for seawater reverse osmosis plants: A review, Desalination 449 (2019) 78-91.

[165] J. Kim, K. Park, D.R. Yang, S.J.A.E. Hong, A comprehensive review of energy consumption of seawater reverse osmosis desalination plants, Applied Energy 254 (2019) 113652.

[166] F. Liu, L. Wang, R. Bradley, B. Zhao, W. Wu, Graphene – carbon composites for solar and low - voltage powered efficient interfacial evaporation, Advanced Sustainable Systems 4(3) (2020) 1900122.

[167] L. Su, Y. Ning, Z. Ma, Y. Zhang, C. Liu, Y. Zhang, et al., Polypyrrole‐Reinforced N, S‐Doping Graphene Foam for Efficient Solar Purification of Wastewater, Solar RRL 5(7) (2021) 2100210.

[168] L. Ai, J. Su, M. Wang, J. Jiang, Bamboo-structured nitrogen-doped carbon nanotube coencapsulating cobalt and molybdenum carbide nanoparticles: an efficient bifunctional electrocatalyst for overall water splitting, ACS Sustainable Chemistry Engineering 6(8) (2018) 9912-9920.

[169] Y. Fu, G. Wang, T. Mei, J. Li, J. Wang, X. Wang, Accessible Graphene Aerogel for Efficiently Harvesting Solar Energy, ACS Sustainable Chemistry & Engineering 5(6) (2017) 4665-4671.

[170] M. Zhang, F. Xu, W. Liu, Y. Hou, L. Su, X. Zhang, et al., Antibacterial evaporator based on reduced graphene oxide/polypyrrole aerogel for solar-driven desalination, Nano Research (2022).

[171] X. Hu, W. Xu, L. Zhou, Y. Tan, Y. Wang, S. Zhu, et al., Tailoring Graphene Oxide-Based Aerogels for Efficient Solar Steam Generation under One Sun, Adv Mater 29(5) (2017).

[172] Y. Li, T. Gao, Z. Yang, C. Chen, Y. Kuang, J. Song, et al., Graphene oxide-based evaporator with one-dimensional water transport enabling high-efficiency solar desalination, Nano Energy 41 (2017) 201-209.

[173] V.D. Dao, H.S. Choi, Carbon‐based sunlight absorbers in solar‐driven steam generation devices, Global Challenges 2(2) (2018) 1700094.

[174] J. Xu, F. Xu, M. Qian, Z. Li, P. Sun, Z. Hong, et al., Copper nanodot-embedded graphene urchins of nearly full-spectrum solar absorption and extraordinary solar desalination, Nano Energy 53 (2018) 425-431.

[175] W. Wang, X. Yan, J. Geng, N. Zhao, L. Liu, T. Vogel, et al., Engineering a Copper@Polypyrrole Nanowire Network in the Near Field for Plasmon-Enhanced Solar Evaporation, ACS Nano 15(10) (2021) 16376-16394.

[176] Y. Wang, C. Wang, X. Song, S.K. Megarajan, H. Jiang, A facile nanocomposite strategy to fabricate a rGO–MWCNT photothermal layer for efficient water evaporation, Journal of Materials Chemistry A 6(3) (2018) 963-971.

[177] M. Ji, H. Liu, M. Cheng, L. Huang, G. Yang, F. Bao, et al., Plasmonic metal nanoparticle loading to enhance the photothermal conversion of carbon fibers, The Journal of Physical Chemistry C 126(5) (2022) 2454-2462.

[178] H.D. Kiriarachchi, F.S. Awad, A.A. Hassan, J.A. Bobb, A. Lin, M.S. El-Shall, Plasmonic chemically modified cotton nanocomposite fibers for efficient solar water desalination and wastewater treatment, Nanoscale 10(39) (2018) 18531-18539.

[179] F.S. Awad, H.D. Kiriarachchi, K.M. AbouZeid, Ü. Özgür, M.S. El-Shall, Plasmonic Graphene Polyurethane Nanocomposites for Efficient Solar Water Desalination, ACS Applied Energy Materials 1(3) (2018) 976-985.

[180] T. Ding, Y. Zhou, W.L. Ong, G.W. Ho, Hybrid solar-driven interfacial evaporation systems: Beyond water production towards high solar energy utilization, Materials Today Energy 42 (2021) 178-191.

[181] P. Tao, G. Ni, C. Song, W. Shang, J. Wu, J. Zhu, et al., Solar-driven interfacial evaporation, Nature energy 3(12) (2018) 1031-1041.

[182] F. Nawaz, Y. Yang, S. Zhao, M. Sheng, C. Pan, W. Que, Innovative salt-blocking technologies of photothermal materials in solar-driven interfacial desalination, Journal of Materials Chemistry A 9(30) (2021) 16233-16254.

[183] M. Zhu, Y. Li, F. Chen, X. Zhu, J. Dai, Y. Li, et al., Plasmonic Wood for High-Efficiency Solar Steam Generation, Advanced Energy Materials 8(4) (2018).

[184] Y. Kuang, C. Chen, S. He, E.M. Hitz, Y. Wang, W. Gan, et al., A High-Performance Self-Regenerating Solar Evaporator for Continuous Water Desalination, Adv Mater 31(23) (2019) e1900498.

[185] X. Mo, K.C. Chan, E.C.M. Tse, A Scalable Laser-Assisted Method to Produce Active and Robust Graphene-Supported Nanoparticle Electrocatalysts, Chemistry of Materials 31(19) (2019) 8230-8238.

[186] Z. Chen, Q. Li, X. Chen, Porous graphene/polyimide membrane with a three-dimensional architecture for rapid and efficient solar desalination via interfacial evaporation, ACS Sustainable Chemistry Engineering 8(36) (2020) 13850-13858.

[187] D. Xu, K. Chan, H. Guo, H. Zhong, L. Lu, One-step fabrication of a laser-induced forward transfer graphene/Cu x O nanocomposite-based electrocatalyst to promote hydrogen evolution reaction, Journal of Materials Chemistry A 9(30) (2021) 16470-16478.

[188] S. Kim, J.M. Kim, J.E. Park, J.M. Nam, Nonnoble‐Metal‐Based Plasmonic Nanomaterials: Recent Advances and Future Perspectives, Advanced Materials 30(42) (2018) 1704528.

[189] G. Li, W.-C. Law, K.C. Chan, Floating, highly efficient, and scalable graphene membranes for seawater desalination using solar energy, Green Chemistry 20(16) (2018) 3689-3695.

[190] Y. Xu, H. Zhang, J. Song, D. Wang, X. Gu, Boosting the on-demand hydrogen generation from aqueous ammonia borane by the visible-light-driven synergistic electron effect in antenna-reactor-type catalysts with plasmonic copper spheres and noble-metal-free nanoparticles, Chemical Engineering Journal 401 (2020) 126068.

[191] H. Cheng, N. Yang, Q. Lu, Z. Zhang, H. Zhang, Syntheses and properties of metal nanomaterials with novel crystal phases, Advanced Materials 30(26) (2018) 1707189.

[192] Y. Wang, T. Williams, T. Gengenbach, B. Kong, D. Zhao, H. Wang, et al., Unique hybrid Ni 2 P/MoO 2@ MoS 2 nanomaterials as bifunctional non-noble-metal electro-catalysts for water splitting, Nanoscale 9(44) (2017) 17349-17356.

[193] S.-S. Yi, X.-B. Zhang, B.-R. Wulan, J.-M. Yan, Q. Jiang, Non-noble metals applied to solar water splitting, Energy & Environmental Science 11(11) (2018) 3128-3156.

[194] H. Duan, T. Wang, Z. Su, H. Pang, C. Chen, Recent progress and challenges in plasmonic nanomaterials, Nanotechnology Reviews 11(1) (2022) 846-873.

[195] W. Wu, L. Wang, Y. Li, F. Zhang, L. Lin, S. Niu, et al., Piezoelectricity of single-atomic-layer MoS2 for energy conversion and piezotronics, 514(7523) (2014) 470-474.

[196] C. Covaci, A.J.S. Gontean, Piezoelectric energy harvesting solutions: A review, 20(12) (2020) 3512.

[197] N. Sezer, M.J.N.e. Koç, A comprehensive review on the state-of-the-art of piezoelectric energy harvesting, 80 (2021) 105567.

[198] L. Lu, W. Ding, J. Liu, B.J.N.E. Yang, Flexible PVDF based piezoelectric nanogenerators, 78 (2020) 105251.

[199] M. Smith, S.J.I.M.R. Kar-Narayan, Piezoelectric polymers: theory, challenges and opportunities, 67(1) (2022) 65-88.

[200] O. Aktas, M. Kangama, G. Linyu, G. Catalan, X. Ding, A. Zunger, et al., Piezoelectricity in nominally centrosymmetric phases, 3(4) (2021) 043221.

[201] D. Lee, A. Yoon, S. Jang, J.-G. Yoon, J.-S. Chung, M. Kim, et al., Giant flexoelectric effect in ferroelectric epitaxial thin films, 107(5) (2011) 057602.

[202] L. Wang, S. Liu, X. Feng, C. Zhang, L. Zhu, J. Zhai, et al., Flexoelectronics of centrosymmetric semiconductors, 15(8) (2020) 661-667.

[203] P.V. Yudin, A.K.J.N. Tagantsev, Fundamentals of flexoelectricity in solids, 24(43) (2013) 432001.

[204] X. Wen, D. Li, K. Tan, Q. Deng, S.J.P.r.l. Shen, Flexoelectret: an electret with a tunable flexoelectriclike response, 122(14) (2019) 148001.

[205] M. Grasinger, K. Mozaffari, P.J.P.o.t.N.A.o.S. Sharma, Flexoelectricity in soft elastomers and the molecular mechanisms underpinning the design and emergence of giant flexoelectricity, 118(21) (2021) e2102477118.

[206] D. Codony, P. Gupta, O. Marco, I.J.J.o.t.M. Arias, P.o. Solids, Modeling flexoelectricity in soft dielectrics at finite deformation, 146 (2021) 104182.

[207] P. Van Minh, L.M. Thai, N.T. Dung, A. Tounsi, N.T.C. Nhung, D.J.I.J.o.M. Van Thom, et al., An overview of the flexoelectric phenomenon, potential applications, and proposals for further research directions, 19(4) (2023) 903-925.

[208] P. Zubko, G. Catalan, A.K.J.A.R.o.M.R. Tagantsev, Flexoelectric effect in solids, 43 (2013) 387-421.

[209] L. Molina-Luna, S. Wang, Y. Pivak, A. Zintler, H.H. Pérez-Garza, R.G. Spruit, et al., Enabling nanoscale flexoelectricity at extreme temperature by tuning cation diffusion, 9(1) (2018) 1-8.

[210] W. Huang, K. Kim, S. Zhang, F.G. Yuan, X.J.p.s.s.R.R.L. Jiang, Scaling effect of flexoelectric (Ba, Sr) TiO3 microcantilevers, 5(9) (2011) 350-352.

[211] T.D. Nguyen, S. Mao, Y.W. Yeh, P.K. Purohit, M.C.J.A.M. McAlpine, Nanoscale flexoelectricity, 25(7) (2013) 946-974.

[212] Y. Xia, W. Qian, Y.J.A.A.M. Yang, Interfaces, Advancements and Prospects of Flexoelectricity, (2024).

[213] J. Hong, D.J.P.R.B. Vanderbilt, First-principles theory and calculation of flexoelectricity, 88(17) (2013) 174107.

[214] X. Liang, S. Hu, S.J.S.M. Shen, Structures, Nanoscale mechanical energy harvesting using piezoelectricity and flexoelectricity, 26(3) (2017) 035050.

[215] A. Abdollahi, I.J.J.o.A.M. Arias, Constructive and destructive interplay between piezoelectricity and flexoelectricity in flexural sensors and actuators, 82(12) (2015) 121003.

[216] V.I. Artyukhov, S. Gupta, A. Kutana, B.I.J.N.l. Yakobson, Flexoelectricity and charge separation in carbon nanotubes, 20(5) (2020) 3240-3246.

[217] H. Qiao, P. Zhao, O. Kwon, A. Sohn, F. Zhuo, D.M. Lee, et al., Mixed triboelectric and flexoelectric charge transfer at the nanoscale, 8(20) (2021) 2101793.

[218] J. Narvaez, F. Vasquez-Sancho, G.J.N. Catalan, Enhanced flexoelectric-like response in oxide semiconductors, 538(7624) (2016) 219-221.

[219] J.Y. Fu, W. Zhu, N. Li, L.E.J.J.o.A.P. Cross, Experimental studies of the converse flexoelectric effect induced by inhomogeneous electric field in a barium strontium titanate composition, 100(2) (2006).

[220] S. Huang, L. Qi, W. Huang, L. Shu, S. Zhou, X.J.J.o.A.D. Jiang, Flexoelectricity in dielectrics: Materials, structures and characterizations, 8(02) (2018) 1830002.

[221] D. Tian, D.-Y. Jeong, Z. Fu, B. Chu, Flexoelectric effect of ferroelectric materials and its applications, Actuators, MDPI, 2023, p. 114.

[222] P. Mohammadi, L. Liu, P.J.J.o.A.M. Sharma, A theory of flexoelectric membranes and effective properties of heterogeneous membranes, 81(1) (2014) 011007.

[223] K.M. Hamdia, H. Ghasemi, X. Zhuang, N. Alajlan, T.J.C.M.i.A.M. Rabczuk, Engineering, Sensitivity and uncertainty analysis for flexoelectric nanostructures, 337 (2018) 95-109.

[224] X. Zhuang, B.H. Nguyen, S.S. Nanthakumar, T.Q. Tran, N. Alajlan, T.J.E. Rabczuk, Computational modeling of flexoelectricity—A review, 13(6) (2020) 1326.

[225] Q. Deng, S. Lv, Z. Li, K. Tan, X. Liang, S.J.J.o.A.P. Shen, The impact of flexoelectricity on materials, devices, and physics, 128(8) (2020).

[226] J.C. Marin Angel, T.J.A.A.M. Kyu, Interfaces, Flexoelectric Ionic Liquid-Grafted Triblock Copolymers for Energy Harvesting under Flexural Deformation, 15(49) (2023) 57434-57446.

[227] Q. Deng, L. Liu, P.J.P.R.E. Sharma, Electrets in soft materials: Nonlinearity, size effects, and giant electromechanical coupling, 90(1) (2014) 012603.

[228] A.H. Rahmati, S. Yang, S. Bauer, P.J.S.m. Sharma, Nonlinear bending deformation of soft electrets and prospects for engineering flexoelectricity and transverse (d 31) piezoelectricity, 15(1) (2019) 127-148.

[229] S. Das, B. Wang, T.R. Paudel, S.M. Park, E.Y. Tsymbal, L.-Q. Chen, et al., Enhanced flexoelectricity at reduced dimensions revealed by mechanically tunable quantum tunnelling, 10(1) (2019) 537.

[230] I.B.J.A.P.L. Bersuker, Pseudo Jahn–Teller effect in the origin of enhanced flexoelectricity, 106(2) (2015).

[231] A. Biancoli, C.M. Fancher, J.L. Jones, D.J.N.m. Damjanovic, Breaking of macroscopic centric symmetry in paraelectric phases of ferroelectric materials and implications for flexoelectricity, 14(2) (2015) 224-229.

[232] S. Kundalwal, V.K. Choyal, V. Choyal, S. Nevhal, N.J.P.E.L.-d.S. Luhadiya, Nanostructures, Enhancement of piezoelectric and flexoelectric response of boron nitride sheet superlattices via interface and defect engineering, 127 (2021) 114563.

[233] H. Shang, X. Liang, F. Deng, S. Hu, S.J.I.J.o.M.S. Shen, Flexoelectricity in wrinkled thin films, 234 (2022) 107685.

[234] K.S. Moreira, E. Lorenzett, A.L. Devens, Y.A. Santos da Campo, D. Mehler, T.A.J.J.o.A.P. Burgo, Low-cost elastomer-based flexoelectric devices, 129(23) (2021).

[235] Y. Shin, Y. Jiang, Q. Wang, Z. Zhou, G. Qin, D.-K.J.P.R. Yang, Flexoelectric-effect-based light waveguide liquid crystal display for transparent display, 10(2) (2022) 407-414.

[236] L.J.E. Qi, Energy harvesting properties of the functionally graded flexoelectric microbeam energy harvesters, 171 (2019) 721-730.

[237] P. Ajayan, J.-C. Charlier, A.J.P.o.t.N.A.o.S. Rinzler, Carbon nanotubes: from macromolecules to nanotechnology, 96(25) (1999) 14199-14200.

[238] T.W. Odom, J.-L. Huang, P. Kim, C.M.J.N. Lieber, Atomic structure and electronic properties of single-walled carbon nanotubes, 391(6662) (1998) 62-64.

[239] S. Niyogi, M. Hamon, H. Hu, B. Zhao, P. Bhowmik, R. Sen, et al., Chemistry of single-walled carbon nanotubes, 35(12) (2002) 1105-1113.

[240] T. Dumitrică, C.M. Landis, B.I.J.C.p.l. Yakobson, Curvature-induced polarization in carbon nanoshells, 360(1-2) (2002) 182-188.

[241] A.G. Kvashnin, P.B. Sorokin, B.I.J.T.j.o.p.c.l. Yakobson, Flexoelectricity in carbon nanostructures: Nanotubes, fullerenes, and nanocones, 6(14) (2015) 2740-2744.

[242] X. Yang, T. Liu, R. Li, X. Yang, M. Lyu, L. Fang, et al., Host–guest molecular interaction enabled separation of large-diameter semiconducting single-walled carbon nanotubes, 143(27) (2021) 10120-10130.